Electrolyte design for high-energy density Lithium-ion battery with pure Silicon anode

A.J. Hobo

TU Delft

Electrolyte design for high-energy density Lithium-ion battery with pure Silicon anode

by

A.J. Hobo

to obtain the degree of Master of Science

at the Delft University of Technology,

to be defended publicly on Tuesday November 2, 2021 at 15.00.

Student number:	5181283	
Project duration:	February 8, 2021 – November 2, 2021	
Thesis committee:	Dr. Y. Gonzalez Garcia,	TU Delft, supervisor
	Dr. Z. Li,	LeydenJar Technologies, supervisor
	Dr. A. Didden,	LeydenJar Technologies, supervisor
	Dr. E. M. Kelder	TU Delft

This thesis is confidential and cannot be made public until November 2, 2023.

TU Delft

LeydenJar
ENERGISING TECHNOLOGIES

Abstract

Silicon anodes can boost the energy density of lithium-ion batteries due to its high theoretical capacity up to ∼3600 mAh/g. However, a challenge of the use of silicon anode is 300% swelling/shrink upon lithiation/delithiation, which is a major cause of battery failure. A lithium-ion battery with silicon anode requires the formation of a flexible and stable solid electrolyte interphase (SEI) on the anode's surface to prevent continuous electrolyte decomposition, to mitigate the volume changes and to enable good Li-ion transportation. It is still a challenge to develop new electrolyte compositions to mitigate the continuous SEI formation and, consequently, enhance the cycle life. In this thesis, a 100% pure amorphous silicon anode is investigated in lithium-ion battery cells with an energy density up to 1350 Wh/L. The effect of different electrolyte compositions on the electrochemical behaviour and cycle life is studied. The results show that the addition of fluoroethylene carbonate (FEC) and vinylene carbonate (VC) to an electrolyte mixture of $LiPF_6$ and a pure linear carbonate solvent improves the capacity retention for over 100 cycles. The addition of co-solvents, propylene carbonate (PC) or ethylene carbonate (EC), improves the silicon utilisation level from ∼1500 to ∼1700 mAh/g. The diallyl pyrocarbonate (DAPC) additive in the electrolyte improves the capacity retention at 100 cycles from 67.7% to 72.2% in a full NMC-622/Si coin cell and from 84.2% to 90.8% in a full pouch cell. This study demonstrates that the electrolyte composition has an effect on the cycle life of lithium-ion batteries with silicon anode, likely by SEI formation from preferable decomposition products and from a complementary mixture of electrolyte components.

Contents

1

Introduction

Lithium-ion batteries (LIBs) are applied in many applications, ranging from consumer electronics, to clean energy driven applications, like electric vehicles and stationary energy storage. The main drivers in the development of LIBs for these applications are an increased energy density and cycle life compared to conventional alkaline batteries, which allows consumers to charge the batteries less and use them longer. The high energy density of the material allows for the extension of the driving range of an electric vehicle or the storage of green, yet fluctional, electricity for example. An increased energy density can be achieved by replacing the commonly used graphite anode by a silicon anode. Graphite has a gravimetric specific capacity of 372 mAh/g [45], however, when the graphite material is replaced by silicon, with a gravimetric specific capacity of 3579 mAh/g upon full lithiation to $Li_{15}Si_4$ [39], a 10 times higher specific capacity can be achieved. Moreover, Si is a naturally abundant element in earth's crust, which is environmentally friendly, cheap and non-toxic [37].

One of the main challenges in the development of a LIB with a Si anode is the large volume change of Si anode during cycling. It undergoes about 300 volume% swelling/shrink upon lithiation/delithiation. One can compare this with a swelling of only 10 volume% upon intercalation of Li-ions in the commonly used graphite anode [64]. The swelling of the silicon anode is one of the main causes of battery failure [64]. The mechanism that causes cell failure is shown in 1.1.

Cell failure occurs after prolonged cycling by the formation of a very thick and insulating Solid Electrolyte Interphase (SEI), which prohibits the Li-ion transport [45]. The function of the SEI, however, is to transport Li-ions to the anode and block electrons, preventing electrolyte decomposition. Upon the first lithiation cycle, the SEI is formed via the decomposition of electrolyte components, which leads to consumption of active Li-ions in a LIB. Upon lithiation/delithiation Si expands/shrinks, resulting in crack formation in the electrode and SEI layer, exposing 'fresh' Si again to the electrolyte, thereby leading to spontaneous Li-ion loss by the formation of new SEI. Therefore, the SEI layer on a Si anode thickens upon prolonged cycling, by the continuous cracking and reformation of the SEI.

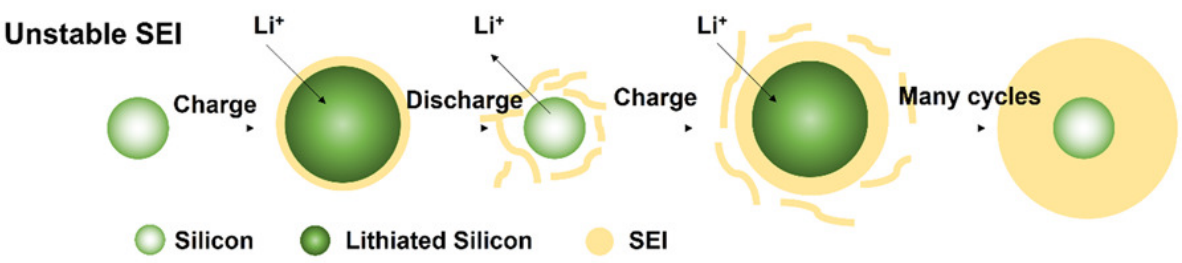

Figure 1.1: Schematic of the formation and transformation of the SEI during prolonged lithiation and delithiation. Adapted from [55].

The continuous growth of the SEI should be prevented and therefore the SEI should have good flexibility and mechanical strength [18]. A flexible and stable SEI needs to be formed, which is preferably thin, uniform, polymeric and protective, to mitigate the cells swelling and enable good Li-ion transportation [45, 65]. By alterning the composition of the electrolyte, one can expect to form an ideal SEI layer, since the SEI is formed by the decomposition products of the electrolyte. Therefore, the main aim of this research is to investigate what effect different electrolyte compositions have on the cycle life of a LIB with pure Si anode.

The simplest form of an electrolyte consists of a solvent and a lithium salt. The solvents will decompose upon charging the battery and form the SEI layer, so by altering the solvent composition, one can tweak the properties of the SEI. Another approach is to add additives to the electrolyte, which have a higher reduction potential than the solvents, so they preferentially decompose and restrict the solvent parasitic reaction. The additives will therefore determine the properties of the SEI. The body of this research will entail the effect of various solvent compounds on the cycle life of a LIB with Si anode and the effect of various additive compounds.

Leyden Jar Technologies (LJT) aims to develop a pure Si anode for use in LIBs. The Si anode of LJT is unique, since LJT claims to have developed a nano- and micro- pore structure to absorb significant expansion of Si during lithiation by deposition of a plasma-enhanced chemical vapor deposition (PECVD) grown amorphous Si film on a Cu substrate. Due to the high porosity of the Si deposition layer of approximately 30%, the Si anode of LJT shows significantly less volume expansion than the theoretical expansion of 300% [12]. Nevertheless, due to the breakage of the SEI layer during cycling caused by the bigger volume changes of the anode compared to a graphite anode, LJT still faces challenges of developing new electrolyte compositions to mitigate the continuous SEI formation.

The focus of this research is on the electrochemical behaviour of the LIB with Si anode with different electrolyte compositions. Different electrolyte compositions were investigated by means of long term charge/discharge tests, Direct Current Internal Resistance (DCIR) measurements and Electrochemical Impedance Spectroscopy (EIS). Furthermore, the behaviour of the anode material during lithiation and delithiation is investigated by means of Cyclic Voltammetry (CV).

It is assumed throughout this research that the biggest impact on the cycle life of the LIB is reached by an alteration of the SEI layer composition. The formation of a preferable SEI layer by an altered electrolyte composition can mitigate the detrimental effects of swelling of the Si anode and therefore prevent early battery failure. The cycle life of the battery is defined as the amount of cycles a battery can reach until the event of rapid capacity fade or the amount of cycles a battery can reach until 80% capacity retention is reached. The 80% capacity retention line stems from the battery utilization targets of LJT.

In section 1.1 a description of the general build-up and the components of a LIB will be presented, followed by theory on the electrochemical analysis of a LIB in section 1.2. Chapter 2 will elaborate on materials and methods used and the results of the experiments will be displayed and discussed in chapter 3. Firstly, the results of the Cyclic Voltammetry experiment will be shown in section 3.1. Secondly, the results of the adaptation of linear carbonate solvents and the effect the attendance of Vinylene Carbonate (VC) and Fluoroethylene Carbonate (FEC) in the electrolyte on the cycling behaviour will be shown in section 3.2. Thirdly, the effect of the attendance of cosolvents, cyclic carbonate solvents, in the electrolyte will be shown in section 3.3. Lastly, the effect on the cycling behaviour of the attendance of diallyl pyrocarbonate (DAPC), dimethylacrylamide (DMAA) or (2-cyanoethyl)triethoxysilane (TEOSCN) in the electrolyte mixture will be shown in section 3.4. The DCIR results will be presented in section 3.5 and the EIS data will be shown in section 3.6. The results will be followed by a conclusion in Chapter 4.

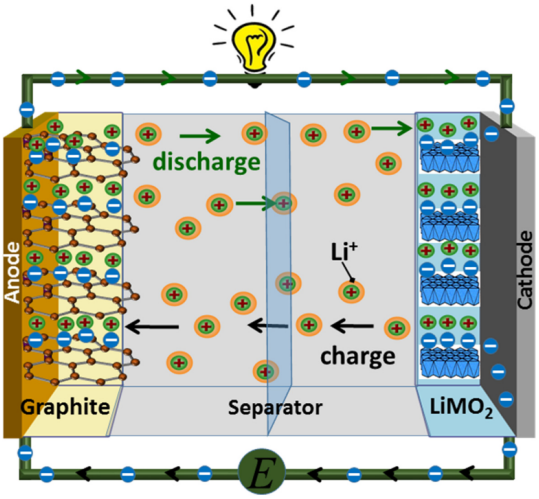

Figure 1.2: The general build-up of a LIB. Reprinted from [34].

1.1. Build-up of a lithium-ion battery

In general any electrochemical cell consists of a negative and a positive electrode, the anode and the cathode respectively, which present a potential difference between them. When the electrodes are connected via a conducting medium, charge can be transferred from the negative electrode to the positive electrode via migration of electrons. This can only happen if simultaneously positively charged species can migrate from the anode to the cathode to maintain the charge balance. This process is called delithiation and happens upon discharge of the battery. These positively charged species are typically ions in liquid electrolyte. In the case of a LIB, the positively charged species are Li-ions. The LIB is a rechargeable battery. When an electrical charge is supplied to the battery, the reaction described above can be reversed, which is called lithiation, and the battery will be charged. The migration of ions and electrons during charge and discharge are shown in Figure 1.2.

Figure 1.2 also shows two other components present in the battery system, the separator and the electrolyte. The separator is used to create a physical barrier between the anode and the cathode, so that no short circuit can exist, and to allow positively charged ions to migrate between the cathode and the anode. The electrolyte ensures that the Li-ions can move between the electrodes. The electrolyte consists of lithium salt dissolved in one or more solvents. Some additives might be added to the electrolyte to enhance the performance of the battery. This section describes the function and properties of a few important battery components: the anode and cathode material, the electrolyte solvents and salt and additives. It is assumed that the separator and the type of separator does not have a big influence on the cycle life of the LIB, so the separator is not discussed further here.

1.1.1. Anode material

The negative electrode is typically made of a current collector, such as copper foil coated with a layer of graphite or silicon. Graphite has a layered structure. The Li-ions will intercalate between the layers of the graphite [15], upon charging the battery, causing only a minor volume expansion of around 10%. The mechanism of lithium insertion into the silicon is quite different, since the Li-ions will form an alloy with the silicon atoms. Upon lithiation the amorphous Si will form a crystalline $Li_{15}Si_4$ phase with the same structure as $Cu_{15}Si_4$ (Pearson Symbol: cI76) [39] and the alloy formation will cause a significant volume expansion. The main advantage of the replacement of graphite with Si as anode material is that a 10 times higher specific capacity can be reached. Si can accommodate 3.75 Li-ions per Si atom, whilst only one Li-ion can be accommodated per 6 carbon atoms.

The large capacity for Li storage in Si causes some problems during cycling. Due to the volume changes, the Si anode film cracks and subsequently pulverizes. Even though the reaction is reversible, over time the electrode structure and components deteriorate and contact is lost between the current collector, the copper foil, and the Si particles. Therefore, Si particles become isolated and active Si

is lost. Lastly, due to cracking and pulverization, 'fresh' Si is always exposed, so that new SEI forms. Li-ions are thus continuously consumed for the formation of new SEI [14].

1.1.2. Cathode material

The cathode typically consists of an aluminium foil coated with a layer of active cathode material. A variety of cathode materials are available for LIB. $LiCoO_2$, $LiMn_2O_4$, $LiNiO_2$ and $LiFePO_4$ are a few of the most well-known cathode materials. The insertion reaction of Li-ions into the cathode material occurs via the intercalation mechanism.

$LiCoO_2$ is developed the earliest, but cobalt is a toxic and expensive material, so alternatives were sought after. The theoretical specific capacity of $LiCoO_2$ (274 mAh/g) is high, but in practice the material only reaches half of its theoretical specific capacity. Cobalt is being replaced by manganese, which is less toxic, more abundantly available and less expensive, and also by nickel, which is a heavy metal, but relatively low-cost and more abundantly available then cobalt [35, 61, 66].

To optimize the properties of the materials, researchers started to replace cobalt atoms by using the manganese and nickel atoms with a certain ratio in $LiCoO_2$ layered structure. The result is an NMC ($LiNi_xMn_yCo_zO_2$) material with a theoretical specific capacity, comparable to $LiCoO_2$, of 275 mAh/g [23]. In recent years, a trend has developed to increase the nickel content in the alloy to lower the costs of the material [35]. Moreover, the higher nickel content improves the electronic conductivity and the Li-ion diffusivity [36]. LJT uses $LiNi_{0.6}Mn_{0.2}Co_{0.2}O_2$ (NMC-622) as a cathode material.

$LiFePO_4$ is an upcoming material, which has a relatively low theoretical specific capacity (170 mAh/g). Nevertheless, a practical specific capacity can be reached of 65 to 95% of the theoretical specific capacity. Besides, iron and phosphate are low-cost and environmentally friendly materials [61, 66].

1.1.3. Solvents

The solvents generally used in a LIB are one or more of the following compounds: Propylene Carbonate (PC), Ethylene Carbonate (EC), Diethyl Carbonate (DEC), Dimethyl Carbonate (DMC) and Ethyl Methyl Carbonate (EMC). All these compounds are different types of aprotic carbonates, as depicted in Figure 1.3, which enable the dissolution of electrolyte salts. Xu et al. [59] identified the properties of an ideal solvent as:

- Low viscosity
- High boiling point
- Low melting point
- High flash point
- High dielectric constant
- Low reduction potential
- High oxidation potential

Mixing of the solvents can be a way to optimize the properties of the electrolyte. In Figure 1.4 a comparison has been made between the different solvents, based on a relative score assigned to the solvents for the parameters listed by Xu et al. [59]. Cyclic carbonates have a relatively high viscosity, but also a high dielectric constant and a high boiling point compared to the linear carbonates. Generally an electrolyte consists of a combination of EC/DEC or EC/DMC, but other combinations are also used to meet specific cell requirements [59]. The benefits of the EC/DEC and EC/DMC mixtures are caused by the high anodic stability of EC on cathode surfaces, high solubility of EC towards Li salts and low viscosity of DEC and DMC to promote ion conductivity [59].

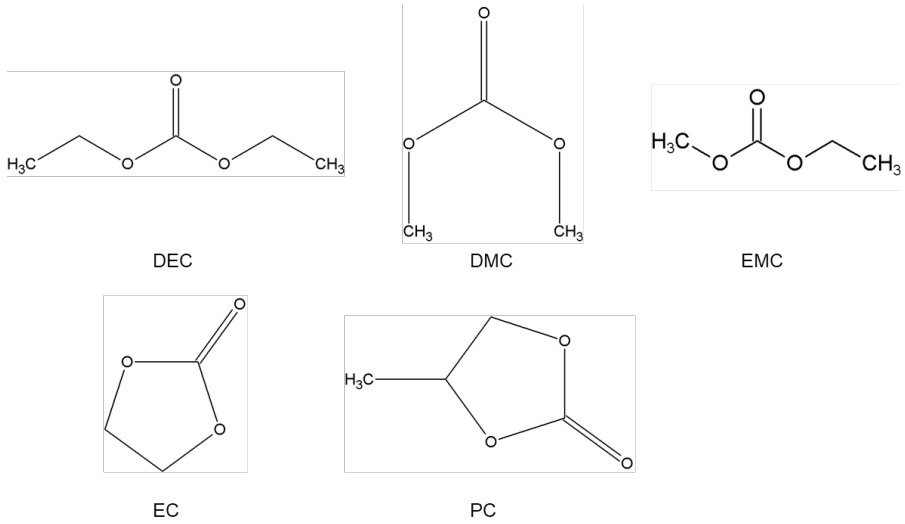

Figure 1.3: Molecule structures of different carbonate solvents typically used in LIBs.

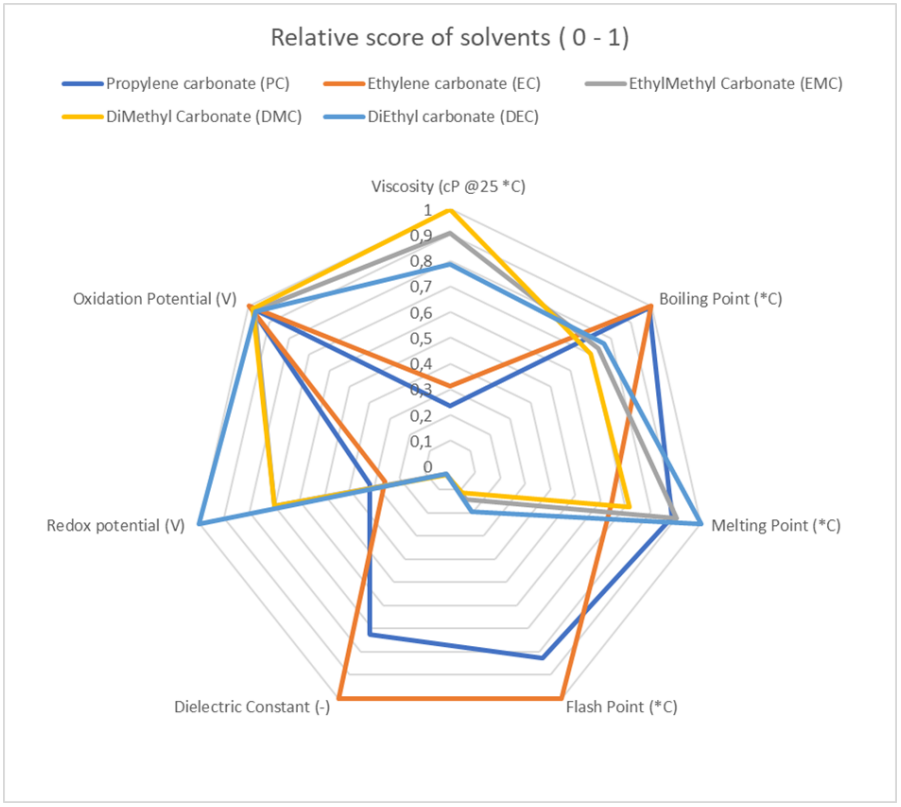

Figure 1.4: Comparison of solvents by assigning a relative score for different parameters. The score is based on the absolute values of the parameters obtained from [58].

1.1.4. Lithium salt

A variety of lithium salts exist for the LIB, like $LiClO_4$, $LiAsF_6$, $LiBF_4$, $LiCF_3SO_3$ and $LiPF_6$. Usually a single type of lithium salt is used in the electrolyte, rather than a combination of salts. $LiPF_6$ is often used, also by LJT. Therefore only $LiPF_6$ is discussed in this section.

$LiPF_6$ is known for a good balance of properties like high solubility, good ionic conductivity, high dissociation constant and sufficient electrochemical stability [62]. Nevertheless, there are some disadvantages to the usage of $LiPF_6$. This electrolyte salt is very sensitive to impurities, like water and alcohol. These impurities react with the anion and form HF, which is a highly reactive and toxic species [14]. At high temperatures large amounts of HF form, deteriorating the cell [26]. Furthermore, the salt is only stable at temperatures up to 70˚C [59].

1.1.5. Additives

Additives are added to the electrolyte to enhance the performance of the LIB and to prevent early deterioration. Usually additives play a sacrificial role. They are reduced before the other components in the electrolyte to form a passivating layer over the electrode's surface [45]. The SEI should have high flexibility and mechanical strength in order to be an effective passivation layer on the electrode surface. Besides that, the additives should prevent the continuous growth of the SEI layer. Therefore, the additive should have the following properties [18]:

- To form a passivating SEI film, which prevents further reduction of the electrolyte solvents;
- To reduce the surface resistance;
- To enhance the ionic conductivity of the SEI;
- To enhance the formation of alkyl dicarbonate;
- To have a higher reduction potential then the electrolyte solvents;
- To have high anodic stability;
- To have good cathodic reactivity;
- To be well polymerizable;
- To have a good thermal stability;
- To be less reactive with Li-ions;
- To have a lesser solvation behaviour;

In addition it is beneficial if the additive has low costs and if the synthesis, preparation process and storage are easily scalable and of limited negative environmental impact [59].

A selection of additives have been investigated in the past for use in a LIB with a Si anode. Some of them are shown in Figure 1.5. The first one in the top row of the figure, namely Vinylene Carbonate (VC), is derived from the solvent EC and contains a double bond rather than a single bond. This allows the molecule to be reduced earlier than the solvents. Later it was discovered that the addition of a fluorine atom to the molecule would enhance the properties of the additive. Fluoroethylene carbonate (FEC) is now a frequently used additive. Another type of additives are the silane-type additives. These molecules mostly form a siloxane network covering the electrode's surface. Lastly, salt type (ionic) additives have been investigated. In this case the electrolyte salt, rather than the solvents, partakes in the SEI layer formation with participation from either the cation or the anion [14]. More types of additives are being investigated. The common factor between them is the higher reduction potential with respect to other electrolyte components.

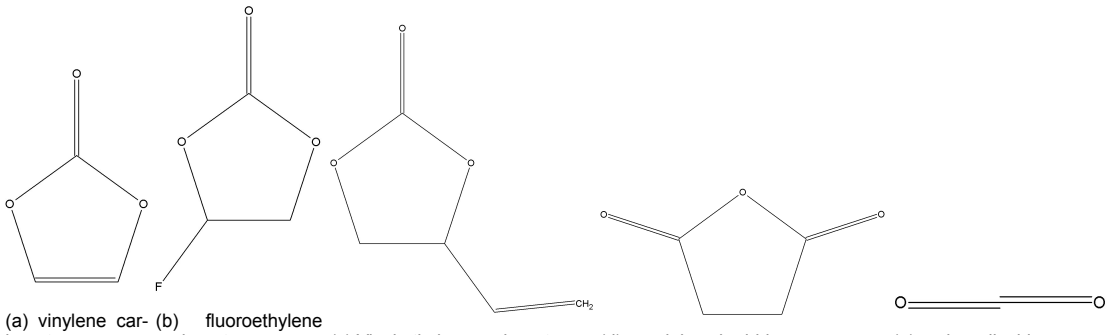

(a) vinylene carbonate (b) fluoroethylene carbonate (c) Vinyl ethylene carbonate (d) succinic anhydride (e) carbon dioxide

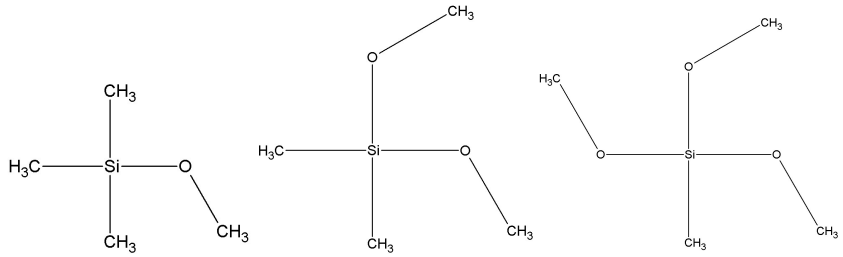

(f) methoxy trimethyl silane (g) dimethoxy dimethyl silane (h) trimethoxy methyl silane

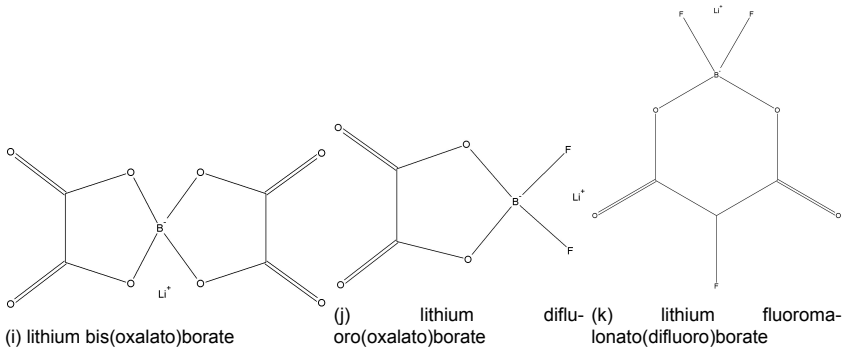

(i) lithium bis(oxalato)borate (j) lithium difluoro(oxalato)borate (k) lithium fluoromalonato(difluoro)borate

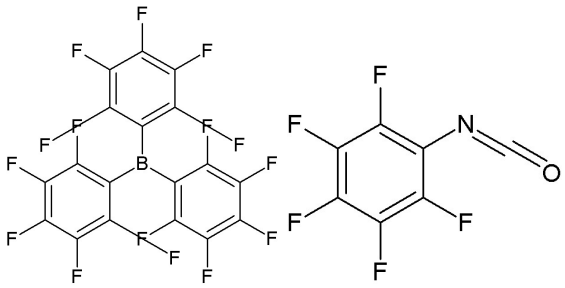

(l) tris (pentafluorophenyl) borane (m) pentafluorophenyl isocyanate

Figure 1.5: Molecule structures of different electrolyte additives introduced in [14].

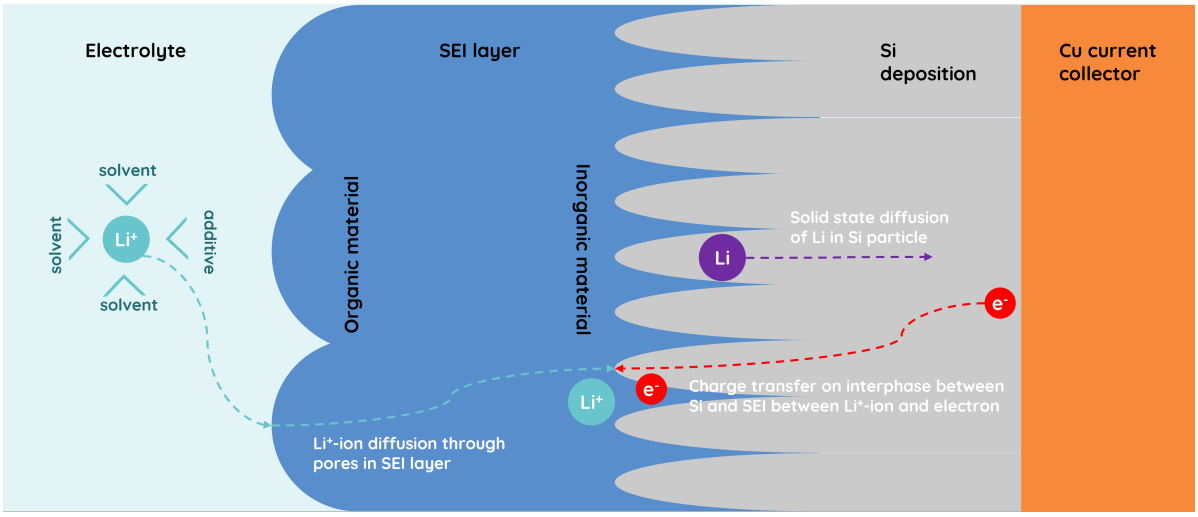

Figure 1.6: Model of the Si anode/electrolyte interphase and the migration of Li-ions, Li atoms and electrons upon lithiation.

1.2. Electrochemical lithium-ion battery analysis

It is important to construct a physically meaningful model of the materials and material interactions that are studied. This is important because the model is the basis for the assumptions made in the calculations that are performed. This study focusses on the electrochemical analysis of a LIB with Si anode. In this research prolonged charge/discharge cycling tests, DCIR experiments and more advanced CV experiments and EIS experiments are deployed. Section 1.2.1 will expand on the construction of such a model for the Si anode with the SEI layer. The following section, section 1.2.2, will elaborate on the theory behind DCIR, CV and EIS.

1.2.1. Model of the anode/electrolyte interphase

Figure 1.6 shows a schematic model of the Cu current collector with Si deposition, the SEI and the electrolyte and the migration of Li-ions, Li particles and electrons within the material during lithiation. This model is used as a basis for the analysis of the electrochemical behaviour of the LIB with Si anode throughout this report. A solvated Li-ion will migrate towards and inwards the Si deposition layer upon the application of an electrical charge. The process of lithiation shown in Figure 1.6 is described by Levi and Aurbach [31] as follows.

Li-ions are solvated by solvent and additive molecules within the electrolyte and migrate upon an applied current towards the anode. Therefore, the ions need to pass the SEI layer by diffusion through the pores in the SEI layer. The SEI material, which consists of the decomposition products of the electrolyte, greatly determines the diffusion coefficient of the Li-ions. Finally, the Li-ions reach the Si deposition layer, where they will recombine with an electron, originating from the copper current collector, to form solid state lithium. This process is called charge transfer. At the interface between the SEI and the Si deposition layer Li-ions and electrons will accumulate and form a double layer. Lastly, mass transfer of solid state lithium will occur within the Si deposition layer and the Li will accumulate near the current collector surface [31].

Simultaneously with charge transfer and solid state diffusion, lithium will form an alloy with the Si particles upon charge to reach a fully lithiated state of the Si particles. The fully lithiated state of Si was long believed to be $Li_{21}Si_5$, until in 2004, when Obrovac and Christensen demonstrated with the use of X-ray powder diffraction that not $Li_{21}Si_5$ is the highest lithiated state, but $Li_{15}Si_4$ [39]. In 2020, Jiang et al. proposed a zero-dimensional mechanistic model, which includes a reaction pathway for the lithiation and delithiation of Si [21].

Figure 1.7 illustrates the reaction pathway proposed by Jiang et al. [21]. During charge amorphous Si transforms via a two-step reaction pathway to a-Li_xSi and further to a-$Li_{15}Si_4$ according to reaction pathways 1 and 2. Reaction pathways 1 and 2 are always reversible. Upon further lithiation, when the cell is charged below 0.05 V (V vs Li/Li^+), critical nuclei of $Li_{15+\delta}Si_4$ form via reaction pathway f3. If

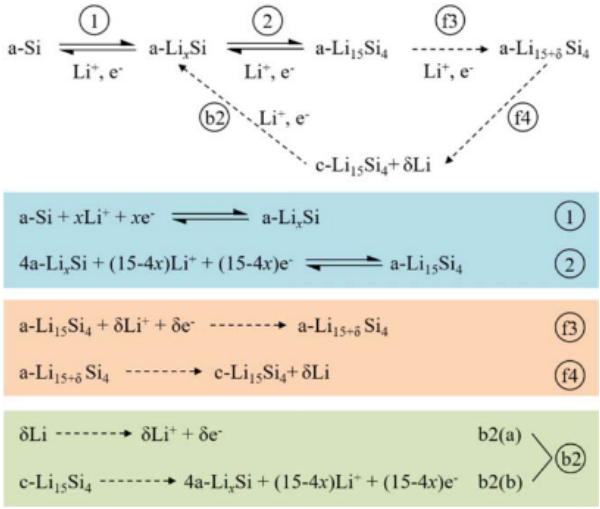

Figure 1.7: Reaction pathways for lithiation and delithiation of silicon at room temperature. Reprinted from [21].

these nuclei reach a critical size, a crystalline phase can form consisting of c-$Li_{15}Si_4$ + δ Li via reaction pathway f3. During discharge the reaction can reverse and the intermediate phase a-Li_xSi can be formed via reaction pathway b2 [21].

1.2.2. Selected electrochemical analysis techniques

The combination of the model presented in section 1.2.1 and the theory behind the selected electrochemical analysis techniques form the basis for the analysis of the electrochemical behaviour of the batteries. In this study, the electrochemical behaviour of the batteries is analysed with CV, long term charge/discharge tests, DCIR and EIS. The theory behind CV, DCIR and EIS is discussed in this section. Accordingly, the required knowledge to understand the results and discussions presented in chapter 3 is provided.

CV is utilized to understand the mechanisms at play during lithiation and delithiation of the anode material, which contributes to the verification of the model presented in section 1.2.1. Long term charge/discharge tests are utilized to analyse the change in cycling behaviour of the batteries with different electrolyte compositions. Since this test is relatively simple, there is no need for further elaboration on the specifics of long term charge/discharge tests in this section. The evolution of the resistance in the cell is determined by DCIR and EIS. DCIR has the advantage that the analysis of the results is relatively quick compared to the analysis of EIS results, so DCIR is utilized to give a first indication on the evolution of the resistance during a battery's cycle life. As it is not possible to distinguish the contribution to the resistance of all processes at play in a battery, EIS is utilized. EIS has the advantage that the contribution of different processes to the resistance is a cell can be distinguished. In this research especially the evolution of the SEI resistance by the change in electrolyte composition is of interest.

Cyclic Voltammetry

CV is performed by varying the applied voltage at a constant scan rate within a predetermined voltage window, and measuring the current response. Peak currents are measured in the event of reduction and oxidation reactions of molecular species in the electrochemical system or electron transfer-initiated chemical reactions. A typical current response is shown in Figure 1.8. The minimum in the curve is typically related to a reduction reaction and the maximum in the curve is typically related to a oxidation reaction.

The peaks emerge from the diffusion of the analyte, in a LIB these are the Li-ions, within the electrochemical system. The change in concentration of the analyte or system response to a change in electrode potential is described by the Nernst equation (1.1), which relates the potential of an electrochemical cell (E_{eq}) to the standard potential of a species (E_0) and the relative activities or the concentrations of the oxidized ([Ox]) and reduced species ([Red]). In this equation, F is Faraday's constant,

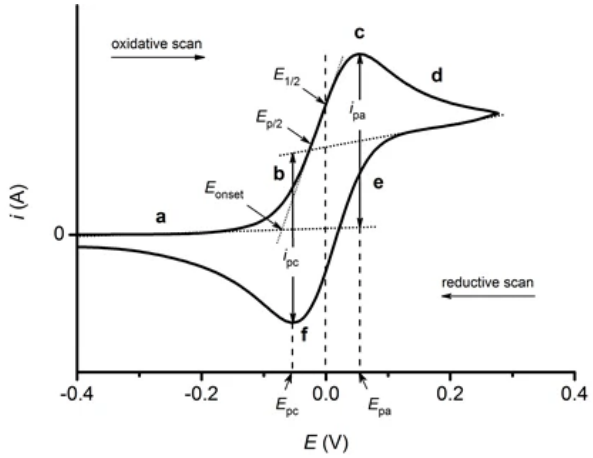

Figure 1.8: Example of a typical current response to an applied voltage at a constant scan rate. Reprinted from [40].

R is the gas constant, n is the number of electrons involved in the reaction and T is the temperature.

$$E_{eq} = E^0 - \frac{RT}{nF} \ln \frac{[\text{Red}]}{[\text{Ox}]} \tag{1.1}$$

The current is dictated by the diffusion of additional species from the bulk solution towards the anode surface. When the potential changes during a CV scan, the concentration of species in solution in the double layer changes over time, as the species are reduced or oxidized, according to the Nernst equation. The scan towards lower potentials induces the reduction reaction of the species, which results in the measurement of a current and depletion of the species in solution at the electrode surface. A diffusion layer containing the reduced species at the electrode surface starts to grow, impeding the diffusion of the species from the bulk electrolyte towards the electrodes surface. Of course, when the scan is reversed towards higher potentials, oxidation of the formally reduced species occurs and a negative current is measured.

At faster scan rates the size of the diffusion layer decreases, which results in higher measured currents. So, a variation of the potential scan rate results in different measured peak currents. From this variation it is possible to determine the diffusion coefficient of the oxidized species with the use of Randles-Sevcik equation (1.2). This equation relates the peak current (i_p) to the square root of the scan rate (v) and the diffusion coefficient (D_{Li^+}), where n is the number of electrons involved in the redox reaction, F is the Faraday Constant, A is the apparent electrode surface area, C^0 is the bulk concentration of the electrolyte salt, R is the gas constant and T is the temperature.

$$i_p = 0.4463nFAC^0 \sqrt{\frac{nFvD_{Li^+}}{RT}} \tag{1.2}$$

Direct Current Internal Resistance

DCIR is used to measure the DC resistance at predetermined moments in time and at a predetermined State of Charge (SOC), during a batteries lifetime. During a small time-frame a change in current, a pulse, is applied and the voltage response is measured. The resistance of the cell over this small time period is determined. It is assumed that the short current pulse does not significantly change the SOC of the battery. One can differentiate between the instantaneous resistance of the cell and the diffusive resistance. Both the evolution of the instantaneous and diffusive resistance in time or over a battery's cycle life can be plotted per SOC.

The voltage response during a change in current is illustrated by Figure 1.9. The steep decrease, upon charge of the cell, in voltage after the pulse is called the "Instantaneous resistance" and is determined by the Ohmic resistance originating from the current collectors, the active material of the electrodes, the ionic conductivity of the electrolyte and connections like tab welds, contact resistances and safety

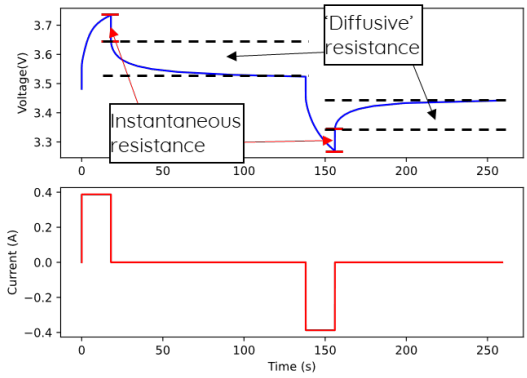

Figure 1.9: Illustration of a DCIR test by the method of LJT. Below is the current pulse, above shows the voltage response.

elements [4]. The instantaneous resistance is calculated by dividing the change in potential ($\Delta V_{\text{instant}}$) in the first 20 msec after the current pulse over the total change in current (ΔI_{total}):

$$R_{\text{instant}} = \frac{\Delta V_{\text{instant}}}{\Delta I_{\text{total}}} \tag{1.3}$$

The potential relaxation after the Ohmic drop shows a first order relation. From this relaxation curve the "Diffusive resistance" can be calculated. The diffusive resistance is determined by electrochemical reactions and non-Ohmic processes [4], like charge transfer resistance and diffusion of Li-ions through the electrode. The diffusive resistance is calculated by dividing the change in potential ($\Delta V_{\text{diffusive}}$) during relaxation of the potential curve over the total change in current (ΔI_{total}):

$$R_{\text{diffusive}} = \frac{\Delta V_{\text{diffusive}}}{\Delta I_{\text{total}}} \tag{1.4}$$

DCIR is an easy tool to analyse the change in resistance of the cell. However, one cannot differentiate between the different processes that could cause a change in the resistance in the diffusive or the instantaneous regime.

Electrochemical Impedance Spectroscopy

EIS is performed by applying a small alternating current potential to the battery and measuring and analysing the pseudo-linear current response. (A pseudo-linear response means that the current follows the potential while locally adhering to Ohm's law.) The tendency of a system to oppose the alternating current potential is a measure of the impedance, which is a function of the signal's frequency. EIS allows to differentiate between various electrochemical processes in an electrochemical system, as different kinetic steps within the system have different frequency responses. The potential-controlled excitation (E_t) as a function of time and corresponding current response (I_t) can be represented as:

$$E_t = E_0 \sin(\omega t) \tag{1.5}$$

$$I_t = I_0 \sin(\omega t + \phi) \tag{1.6}$$

The amplitude of the signal is represented by E_0, the radial frequency by ω and the phase shift by ϕ. The impedance of the system (Z) can be expressed as:

$$Z = \frac{E_t}{I_t} = Z_0 \frac{\sin(\omega t)}{\sin(\omega t + \phi)} \tag{1.7}$$

One can rewrite Equation (1.7) into Equation (1.8), where the complex impedance is represented by an imaginary part and a real part.

$$Z_\omega = Z_0(cos(\phi) + i \sin(\phi)) \tag{1.8}$$

Table 1.1: Common electrical equivalent circuit elements and their respective impedances [16].

Element	Resistor	Capacitor	Constant Phase Elem.	Inductor	Warburg
Equivalent Circuit Parameter	R	C	CPE	L	W
Impedance	R	$\frac{1}{j\omega C}$	$\frac{1}{Q(\omega C)^{\alpha}}$	$j\omega L$	$\frac{A_W}{\sqrt{\omega}} + \frac{A_W}{j\sqrt{\omega}}$

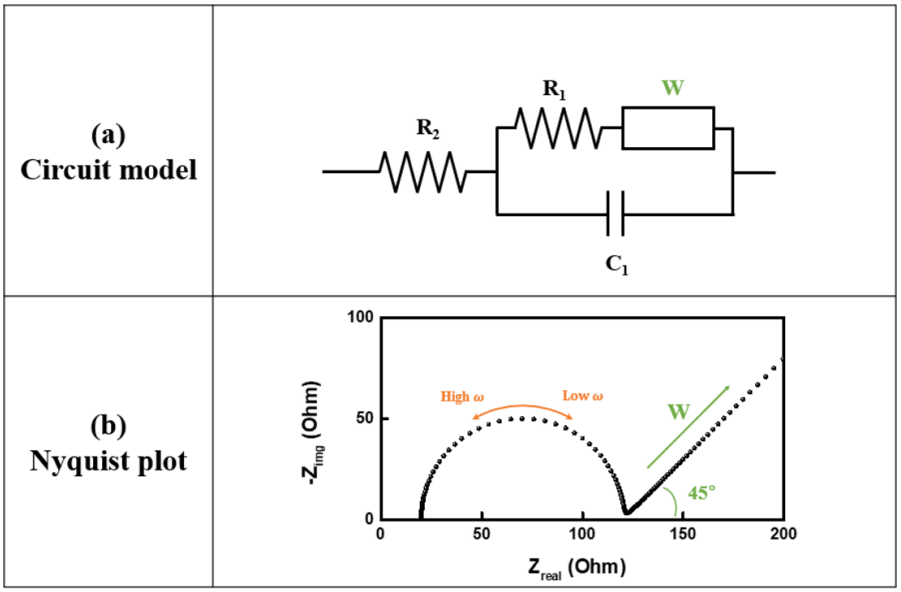

Figure 1.10: (a) a Randles circuit and (b) the corresponding complex plane for the redox system represented by a Randles circuit. Reprinted from [10].

Typically, impedance data is represented in a Nyquist, $-\Im(Z)$ vs $\Re(Z)$, or Bode plot, $|Z|$ vs ω and ϕ vs ω. The data is often analysed with the use of an equivalent circuit (EC). The behaviour of the cell is then compared with the modelled behaviour of the EC to determine the parameters of the processes in a cell. An EC usually consists of a resistor, a capacitor and an inductor. More complex circuits can contain components like a Constant Phase Element (CPE), to describe the imperfect behaviour of capacitances, and Warburg impedance, to describe mass transfer characteristics. The impedance of these elements are defined in Table 1.1 [16].

An example of a common EC in Li-ion battery research is the Randles circuit as shown in Figure 1.10. The cell consists of a resistor in series with a component, which consists of a capacitor parallel to a resistor and a Warburg element. The Nyquist plot shows a semicircle with its origin at a positive real impedance value and a tail with a 45° angle in the low frequency domain. The value of R_2, known as the solution resistance between the electrodes [28], will be determined by the point at which the semicircle cuts the '0 imaginary impedance'-plane. The value of R_1 will be determined by the diameter of the semicircle and describes the resistance due to charge transfer. The Warburg impedance (Z_W) is associated with the diffusion of ions by

$$Z_W = A_W \omega^{-1/2}(1 - i) \tag{1.9}$$

Where A_W is related to the diffusion coefficient (D) by

$$A_W = \frac{RT}{n^2 F^2 A\sqrt{2}} \left(\frac{1}{C\sqrt{D}} \right) \tag{1.10}$$

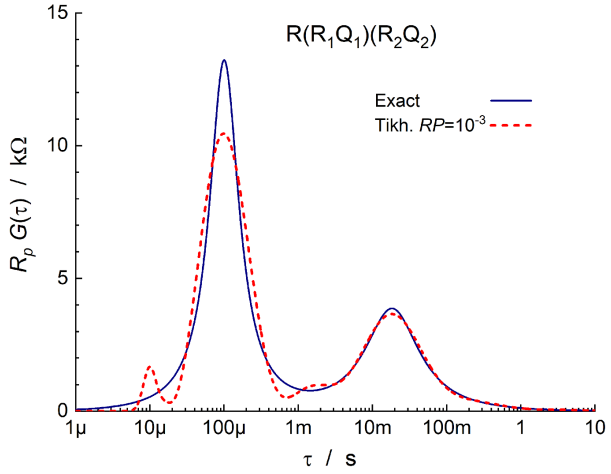

Figure 1.11: DRT function derived by Tikhonov Regularization from a R(RQ)(RQ) circuit with a Regularization Parameter of 10^{-3}. The solid line represents the exact DRT. Reprinted from [5].

Otherwise, the impedance data can also be analysed with the use of a Distribution of Relaxation Times (DRT) map. A RC-circuit element is represented by a single time constant, characterised by $\tau_{RC} = R \cdot C$ in the case of ideal capacitive behaviour [5, 11]. However, most studies are now carried out with electrodes made of non-ideally polarizable material, so the capacitor is replaced by a CPE. As a result the time constants show a distribution in the τ-domain with $\tau_{\text{max}} = (R \cdot Y_0)^{\frac{1}{\phi}}$, where Y is the admittance (Z^{-1}) and the exponent ϕ is not the phase shift, but a dimensionless parameter (ϕ<1) used to describe the imperfect capacitors or inhomogeneities shown in the Nyquist plot as a depressed semi-circle [11, 28].

The distribution function is derived from the impedance data by solving a 'Fredholm integral of the second kind' as discussed by Boukamp [5]. A problem with solving this integral is that many solutions exist. A widely applied procedure for solving these type of inversion problems is the Tikhonov Regularization procedure. A distribution function $R \cdot G(\tau)$ versus the time constants (τ) is obtained as simulated in Figure 1.11.

The Tikhonov Regularization procedure follows the exact DRT quite well apart from some minor oscillations. However, the procedure knows two important limitations. Firstly, the Tikhonov regularization shows deviations in the high frequency range. Secondly, the Regularization Parameter, which is a critical factor to obtain an acceptable result, needs to be adjusted. A too small value causes additional oscillations. When the value is increased the DRT becomes more smooth, however, it is also losing details, especially in the high frequency region [5].

2

Methodology

This chapter describes the experimental conditions under which the experiments in this research were performed. In section 2.1 the process of cell assembly and the compositions of the studied electrolytes are described. In section 2.2 the settings of the electrochemical characterisation tests are given.

2.1. Battery preparation

Four different cell configurations were used for the purpose of thesis: full coin cell, full pouch cell, half coin cell and symmetric coin cell. Full cells consist of a NMC-622 cathode and a Si anode. The pouch cell is different from the coin cell, because of its geometry and way of assembly as is elaborated hereafter. Half coin cells consist of Si anode material and lithium metal as the counter electrode. The lithium metal provides a constant Li concentration in the electrode, therefore the effects of the counter-electrode's SOC on the voltage profile are excluded. Likewise, as an alternative for half coin cells, symmetric coin cells are assembled in which two electrodes are of equal material. A potential needs to be induced upon assembly between the two electrodes in a symmetric coin cell, which is established by combining a fully charged electrode with a fully discharged electrode. In a symmetric coin cell, the effects of the counter-electrode on cell kinetics and stability are also excluded.

Full coin cell The amorphous Si electrode produced by LJT was punched into disks (A = 1.266 cm^2) and paired with NMC-622 electrodes (surface area: A = 0.969 cm^2, areal capacity: C_{area} = 3.5 mAh/cm^2) to Si/NMC-622 full cells, with an N/P ratio ≈ 1.2. The N/P ratio describes the areal capacity ratio between the anode and the cathode in a battery. The cells were assembled in an Argon filled glove box. The electrodes were separated by two layers of separators, Celgard 2500 and glass fiber. A total amount of 80 μL of electrolyte with compositions further specified in Table 2.1 was added to the cell.

Full pouch cell The amorphous Si electrode produced by LJT was punched into rectangles (A = 35.08 cm^2) and paired with NMC-622 electrodes (surface area: A = 30.1 cm^2, areal capacity: C_{area} = 3.5 mAh/cm^2) to Si/NMC-622 full cells (N/P ratio ≈ 1.2). The cells were assembled in air and injected with electrolyte in an Argon filled glove box. The electrodes were separated by one layer of separator, Celgard 2500. A total amount of 0.7 g of electrolyte with compositions further specified in Table 2.1 was added to the cell.

Half coin cell The amorphous Si electrode produced by LJT was punched into disks (A = 1.266 cm^2) and paired with lithium metal electrodes (surface area: A = 1.9 cm^2) to Si/Li half cells. In this configuration Si is the cathode and Li metal is the anode. The cells were assembled in an Argon filled glove box. The electrodes were separated by two layers of separators, Celgard 2500 and glass fiber. A total amount of 80 μL of electrolyte with compositions further specified in Table 2.1 was added to the cell.

Table 2.1: List containing the electrolyte compositions with their respective names and the cell types in which they were used.

Electrolyte name	Electrolyte composition	Used in cell type
EL1	1M $LiPF_6$ in pure EMC	Full coin cell, full pouch cell
EL2	1M $LiPF_6$ in pure DMC	Full coin cell, full pouch cell
EL3	1M $LiPF_6$ in pure DEC	Full coin cell, full pouch cell
EL4	1M $LiPF_6$ in pure EMC 2 wt% AN 5 wt% FEC 2 wt% VC	Full coin cell, full pouch cell
EL5	1M $LiPF_6$ in pure DMC 2 wt% AN 5 wt% FEC 2 wt% VC	Full coin cell, full pouch cell
EL6	1M $LiPF_6$ in pure DEC 2 wt% AN 5 wt% FEC 2 wt% VC	Full coin cell, full pouch cell
EL7	1M $LiPF_6$ in PC:EC:DEC (1:1:1 vol%) 2 wt% AN 5 wt% FEC 2 wt% VC	Full coin cell
EL8	1M $LiPF_6$ in PC:DEC (1:1 vol%) 2 wt% AN 5 wt% FEC 2 wt% VC	Full coin cell, full pouch cell
EL9	1M $LiPF_6$ in EC:DEC (1:1 vol%) 2 wt% AN 5 wt% FEC 2 wt% VC	Full coin cell, half coin cell, full pouch cell
EL10	1M $LiPF_6$ in EC:DEC (1:1 vol%) 2 wt% AN 5 wt% FEC 1 wt% VC	Full coin cell, full pouch cell, symmetric coin cell
EL11	1M $LiPF_6$ in EC:DEC (1:1 vol%) 2 wt% AN 5 wt% FEC 1 wt% VC 1 wt% DAPC	Full coin cell, full pouch cell, symmetric coin cell
EL12	1M $LiPF_6$ in EC:DEC (1:1 vol%) 2 wt% AN 5 wt% FEC 1 wt% VC 1 wt% DMAA	Full coin cell, full pouch cell, symmetric coin cell
EL13	1M $LiPF_6$ in EC:DEC (1:1 vol%) 2 wt% AN 5 wt% FEC 1 wt% VC 1 wt% TEOSCN	Full coin cell, full pouch cell, symmetric coin cell

Symmetric coin cell Full pouch cells were produced, which were cycled for two cycles at a rate of 0.2C between 2.5 and 4.2 V, this is called formation, after which one of the two cells was fully charged and the other was fully discharged. In an argon filled glove box, the pouch cells were disassembled, after which the fully charged anode was cut in small circles with a surface area of 0.969 cm^2 and the fully discharged anode in large circles of 1.266 cm^2. All the electrodes were rinsed with pure DMC and subsequently vacuum dried. Large amorphous Si electrodes were paired with small amorphous Si electrodes to Si/Si symmetric cells. The electrodes were separated by two layers of separators, Celgard 2500 and glass fiber. A total amount of 80 μL of electrolyte with compositions further specified in Table 2.1 was added to the cell.

2.2. Electrochemical characterisation

Four different tests were performed on the cells, prolonged charge/discharge cycling of the cells, Direct Current Internal Resistance (DCIR), Cyclic Voltammetry (CV) and Electrochemical Impedance Spectroscopy (EIS). Charge/discharge cycling was performed in full cells, as was DCIR. The performance of these tests in full cells was chosen because a full cell represents the expected behaviour most adequately. CV was performed in half coin cells to exclude the effect of the counter-electrode. Since the Li metal electrode still has an effect on the kinetics and cell stability, EIS was performed in symmetrical coin cells to solely analyse the effect of different electrolyte compositions on the electrode of interest. The details and settings of the tests are discussed hereafter.

Charge/discharge cycling of the Si/NMC-622 full cells was performed in a voltage range of 2.5/3.0 – 4.0/4.2V at room temperature on a LAHNE Battery Testing System type V4.3. The cycling protocol started by a so called formation protocol as schematically shown in Figure 2.1. Therefore the batteries were charged for 5h with a current of 0.02C and subsequently for 9h or until a voltage of 4.2V was reached with a current of 0.1C, followed by discharging down to 2.5V at 0.1C. One additional charge/discharge step at 0.2C and a charge step at 0.2C for 1.5h (charging the cell to approximately 30% State of Charge (SOC)) completed the formation process of the Si/NMC-622 full cells.

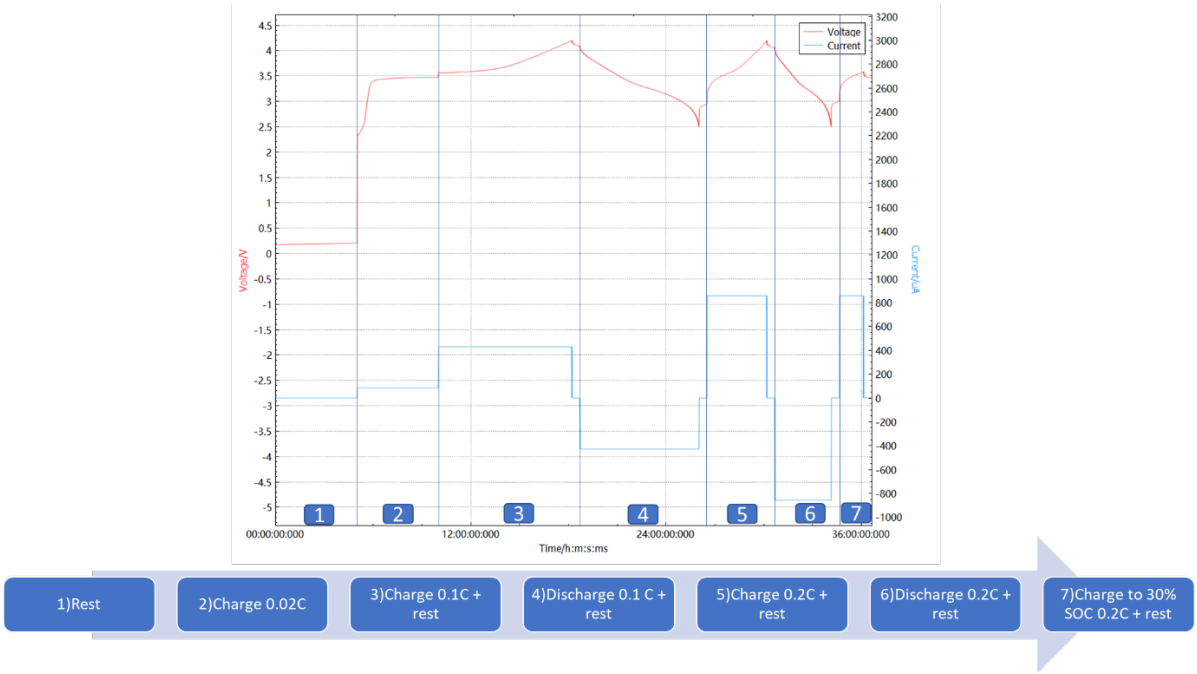

Figure 2.1: Evolution of voltage and current during the formation protocol.

The Initial Coulombic Efficiency (ICE) and the total capacity of the cell were determined from the formation process. The ICE is defined as the first discharge capacity divided by the first charge capacity. Afterwards, the cells were cycled with the use of two different protocols, since the experiments were performed at the company, who update and implement new protocols frequently as they notice that the new protocol accelerates the data acquisition and analysing process. It must be pointed out that the two different protocols used does lead to very comparable charge/discharge cycling profiles of the batteries.

Cycling protocol 1 After formation, the cells were discharged down to 3.0V, followed by a charge and discharge step at a low current of 0.05C between 3 and 4V and a DCIR step. These three steps were followed by cycling at a constant charge/discharge current of 0.5C between 3.0 and 4.2V. Additionally, a constant voltage step at the charge cut-off voltage was applied until the current dropped below 0.05C. The evolution of voltage and current during cycling is shown in Figure 2.2. The cells cycled for at least 100 cycles or until the capacity retention dropped below 50%.

Cycling protocol 2 After formation, the cells were charged and discharged ones at a constant current of 0.2C between 4.0 and 3.0V, additionally applying a constant voltage step at the charge cut-off voltage until the current dropped below 0.05C. Followed by cycling at a constant charge/discharge current of 0.5C between 3.0 and 4.0V, again additionally applying a constant voltage step at the charge cut-off voltage until the current dropped below 0.05C. The evolution of voltage and current during cycling is shown in Figure 2.3. The cells cycled for at least 100 cycles or until the capacity retention dropped below 50%.

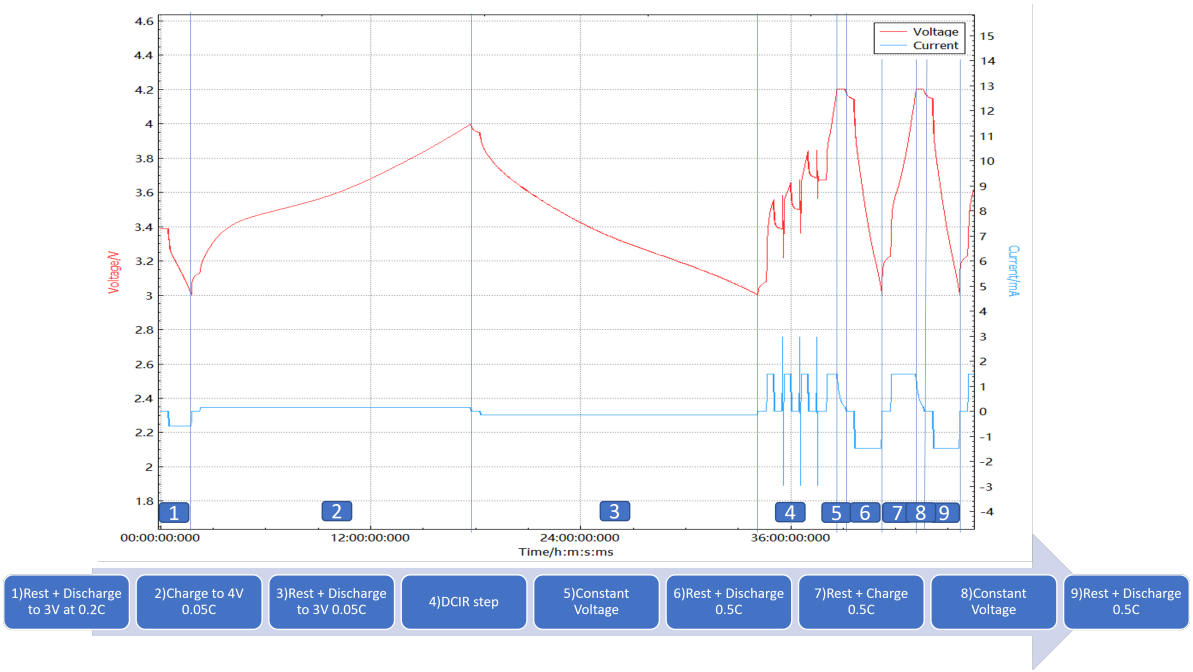

Figure 2.2: Evolution of Voltage and Current during Cycling protocol 1.

Figure 2.3: Evolution of Voltage and Current during Cycling protocol 2.

The instantaneous and diffusive internal resistance was measured after every 25 cycles at a specific SOC by means of implementing a DCIR step into the cycling protocol. Two different protocols were used over the course of the experiments. With the first protocol measurements were performed at 20, 40 and 60% SOC. With the second protocol, measurements were only performed at 50% SOC, so that the measurement takes less time.

DCIR protocol 1 The basic principle of the DCIR test is a current pulse of 18 seconds during charge and during discharge. This protocol was designed for full coin cells and a pulse with a constant current of 1C was applied. Beforehand, the cell was charged at a constant rate of 0.2C for 1h. These two steps were repeated 3 times. The evolution of voltage and current during the DCIR steps is shown in Figure 2.4.

DCIR protocol 2 The basic principle of the DCIR test is a current pulse of 18 seconds during charge and during discharge. This protocol was designed for both full coin and full pouch cells and a pulse with a constant current of 1C was applied. Beforehand, the cell was charged with a constant current of 0.5C up to 3.6V, additionally applying a constant voltage step at 3.6V until the current dropped below 0.05C. The evolution of voltage and current during the DCIR steps is shown in Figure 2.5.

Cyclic voltammetry (CV) was carried out on Si half cells and NMC-622 half cells within a voltage window of 0.01 - 1 V and 3 - 4.2 V, respectively at various scan rates from 0.02 to 0.2 mV/s. CV was performed at room temperature on a LAHNE Battery Testing System type V4.3.

Electrochemical Impedance Spectroscopy (EIS) was performed on full coin cells, full pouch cells and symmetrical coin cells in a two-electrode set-up on Metrohm Autolab and Biologic VSP potentiostats. A frequency range of 100 kHz - 0.1 Hz and an amplitude of 10 mV were applied.

Figure 2.4: Evolution of Voltage and Current during DCIR protocol 1.

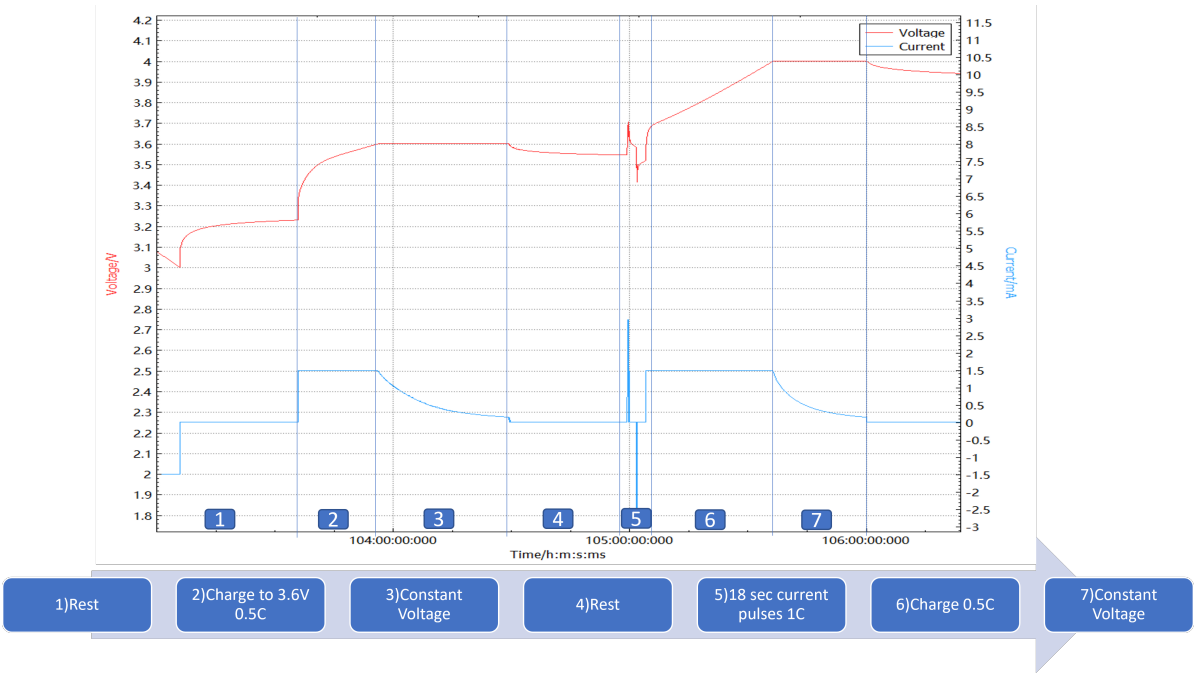

Figure 2.5: Evolution of Voltage and Current during DCIR protocol 3.

3

Results and discussion

3.1. Behaviour of the Si anode investigated by Cyclic Voltammetry

The material that is investigated in this report is the Si anode of LJT, which is in continuous development to optimize its properties and gain market value. Due to the continuous development, the properties of the anode change slightly during the time-frame in which the experiments took place, which may have an effect on for example the porosity of the anode, the conductivity or the silicon utilisation level. If one wants to compare the results of different anode samples with each other, one needs to understand the mechanisms at play in the anode material during lithiation and delithiation. Therefore, the anode material is investigated by Cyclic Voltammetry.

Cyclic voltammograms are obtained of a Si anode half-cell at various scan rates and the results are presented in Figure 3.1. The appearance of the Cyclic Voltammogram corresponds well with the CV scans found in literature [6, 24, 27, 57]. Current peaks are found around 0.32V and 0.50V in the forward scans and around 0.21V and 0.07V in the backward scan, which is well comparable with the peak potentials found in literature.

At the lower scan rates two peaks are visible in both the anodic and the cathodic regime, which relate to the reversible redox reactions taking place in the battery. Amorphous Si reacts upon lithiation in a two-step mechanism from a-Li_xSi into a-$Li_{15}Si_4$ phase as presented in Figure 1.7, which relates to the two backward peaks in the Cyclic Voltammogram. The two forward peaks show the reversibility of the reactions as the reactions described here are reversed and two peaks are again visible.

Another observation is that the peak current becomes larger as the scan rate increases. This can be explained by an increase of the Li-ion concentration gradient, which causes the current, at the anodes surface as the potential is the driving force for the Li-ion migration [13]. More importantly, the peaks merge upon increase of the scan rate, so the two reactions are not distinguishable anymore and at a scan rate higher than 0.06 mV/s the second reaction in the reverse scan does not take place anymore as the reaction cannot be finished within this voltage window as can be seen in Figure A.1.

The lithium diffusion coefficient is determined for both reactions during the forward and reverse scan with the use of Randles-Sevcik equation (1.2). The equation can be rewritten, so that the diffusion coefficient (D_{Li^+}) can be obtained from the slope (m) of Figure 3.2.

$$D_{Li^+} = \left(\frac{m}{0.4463 \cdot nFAC^0}\right)^2 \cdot \frac{RT}{nF} = 5.63 \cdot 10^{-12} \cdot m^2 \tag{3.1}$$

Herein we assumed that the number of electrons participating in the reaction is 1 as lithium transverses from Li^+ to Li, the bulk concentration of the electrolyte salt is 1M, and the apparent electrode surface area is equal to 1553 cm^2. The surface area of the anode (A) was corrected for the porosity of the anode by $A = SSA \cdot m_{Si}$. SSA is the specific surface area of the anode and was determined by means of Brunauer-Emmett-Teller (BET) measurement to be 869680 cm^2/g. The Si deposition was weighed

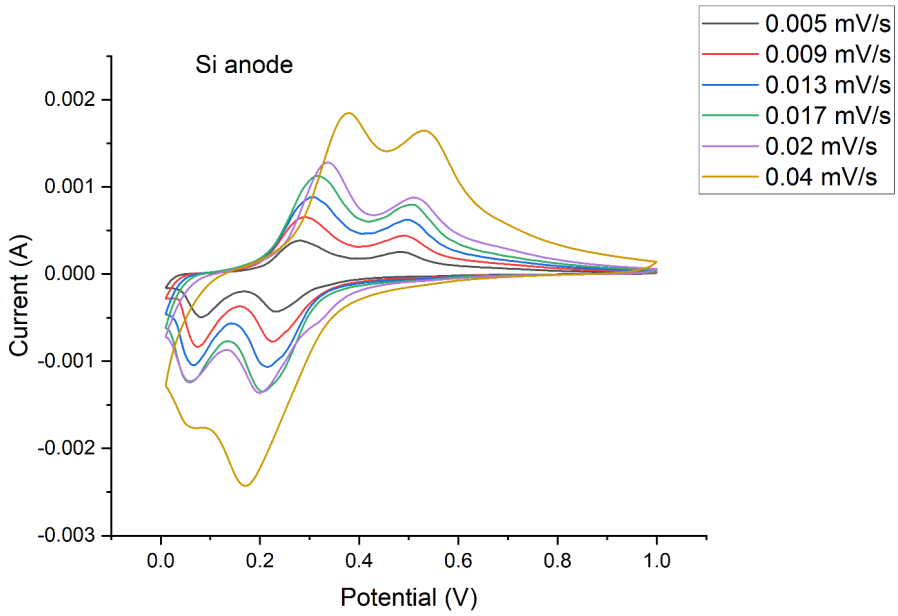

Figure 3.1: Cyclic Voltammogram of Si anode half-cell at various scan rates.

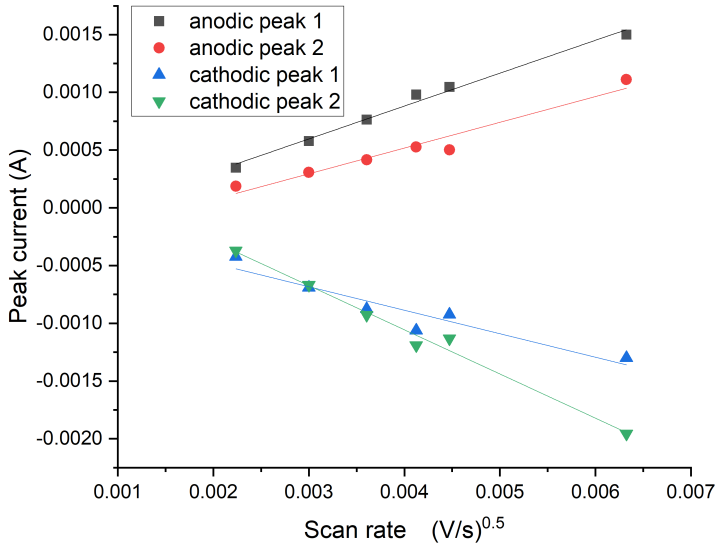

Figure 3.2: Peak currents (two anodic peaks and two cathodic peaks) of the Si anode half-cell cyclic voltammogram versus the square root of the scan rate with a linear fit (with equation $y = ax + b$).

Table 3.1: Diffusion coefficients of lithium during various stages of lithiation and delithiation in the Si anode. Reaction 1 refers to the reaction from a-Si to a-Li_xSi. Reaction 2 refers to the reaction from a-Li_xSi to a-$Li_{15}Si_4$.

	Reaction 1 forward scan	Reaction 2 forward scan	Reaction 2 backward scan	Reaction 1 backward scan
D_{Li^+} (cm^2s^{-1})	4.56E-13	2.80E-13	8.24E-13	2.33E-13

(m_{Si}) to be 1.79 g. Values for m were used as shown in Table A.1. The diffusion coefficients of lithium during various stages of lithiation and delithiation of the anode are shown in Table 3.1. Diffusion during lithiation and during delithiation occurs with similar diffusion rates of around 10^{-13} cm^2s^{-1}.

3.1.1. Discussion on the Cyclic Voltammetry results

It is demonstrated that the Si anodes produced by LJT show the same behaviour as the Si anodes produced by other research groups. Lithiation and delithiation of the Si anode is demonstrated in this work to occur via a two-step process. Thereby, since a two-step process is demonstrated, the model proposed by Jiang et al. [21] in section 1.2.1 can be assumed for the Si anode of LJT. In literature values for D_{Li^+} around 10^{-13} cm^2s^{-1} have been found [27, 57], but also values around 10^{-9} cm^2s^{-1} have been observed [6]. The values found for D_{Li^+} in this research are thus comparable to the values found in literature. Nevertheless, differences may occur do to variation in anode material structure and a critical attitude is recommended for the determination of the apparent electrode surface area and assumptions made for the calculation of the diffusion coefficient.

The Si deposition layers are often manufactured by different layer deposition techniques, which cause a variety in material structure of the anode. A high porosity and large surface area likely enhance the diffusion ability of the Li-ions within the porous Si deposition layer. This statement is supported by the recognition that an amorphous or porous structure allows for a more homogeneous volume expansion and contraction during charge and discharge respectively and many Li-ion diffusion pathways [29]. So it can be assumed that the degree of porosity is an important factor for the ease of Li-ion diffusivity.

Both the Si anode produced by LJT and the Si anodes produced by Kulova et al. [27], Xia et al. [57] and Chen et al. [6] are reported to have an amorphous structure, however, the degree of porosity is not always reported. Chen et al. [6] reported the manufacture of an amorphous Si thin film produced by magnetron sputtering, for which a density of 2.33 g/cm^3 was assumed, which is the density of crystalline Si. Kulova et al. [27] reported the manufacture of a hydrogenated amorphous Si layer with a density of 2.0 - 2.2 g/cm^3. Xia et al. [57] reported the manufacture of an amorphous Si thin film anode prepared by pulsed laser deposition, but no information on the density or porosity of the layer was reported. The Si deposition layer of LJT, which is produced by PECVD, has an approximate density of 1.6 g/cm^3 [12], a porosity of 17% and a specific surface area of 87 m^2/g. Due to the high degree of porosity of the LJT Si anode, a good Li-ion diffusivity is expected and confirmed by the results of this research.

The main bottleneck for the correct calculation of the diffusion coefficient from the CV scans likely is the determination of the apparent electrode surface area. If one assumes the Si deposition layer surface to be a flat surface, one can use the geometry of the anode to determine the dimensions of the anode, which is assumed to be equal to the dimensions of the Si deposition layer. However, we know from measurements within LJT that the Si deposition layer is not a flat surface, but contains pores of various sizes. Within these pores electrolyte might penetrate, thus causing the specific surface area available for Li-ion diffusion to be higher than the geometric surface area of the anode. Therefore, the apparent surface area was corrected with the specific surface area of the anode.

Unfortunately, in literature it is rarely reported which values are taken for the apparent electrode surface area and whether the area is corrected for the porosity of the anode. The surface area might differ according to different assumptions on the apparent surface area with a factor 3, and consequently the calculated Li-ion diffusion coefficient might also vary with a factor 10^{-6} ($= \frac{1}{1000^2}$). If D_{Li^+} was calculated with A being the geometric surface area (= 1.266 cm^2), than the diffusion coefficients would be in the order of 10^{-7}. The difference is significant, which makes it hard to draw a valid comparison with literature without the knowledge on the specifics of the calculation.

What is often reported are the peak currents and the dependence of the peak currents on the square root of the potential scan rate and the corresponding linear fit. What is noticeable is that in two articles by Xia et al. [57] and Chen et al. [6] the linear fit goes through the origin, contrarily to the fits performed in this report. Therefore, at the lower scan rates, the data points do not correspond well to the fit, and the slope of the fit differs from the slope obtained if the fit did not go through the origin. Consequently, a significantly different diffusion coefficient can be obtained.

Furthermore, Xia et al. [57] reported the use of scan rates of 0.1 – 2.0 mV/s. In our experiments it was observed that the two peaks merge at a scan rate higher than 0.4 mV/s and the reaction in the backward scan cannot be finished anymore before the cut-off potential is reached. Hence, the peak current cannot be measured anymore in the backward scan as only a part of the peak is now visible. Therefore, the data points at the higher scan rates are not reliable as they do not show the actual peak current. Lower scan rates need to be adopted to make sure the reactions are finished within the voltage window and a distinction can be made between the two reactions in the case of a two-step process.

3.2. Cycling behaviour of linear carbonate solvents

In section 3.1 the behaviour of the Si anode during lithiation and delithiation was investigated. In the next sections, the knowledge gained from section 3.1 can be used to analyse the effect of the adaptation of the electrolyte composition on the cycling performance of the battery. In the following section, section 3.2.1, linear carbonate solvents, DEC, DMC and EMC, will be compared with each other. Afterwards, in section 3.2.2, the effect of the attendance of VC and FEC in the electrolyte composition will be investigated.

3.2.1. Cycling behaviour of pure solvents

One type of solvent plus one type of electrolyte salt forms the basis of the most simple electrolyte composition, hence a good starting point for the development of an electrolyte with a beneficial composition. Long term charge/discharge cycling experiments were performed on Si/NMC-622 full coin cells to investigate the effect of three types of linear carbonate solvents, pure DEC, pure DMC and pure EMC, on the cycling behaviour of the battery. Figure 3.3a and b show the cycling behaviour and Coulombic Efficiency (CE), which is defined as the discharge capacity of the n^{th} cycle over the charge capacity of the n^{th} cycle, of the batteries at a constant current rate of 0.5C according to cycling protocol 1. Figure 3.3a shows the specific charge and discharge capacities during the cycle life of the batteries. Figure 3.3b shows on the left axis the capacity retention of the batteries and on the right axis the CE of the batteries during its cycle life. The average CE over 20 cycles is 93.55%, 97.36% and 63.31% for EL1, EL2 and EL3.

All batteries display a rapid capacity fade and a low initial specific capacity. EL1 shows an initial capacity of 1082 mAh/g of Si anode, and after 20 cycles the capacity remains of 55.2% compared to the initial capacity. EL2 shows an initial capacity of 1042 mAh/g of Si anode, and after 20 cycles the capacity remains of 74.9% compared to the initial capacity. EL3 shows an initial capacity of 1029 mAh/g of Si anode, and after 20 cycles the capacity remains of 5.83% compared to the initial capacity. This quick capacity fade is likely related to the formation of an unstable interphase on the electrode's surface and high irreversible capacity losses due to continuous reduction of the electrolyte solvent and salt on the anode side, which results in isolation of Si particles from the electrode and consumption of Li-ions by the decomposition reactions of the electrolyte and entrapment of Li inside Si particles [19, 47].

It has been reported that decomposition of DEC in the presence of PF_6 is significantly more pronounced than the decomposition of DMC [44]. $LiPF_6$ is reported to have poor thermal stability and facilitates decomposition reactions of dialkyl carbonates [44]. The thermal decomposition of $LiPF_6$ in pure DEC, pure DMC and pure EMC will result in a range of decomposition products, among which the well-known decomposition into LiF and PF_5 [44]. The more pronounced decomposition of DEC could explain a quicker capacity fade for EL3.

The fluctuations in CE are attributed to temperature fluctuations during the time-frame of the test, which occur as the batteries were tested at room temperature. The fluctuations in CE as a results of the temperature fluctuations can be explained with the use of the Nernst equation (eq. (1.1)). As the temperature increases, the overpotential, which is the difference between the equilibrium potential

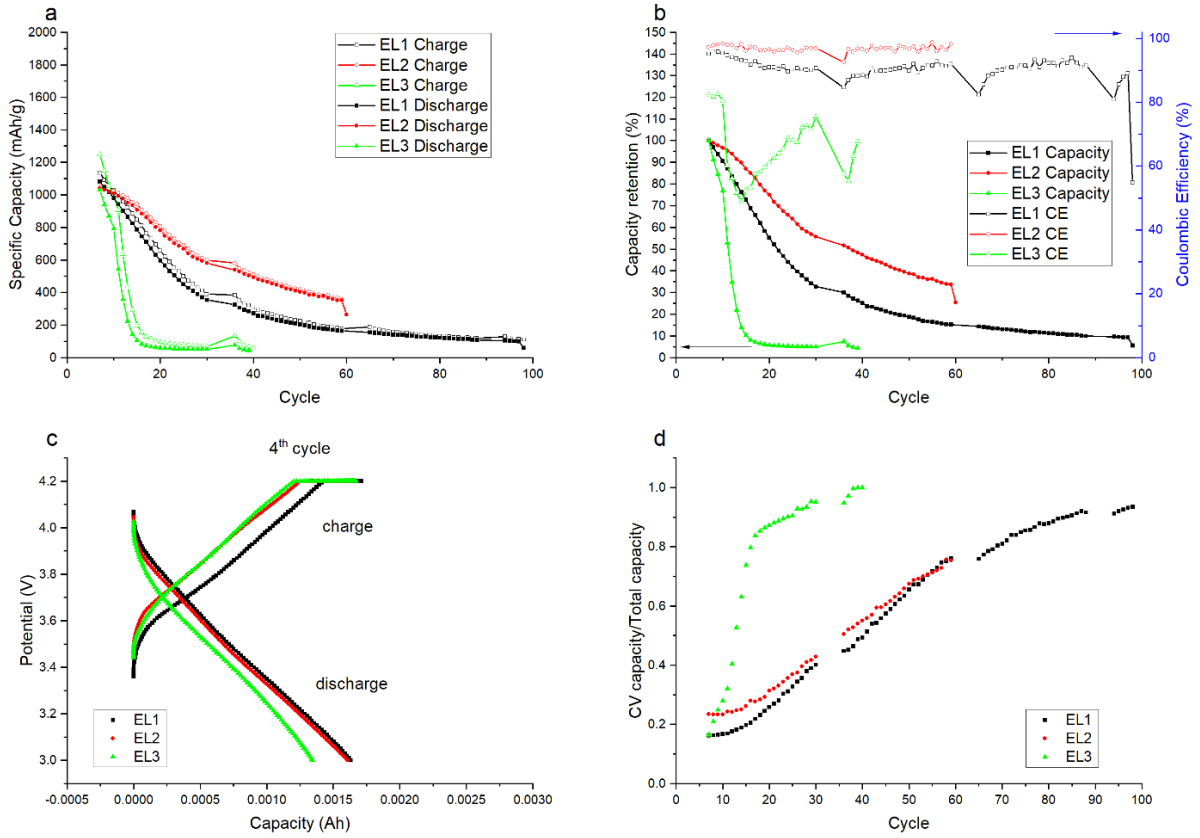

Figure 3.3: Cycling behaviour of full coin cells charged and discharged at a constant current of 0.5C between 3.0 and 4.2V with the following electrolyte compositions: 1M LiPF6 in pure DEC, 1M $LiPF_6$ in pure DMC, 1M $LiPF_6$ in pure EMC. a) Cycling performance b) Cycling performance (left axis) and coulombic efficiency profiles (right axis) of full coin cells at a 0.5C rate c) charge/discharge curves at a rate of 0.5C of the 4^{th} cycle d) Change in time of contribution of capacity gained during constant voltage step with respect to the total capacity.

(E_{eq}) and the standard potential (E^0), decreases. Thus the redox reaction occurs already at a lower potential, and hence a higher capacity can be obtained. So, if the temperature fluctuates upon charge and discharge, the total capacity that can be inserted in or extracted from the battery also fluctuates and these fluctuations are pronounced in the CE curves as the CE is calculated by dividing the discharge capacity over the charge capacity.

Small interruptions followed by a small increase in capacity can be seen in the cycling profiles, because cycling protocol 1 includes one cycle at a low current rate of 0.05C between 3.0 and 4.0V prior to the DCIR measurements. The CE during this cycle was higher than 100%, which means that the cell could be discharged further than it was charged. This is supported by the appearance of a lower over-potential during the cycle at low current rate. Therefore, it is possible that during this slow rate cycle more Li-ions got released from the anode, causing more active Li-ions to be present in the cell again. Thus, the cell recovered some capacity and during the following cycles a slightly higher capacity is observed. This behaviour can be seen throughout all cycling tests we performed for the purpose of this thesis and thus all can be explained by prior DCIR measurements.

Figure 3.3c displays the charge/discharge profiles during the 4th cycle during long term charge/discharge cycling of three batteries containing electrolytes with varying compositions. The charge/discharge curves show typical behaviour for a LIB with a NMC cathode and a Si anode. Nevertheless, two properties stand out: Firstly, the horizontal plateau at the upper end of the charge profile, which can be explained by the constant voltage step at the end of charge. Secondly, the potential increase at a capacity of 0 Ah for both the charge and the discharge profiles. This can be explained by the half an hour rest of the battery after every charge and discharge step, which causes the potential to shift towards the equilibrium potential. Similar properties can be observed throughout this thesis in all other cycling tests performed.

Figure 3.3d shows the contribution of capacity gained during the constant voltage step with respect to the total capacity. The high contribution of the capacity gained during the constant voltage step directly relates to the quick capacity fade of the battery during cycling, since the cut-off potential is reached earlier. Therefore, the over-potential that is required to charge the battery becomes higher when the capacity retention drops below 100%, which relates to the loss of active material that can take up Li-ions. Thus, the contribution of capacity gained during the constant voltage step becomes larger, which relates to a higher resistance in the battery at a 100% SOC. The higher resistance is likely caused by the same processes that cause quick capacity fade, namely the formation of an unstable interphase.

3.2.2. Cycling behaviour in attendance of Vinylene Carbonate, Fluoroethylene Carbonate and Adiponitrile

Long term charge/discharge cycling experiments were performed on Si/NMC-622 full coin cells to investigate battery behaviour with an electrolyte composed of a linear carbonate solvent (DEC, DMC, and EMC) with the attendance of additives (VC, FEC and AN). Studies by Chen et al. [7] and Choi et al. [9], have explored that VC and FEC additives can enhance the cycle performance of a LIB for Si anode, where a smooth and uniform SEI is formed, containing stable compounds in the presence of FEC. In recent research, VC and FEC are regarded as the most common additives and FEC is even regarded up to now as the best performing additive for LIB with a Si anode [14, 18, 37, 64]. AN was chosen, because of its positive effects on the cathode. Lee et al. [30] reported a strong coordination between Ni^{4+} and the nitrile group in AN, which can reduce the parasitic reactions between the electrolyte and Ni-rich (NMC) cathode, and Li et al. [32] reported the good electrochemical stability of AN at high voltages.

Figure 3.4a and b show the cycling behaviour and CE of the batteries at a constant current rate of 0.5C according to cycling protocol 1. It can be seen that EL4 shows an initial capacity of 1113 mAh/g of Si anode, and after 100 cycles the capacity remains of 76.2% compared to the initial capacity. EL5 shows an initial capacity of 1284 mAh/g of Si anode, and after 100 cycles the capacity remains of 78.2% compared to the initial capacity. EL6 shows an initial capacity of 1513 mAh/g of Si anode, and after 100 cycles the capacity remains of 86.6% compared to the initial capacity. The average CE over 100 cycles is 99.10%, 99.60% and 99.63% for EL4, EL5 and EL6 respectively.

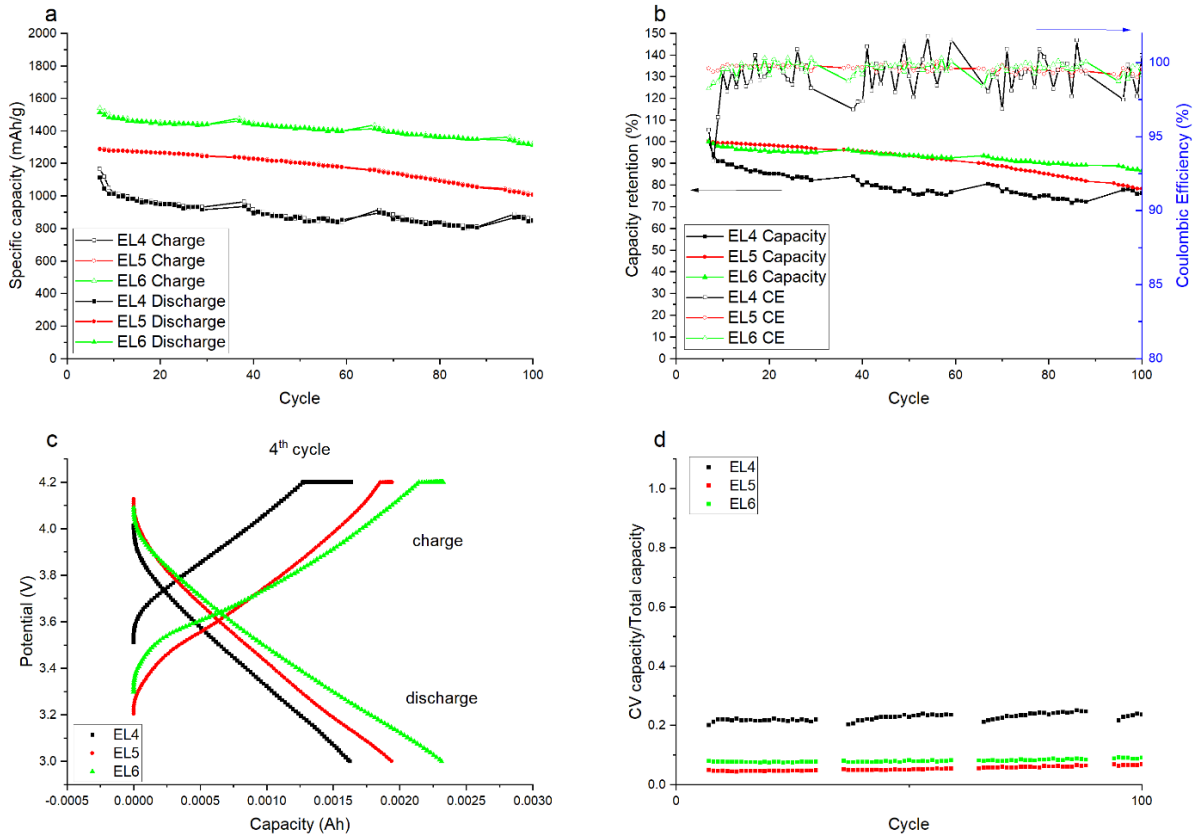

Figure 3.4: Cycling behaviour of full coin cells charged and discharged at a constant current of 0.5C between 3.0 and 4.2V with the following electrolyte compositions: 1M $LiPF_6$ in pure DEC 2 wt% AN 5 wt% FEC 2 wt% VC, 1M $LiPF_6$ in pure DMC 2 wt% AN 5 wt% FEC 2 wt% VC, 1M $LiPF_6$ in pure EMC 2 wt% AN 5 wt% FEC 2 wt% VC. a) Cycling performance b) Cycling performance (left axis) and coulombic efficiency profiles (right axis) of full coin cells at a 0.5C rate c) charge/discharge curves at a rate of 0.5C of the 4^{th} cycle d) Change in time of contribution of capacity gained during constant voltage step with respect to the total capacity.

A large spread in initial specific capacity is shown in Figure 3.4a. EL4 and EL5 show a significantly lower initial specific capacity compared to EL6. An explanation for this behaviour can stem from the process conditions of the Si anodes. As the Si anodes produced by LJT are continuously in development, the properties of the anode might differ per sample. The Si utilisation level of the anode material used for EL4 and EL5 are much lower, which can be caused by differences in porosity for example.

The capacity retention, however, of these batteries shows that the cycle life of the LIB with Si anode can be enhanced significantly by using FEC and VC additives. Since the additives have a higher reduction potential than the solvents (0.46V and 0.51V, for VC and FEC respectively, and 0.1V, for EMC and DMC, and 0.07V, for DEC), the additives are reduced before the other components in the electrolyte to form a passivating layer over the electrode's surface. The function of this passivating layer is to prevent further decomposition of the electrolyte components and to allow for Li-ion transport towards the electrode and block electrons from the electrode [45]. Therefore, it is likely that enhanced cycle life can be attributed to the formation of a stable SEI by the decomposition of the additives on the anode, resulting in much lower irreversible capacity losses.

Figure 3.4c and d show the charge/discharge profiles during the 4^{th} cycle and the contribution of capacity gained during constant voltage step with respect to the total capacity during long term charge/discharge cycling of three batteries containing electrolytes with varying compositions. The charge/discharge curves show typical behaviour for a LIB with a NMC cathode and a Si anode. Figure 3.4d shows a lesser contribution of the constant voltage step over time than we observed in Figure 3.3d and a much more stable behaviour over time, indicating a lower resistance at the end of charge. A higher total capacity can be reached and the relative contribution of the capacity gained during the constant voltage step is lower, because the cut-off potential is reached after a longer charging time, so the stable behaviour of the batteries is likely related to a longer capacity retention of the battery and a lower over-potential.

3.2.3. Discussion on the cycling behaviour of linear carbonate solvents

In section 3.2.1 a quick capacity fade for all four different electrolyte compositions was observed, which is likely related to the formation of an unstable interphase on the electrodes surface, large irreversible capacity losses due to continuous reduction of the electrolyte solvent and salt on the anode side and isolation of Si particles from the electrode. This, in turn, results in consumption of Li-ions by the decomposition reactions of the electrolyte and entrapment of Li inside Si particles. However, we cannot know for sure what the cause of the capacity fade is without investigating the batteries further after degradation. The above stated hypothesis can be confirmed by using post-mortem techniques, techniques used after the cell has failed. Possibilities are gas analysis of the gas produced after formation, to confirm the presence of gaseous decomposition products of the electrolyte compounds, X-ray diffraction (XRD) on the cathode to prove the loss of active Li^+ and scanning electron microscopy (SEM) to show the isolation of Si particles from the Cu current collector.

In section 3.2.2 it is observed that the cycle life of the LIB is elongated from a capacity retention of approximately 75% after 20 cycles to approximately 76% after 100 cycles in the attendance of additives in the electrolyte mixture. This is likely attributed to the formation of a more stable and insulating SEI layer, which is likely also thinner. An analysis on the morphology and composition of the SEI layer has not been performed in this research, but would certainly give more information on the properties of the SEI layer. A first indication of a stable and insulation SEI would be a uniform morphology [45], which can be observed by SEM, and with the use of cross-section SEM the thickness of the SEI layer can be determined as well as with the use of Scanning Spreading Resistance Microscopy (SSRM) [48]. A more in-depth understanding can be obtained by exploiting X-ray photoelectron spectroscopy (XPS) and nuclear magnetic resonance spectroscopy (NMR) to investigate the type of decomposition products formed [46].

Additionally, the choice for an additive compound can also stem from the intended application of the battery. Depending on the application of the battery, the requirements for the battery will change. For example, the battery pack in an electric car needs to be lightweight and of a high energy density to extend the driving range. FEC and VC additives can prolong the thermal stability from 150˚C up to 200˚C according to a study by Profatilova et al. [43]. Therefore, the use of these additives might be suitable for a range of high-temperature applications, like batteries used for geological drilling equipment.

Nevertheless, some shortcomings to the use of VC and FEC additives are also reported in literature. Kim et al. [26] reported the obstruction of good Li-ion transport at high current rates by a densely structured SEI formed from the decomposition products of VC, leading to poor kinetics. Additionally, it is reported that the Ohmic resistance increases at high concentrations of VC, which results in a low cycling efficiency and a high self-discharge rate [14]. Moreover, upon rapid consumption of FEC during charge and discharge cycles, the FEC reservoir might be depleted, which causes sudden battery failure [14]. Therefore, to overcome these shortcomings, further optimization of the electrolyte composition is recommended.

3.3. Cycling behaviour of Cosolvents: Cyclic carbonates

In this section cosolvents, PC and EC, are added to the electrolyte mixture, because of a presumed synergistic effect of the cyclic and linear carbonates. The linear carbonates lower the viscosity, thereby promoting ion transport, and the cyclic carbonates raise the dielectric constant and the boiling point [58]. Simultaneously, they prevent the decomposition of the linear carbonates, since the cyclic carbonates have a higher reduction potential than the linear carbonates [58]. PC is expected to be favourable to use compared to EC, because it is reported to improve battery performance in a wide temperature range [22, 54, 63] due to a low melting point, a high boiling point and a high dielectric constant [58]. In graphite PC is not used, because of the exfoliation of the graphite layers on the anode due to this cosolvent [15], but in this experiment only pure Si is used, eliminating the latter problem. The question remains whether PC as a cosolvent also benefits the cycle performance of the LIB with Si anode at room temperature.

The electrolyte is DEC-based with added VC, FEC and AN, as best results were obtained for this electrolyte composition in section 3.2.2. Long term charge/discharge cycling experiments were performed on Si/NMC-622 full coin cells with four different electrolyte compositions: EL6, EL7, EL8 and EL9. Figure 3.5a and b show the cycling behaviour and CE of the batteries at a constant current rate of 0.5C according to cycling protocol 1. EL7 shows an initial capacity of 1769 mAh/g of Si anode, and after 20 cycles the capacity remains of 65.4% compared to the initial capacity. EL8 shows an initial capacity of 1874 mAh/g of Si anode, and after 100 cycles the capacity remains of 59.16% compared to the initial capacity. EL9 shows an initial capacity of 1763 mAh/g of Si anode, and after 100 cycles the capacity remains of 78.8% compared to the initial capacity. The average CE over 50 cycles is 99.63%, 98.11%, 99.44% and 99.56% for EL6, EL7, EL8 and EL9 respectively.

The cycling behaviour of EL8 shows a higher specific capacity compared to EL6, EL7 and EL9 during the first 80 cycles. This higher capacity of EL8 might be attributed to the preference for PC solvation over EC solvation by Li-ions, as described by Von Wald Cresce et al. [52], which suggests that the Li^+-PC interaction is stronger than the Li^+-EC interaction and thus more Li-ions might be solvated in PC. Hou et al. [20] relates the contribution of solvated Li-ions to the capacity of the battery, as more solvated Li-ions results in better ion transport ability. Therefore, with a better ion transport ability, it is likely that the higher capacity of the battery is related to the preference of Li-ions to form solvation separated ion pairs with PC molecules.

Still, capacity fade of EL8 is occurring after 80 cycles. A possible explanation can be the small difference in molecular structure of PC compared to EC. The presence of the methyl group of PC is reported to increase the size of the cavities in the SEI structure, which was modelled with the use of a hybrid Monte Carlo (MC)/ molecular dynamics (MD) reaction method [51]. Therefore, electrolyte can penetrate more easily through the SEI layer and reach the anode surface, where irreversible reactions take place that cause loss of active lithium. EC-based electrolyte, on the other hand, is reported to form a more dense SEI structure, with smaller cavities, prohibiting in a larger extent the penetration of electrolyte [51].

EL7 shows quick capacity fade in a very early stage. This is likely related to the ratio of cyclic carbonate solvents to linear carbonate solvents (2:1 in EL7) which is higher than the ratios for EL8 and EL9. A reason for capacity fade could be weaker Li^+-FEC interaction compared to Li^+-EC described by Hou et al. [20] and thus even weaker compared to Li^+-PC. Hou et al. [20] argue that in order for FEC to preferentially decompose, and form the SEI layer, earlier than PC and EC, FEC needs to be coordinated with Li-ions. So, in the presence of an excess of cyclic carbonate solvents molecules, PC and EC might decompose instead of FEC, if during the first cycles not enough FEC is coordinated with Li-ions,

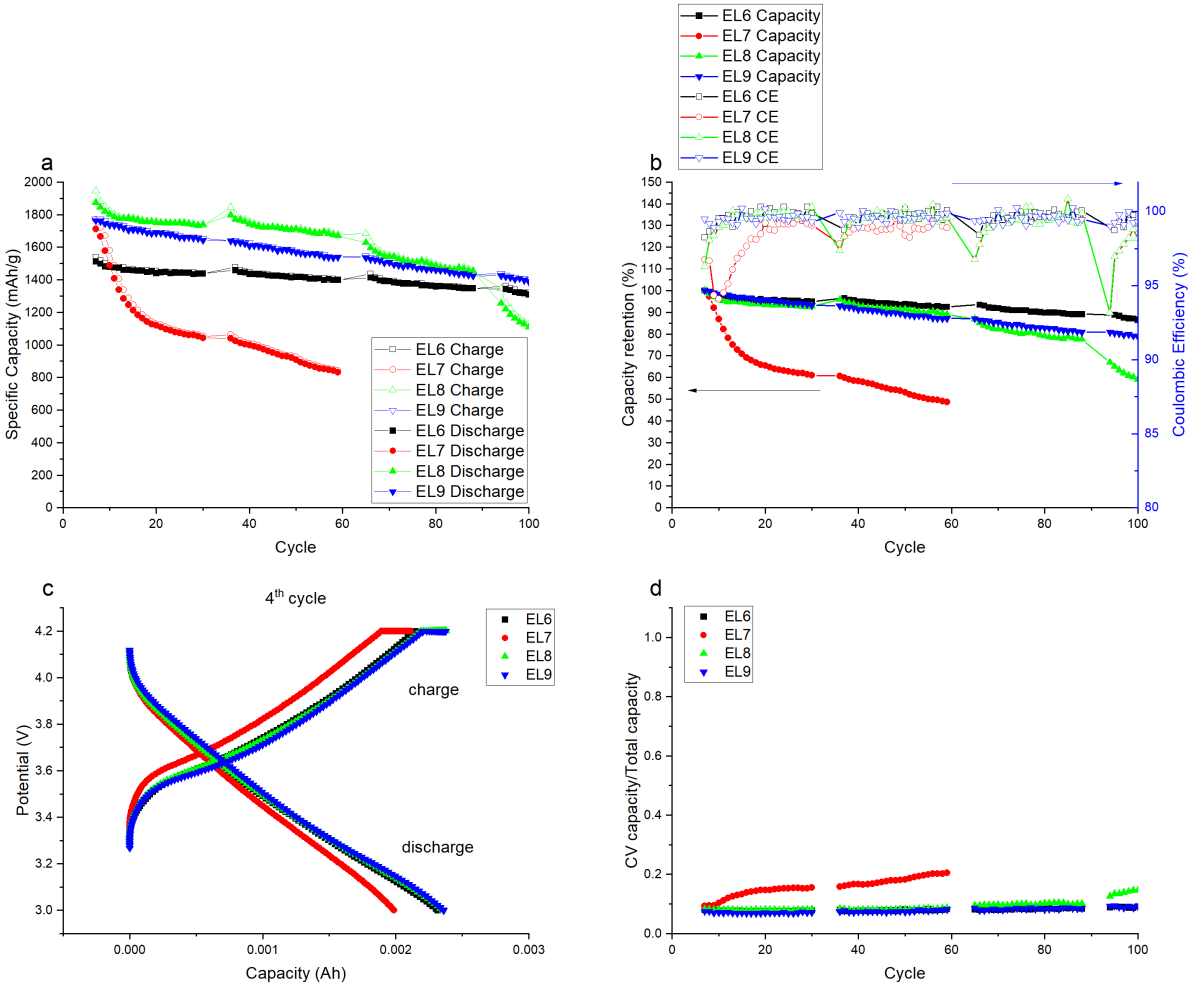

Figure 3.5: Cycling behaviour of full coin cells charged and discharged at a constant current of 0.5C between 3.0 and 4.2V with the following electrolyte compositions: 1M $LiPF_6$ in EC:DEC (1:1 vol%) 2 wt% AN 5 wt% FEC 2 wt% VC, 1M $LiPF_6$ in PC:DEC (1:1 vol%) 2 wt% AN 5 wt% FEC 2 wt% VC, 1M $LiPF_6$ in PC:EC:DEC (1:1:1 vol%) 2 wt% AN 5 wt% FEC 2 wt% VC, 1M $LiPF_6$ in pure DEC 2 wt% AN 5 wt% FEC 2 wt% VC. a) Cycling performance b) Cycling performance (left axis) and coulombic efficiency profiles (right axis) of full coin cells at a 0.5C rate c) charge/discharge curves at a rate of 0.5C of the 4^{th} cycle d) Change in time of contribution of capacity gained during constant voltage step with respect to the total capacity.

resulting in capacity fade.

Figure 3.5c displays the charge/discharge profiles during the 4th cycle during long term charge/discharge cycling of four batteries containing electrolytes with varying compositions. The charge/discharge curves show typical behaviour for a LIB with a NMC cathode and a Si anode. The slightly different curve of EL7 is related to the quick capacity fade of the battery as in the fourth cycle a lower charge and discharge capacity was gained. This results in a shift of the curve towards lower capacities at similar potentials.

Figure 3.5d displays the contribution of capacity gained during constant voltage step with respect to the total capacity during long term charge/discharge cycling of four batteries containing electrolytes with varying compositions. The high contribution of capacity gained during the constant voltage step for EL7 is related to the quick capacity fade of the battery, because the overpotential rises and active material is lost. EL6, EL8 and EL9 show similar, stable, behaviour. No significant change is observed in the contribution of capacity gained during the constant voltage step and thus also no significant change in the resistance of the battery over time.

3.3.1. Discussion on the cycling behaviour of Cosolvents

It was assumed that altering the SEI is the main contributor to reach a long cycle life, but in this section another hypothesis is formed. The capacity that the battery can deliver might also be influenced by the conductivity or resistivity of the bulk electrolyte. To make the most use of the theoretical capacity that the Si anode can reach, the conductivity and the ease of Li-ions to migrate between the anode and the cathode can be large contributors. Still, it is observed that less capacity is retained after 100 cycles when cosolvents are added to the electrolyte mixture, so the preferential reduction of electrolyte compounds that form preferable SEI species is nevertheless assumed to be a large contributor, but this preferential reduction might be influenced by the preferential coordination of the sacrificial additives with the Li-ions.

A solutions conductivity is known to be affected by the dielectric constant, the viscosity and the acceptor number and the donor number of the solutions compounds [50]. Dissolution of salt in a solvent is largely determined by ionic bonding, which is caused by the dielectric constant of the compounds. A compound with a high dielectric constant can typically cause a strong ionic bonding. Additionally, the solubility is related to the dissolution heat, solvents with a small dissolution heat have a high solubility. Therefore it is important to select solvents with a low viscosity, a high dielectric constant and an affinity for accepting or donating an electron pair. Besides, a small molecular volume is mentioned as a beneficial factor for high solubility [50].

To gain more insight into the mechanisms behind the solvation of the electrolyte salt, molecular models can be adopted. For example, Von Wald Cresce et al. [52] implemented quantum chemistry calculations and molecular dynamics simulations to explain preferential solvation of Li-ions by PC versus EC and a combination of classical molecular dynamics and quantum chemical calculations was adopted by Hou et al. [20] to investigate the influence of FEC on the electrolyte composition. The conductivity of a solution can also be determined by simple conductivity measurements. However, the relative contributions of different compounds within the electrolyte will not be known by this measurement, nor will be the preferential coordination of the salt with any of the electrolyte's compounds.

3.4. Cycling behaviour of other additives

To enhance the properties of the electrolyte and the cycling performance of the LIB further, three other additives are introduced, diallyl pyrocarbonate (DAPC), dimethylacrylamide (DMAA) and (2-cyanoethyl)triethoxysilane (TEOSCN). These three additives are chosen, because of two properties that an additive should have, the ability to form flexible polymers and the accommodation of good ionic conductivity. Flexible polymers commonly have no or only few cross-links in their chain and a low molar mass. Good ionic conductivity can be obtained by among others, a low viscosity of the electrolyte, a preferential solvation of Li-ions with the solvent or additive molecules and the formation of highly conductive species.

The DMAA additive is expected to enhance the ionic conductivity of the electrolyte, due to preferential solvation of Li-ions by DMAA molecules, and promote the formation of a uniform and stable SEI

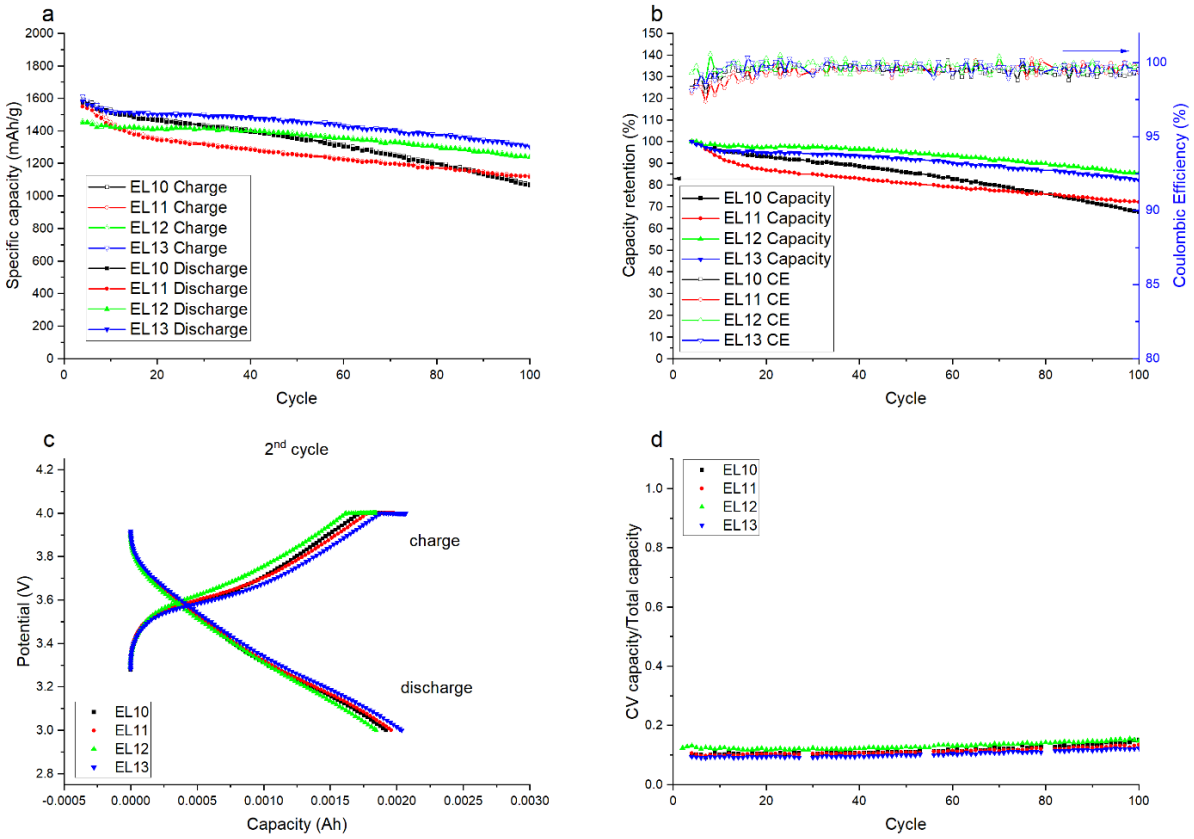

Figure 3.6: Cycling behaviour of full coin cells charged and discharged at a constant current of 0.5C between 3.0 and 4.0V with the following electrolyte compositions: 1M $LiPF_6$ in EC:DEC (1:1 vol%) 2 wt% AN 5 wt% FEC 1 wt% VC, 1M $LiPF_6$ in EC:DEC (1:1 vol%) 2 wt% AN 5 wt% FEC 1 wt% VC 1 wt% DAPC, 1M $LiPF_6$ in EC:DEC (1:1 vol%) 2 wt% AN 5 wt% FEC 1 wt% VC 1 wt% DMAA, 1M $LiPF_6$ in EC:DEC (1:1 vol%) 2 wt% AN 5 wt% FEC 1 wt% VC 1 wt% TEOSCN. a) Cycling performance b) Cycling performance (left axis) and coulombic efficiency profiles (right axis) of full coin cells at a 0.5C rate c) charge/discharge curves at a rate of 0.5C of the 2nd cycle d) Change in time of contribution of capacity gained during constant voltage step with respect to the total capacity.

layer that effectively passivates the Si anode surface [67]. The TEOSCN additive in the electrolyte is expected to result in a thin SEI with a low amount of organic species, and thus better chemical and mechanical stability due to low solubility and high shear strength of the inorganic species. Furthermore, the addition of TEOSCN is also expected to enhance the ionic conductivity, as this molecule allows for the formation of highly conductive Li_3N [2]. DAPC, as deduced from the properties ascribed to the compound by a patent of Azagarsamy et al. [3], is expected to form a polymer-rich SEI with good ionic transport properties. The long term charge/discharge experiments were performed in both full coin cells and later in full pouch cells to confirm the data obtained from the full coin cells.

3.4.1. Cycling behaviour of other additives in full coin cells

Long term charge/discharge cycling experiments were performed on Si/NMC-622 full coin cells according to cycling protocol 2 to investigate the effect of three other additives, DAPC, DMAA and TEOSCN, on the cycling behaviour of the battery. As a reference an electrolyte consisting of 1M $LiPF_6$ in EC:DEC (1:1 vol%) 2 wt% AN 5 wt% FEC 1 wt% VC is chosen, because of the good results obtained with this composition in the earlier experiments. The concentration of VC was reduced to 1 wt%, because of two reasons; in an experiment by LJT, where the concentration of VC was varied, a concentration of 1 wt% VC gave the best results; and VC has the same functionality as the other additives, so in order to give a fair comparison with the other additives, of which we add 1 wt%, the same concentration of VC is added.

Figure 3.6a and b show the cycling behaviour and CE of the batteries at a constant current rate of 0.5C. EL10 shows an initial capacity of 1573 mAh/g of Si anode, and after 100 cycles the capacity

remains of 67.7% compared to the initial capacity. It can be seen that EL11 has a capacity retention of 72.2% after 100 cycles compared to the initial capacity, EL12 has a capacity retention of 85.4% after 100 cycles compared to the initial capacity and EL13 has a capacity retention of 82.2% after 100 cycles compared to the initial capacity. The utilisation capacity of Si at the initial cycle is 1546 mAh/g, 1448 mAh/g and 1581 mAh/g for EL11, EL12 and EL13 respectively. The average CE over 100 cycles is 99.41%, 99.42%, 99.70% and 99.62% for EL10, EL11, EL12 and EL13 respectively.

Unlike the other electrolyte compositions, EL11 shows a drop in capacity during the initial cycles. Likely a significant amount of active Li is lost during these cycles due to the decomposition reactions of the electrolyte components. Despite, all additives increase the slope of the capacity retention curve compared to EL10 and, consequently, a higher capacity retention after 100 cycles is observed. The increased slope is likely related to the formation of a more stable and flexible SEI layer that allows for less detrimental irreversible side reactions.

Figure 3.6c and d show the charge/discharge profiles during the second cycle and the contribution of capacity gained during constant voltage step with respect to the total capacity during long term charge/discharge cycling of four batteries containing electrolytes with varying compositions. The charge/discharge curves show typical behaviour for a LIB with a NMC cathode and a Si anode. The change in contribution of the constant voltage charge capacity over the total charge capacity in time is very comparable for all four electrolyte compositions, however the contribution of EL11 is slightly higher, because the initial contribution is higher. This is likely due to the lower initial capacity of 1448 mAh/g compared to the other electrolyte compositions, since it is observed that a lower Si utilisation level results in a higher contribution of the constant voltage charge capacity to the total capacity.

3.4.2. Cycling behaviour of other additives in full pouch cells

The experiment in section 3.4.1 was repeated in pouch cells to validate the results found in the coin cell experiment. Long term charge/discharge cycling experiments were performed on Si/NMC-622 full pouch cells according to cycling protocol 2 to investigate the effect of three other additives, DAPC, DMAA and TEOSCN, on the cycling behaviour of the battery. Figure 3.7a and b display the cycling behaviour and CE of the batteries at a constant current rate of 0.5C.

EL10 shows an initial capacity of 1799 mAh/g of Si anode, and after 100 cycles the capacity remains of 84.2% compared to the initial capacity. It can be seen that EL11 has a capacity retention of 90.8% after 100 cycles compared to the initial capacity, EL12 has a capacity retention of 55.6% after 100 cycles compared to the initial capacity and EL13 has a capacity retention of 79.1% after 100 cycles compared to the initial capacity. The utilisation capacity of Si at the initial cycle is 1762 mAh/g, 1740 mAh/g and 1805 mAh/g for EL11, EL12 and EL13 additive respectively. The average CE over 100 cycles is 99.74%, 99.85%, 99.07% and 99.65% for EL10, EL11, EL12 and EL13 respectively.

The pouch cell results do not entirely confirm the results obtained by the coin cell data. EL13 follows the same trend as EL10. EL12 diverges from the trend and shows capacity fade already after approximately 30 cycles. A cause for this quick capacity fade could be the relatively little amount of electrolyte, 3 g/Ah, present in a pouch cell compared to a coin cell with 25 g electrolyte/Ah. It is demonstrated on Li metal half cells that an excess of electrolyte can extend the cycle life, since it takes longer before all electrolyte is reacted in irreversible side reactions [8, 33]. Since, in pouch cells no excess of electrolyte is present, it is likely that the SEI formed in the presence of DMAA did not prevent irreversible side reactions that have resulted in capacity fade . Nevertheless, EL11 does confirm the coin cell data, since an enhanced cycling performance compared to EL10 is observed.

Figure 3.7c and d display the charge/discharge profiles during the second cycle and the contribution of capacity gained during constant voltage step with respect to the total capacity during long term charge/discharge cycling of four batteries containing electrolytes with varying compositions. The charge/discharge curves show typical behaviour for a LIB with a NMC cathode and a Si anode. The change in contribution of the constant voltage charge capacity over the total capacity in time is very comparable for all four electrolyte compositions. The increase in the contribution of the constant voltage charge capacity that can be seen for EL12 is related to the capacity fade of the cell during cycling.

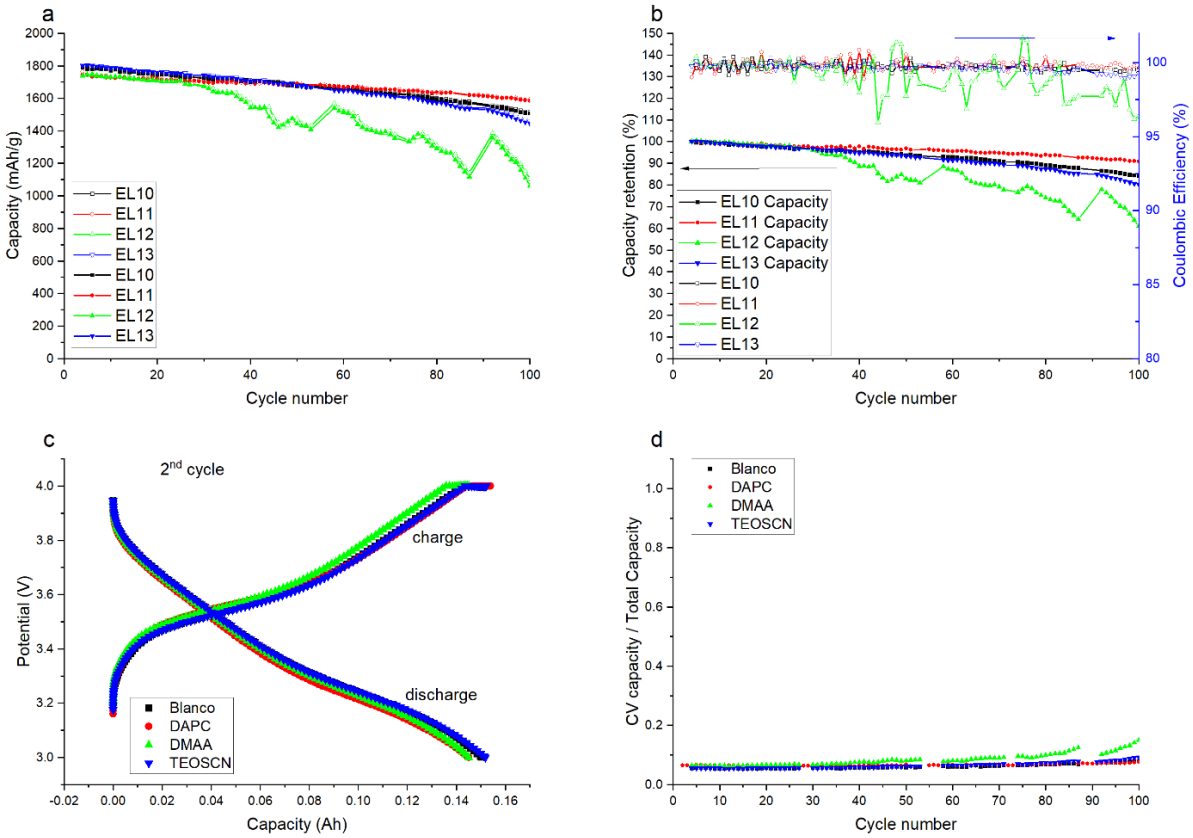

Figure 3.7: Cycling behaviour of full pouch cells charged and discharged at a constant current of 0.5C between 3.0 and 4.0V with the following electrolyte compositions: 1M $LiPF_6$ in EC:DEC (1:1 vol%) 2 wt% AN 5 wt% FEC 1 wt% VC, 1M $LiPF_6$ in EC:DEC (1:1 vol%) 2 wt% AN 5 wt% FEC 1 wt% VC 1 wt% DAPC, 1M $LiPF_6$ in EC:DEC (1:1 vol%) 2 wt% AN 5 wt% FEC 1 wt% VC 1 wt% DMAA, 1M $LiPF_6$ in EC:DEC (1:1 vol%) 2 wt% AN 5 wt% FEC 1 wt% VC 1 wt% TEOSCN. a) Cycling performance b) Cycling performance (left axis) and coulombic efficiency profiles (right axis) of full pouch cells at a 0.5C rate c) charge/discharge curves at a rate of 0.5C of the 2nd cycle d) Change in time of contribution of capacity gained during constant voltage step with respect to the total capacity.

3.4.3. Discussion on the cycling behaviour of other additives

The results obtained in the coin cell experiment of section 3.4.1 were not well repeatable in pouch cells. Recently several studies have been published addressing the complications of translating fundamental research, usually performed in Li half coin cells, to the practical adoption of new ideas in commercially produced pouch cells [8, 33, 38]. The question arises whether the coin cell results can accurately predict the cycling behaviour of the same electrolyte composition in a pouch cell. Three parameters, being cathode loading, electrolyte amount, and Li metal amount, can greatly influence the cycling behaviour of the lithium half-cell [8, 33].

Two variables can be excluded in this reseach and assumed to be constant, leaving only the electrolyte amount as a variable. The cathode loading, or the areal capacity of the cathode, in this research is constant 3.5 mAh/cm^2. The cells used for testing the cycling behaviour were full cells, which means no Li metal was used. Consequently, the only variable parameter in this experiment is the electrolyte amount, specifically the electrolyte-capacity ratio.

The coin cells are in a so-called 'flooded state' with an excess of electrolyte, which might enhance the cycle life of the full coin cell. In a full pouch cell 3 g electrolyte/Ah is used, while in a coin cell the ratio is 8 times higher, with 25 g electrolyte/Ah. For Li metal cells it has been demonstrated that an excess of electrolyte can extend the cycle life, since it takes longer before all electrolyte is reacted in irreversible side reactions [8, 33]. In a full Si/NMC-622 coin cell a SEI is formed, which should prevent irreversible side reactions from happening, but it is also demonstrated that the SEI keeps on expanding during prolonged cycling [48] and, consequently, electrolyte is consumed during the SEI formation [65]. Therefore, it is likely that a flooded state of electrolyte might also enhance the cycle life in full coin cells similarly to Li metal cells, while this behaviour would not be seen in a full pouch cell.

Another aspect that deserves to be discussed is the procedure of manufacture of the batteries, since the procedure of manufacture determines for a large part the functionality of the cell. Full coin cells are likely less well reproducible than pouch cells due to easy misalignment of the anode and the cathode, resulting in a lower capacity than theoretically expected and differences in capacity between cells of equal material. Murray et al. [38] made suggestions to optimize the manufacture of full coin cell, which are: to use anode and cathode disks of equal diameter; to use a single separator of BMF (Polypropylene Blown Micro Fiber), which is thicker and more compressible than a Celgard separator; to construct the cell with a vacuum pen rather than tweezers. With the incorporation of these suggestions, the full coin cells likely predict the performance of new materials in a commercial pouch cell better.

However, the pouch cell manufacture process was not optimized yet at the start of this research. Therefore, no reliable charge/discharge cycle data was obtained in section 3.2 and section 3.3 by the experiments repeated in pouch cells. Thus parts of the experiments cannot be used to draw conclusions on and from previous statements it is obvious that coin cell data needs to be analysed with care. After this realisation, improvements were implemented and, before the start of the experiments in section 3.4, the pouch cell build process was optimized to be more reproducible. Therefore, the differences in cycling behaviour between coin cells and pouch cells observed in this chapter can be discussed here.

Especially EL12 shows different behaviour in a pouch cell compared to a coin cell. It is likely that irreversible reactions take place on the anode side that cause capacity fade. DMAA is reported to preferentially solvate Li-ions compared to DMC and DEC solvents [67], therefore, it can be assumed that DMAA additive is the largest contributor to the SEI layer. The molecular structure of DMAA reveals a large side-group within the expected polymer structure. Just like the methyl-group of PC, the side-group of DMAA may result in an SEI structure with large cavities, which allow for the penetration of the electrolyte and allow for the continuous decomposition of the electrolyte and consumption of the Li-ions, resulting in the observed capacity fade [51]. Molecular dynamics models might provide insights into the expected structure of the SEI in the presence of DMAA.

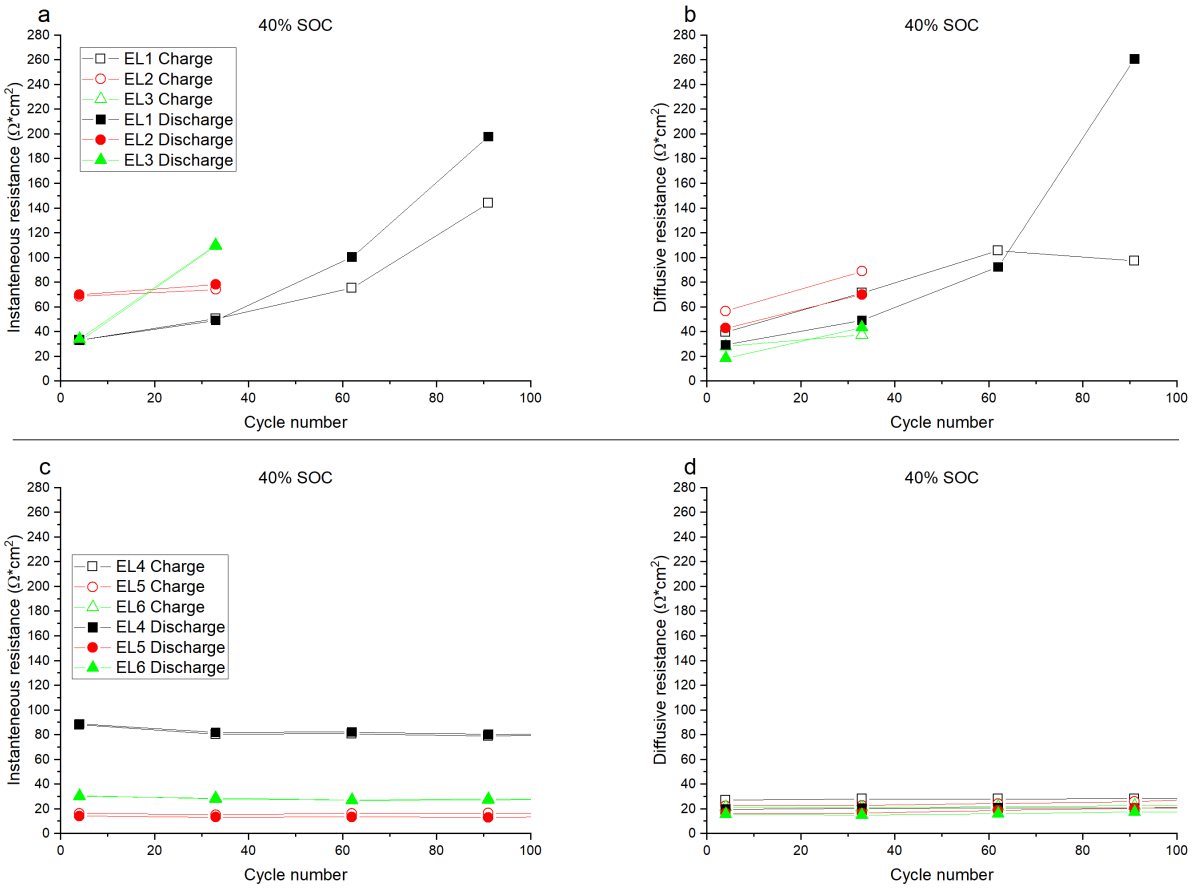

Figure 3.8: Change in Direct Current Internal Resistance in full coin cells at 40% SOC a) for instantaneous processes with electrolyte compositions: 1M $LiPF_6$ in pure DEC, 1M $LiPF_6$ in pure DMC, 1M $LiPF_6$ in pure EMC b) for diffusive processes with electrolyte compositions: 1M $LiPF_6$ in pure DEC, 1M $LiPF_6$ in pure DMC, 1M $LiPF_6$ in pure EMC c) for instantaneous processes with electrolyte compositions: 1M $LiPF_6$ in pure DEC 2 wt% AN 5 wt% FEC 2 wt% VC, 1M $LiPF_6$ in pure DMC 2 wt% AN 5 wt% FEC 2 wt% VC, 1M $LiPF_6$ in pure EMC 2 wt% AN 5 wt% FEC 2 wt% VC d) for diffusive processes with electrolyte compositions: 1M $LiPF_6$ in pure DEC 2 wt% AN 5 wt% FEC 2 wt% VC, 1M $LiPF_6$ in pure DMC 2 wt% AN 5 wt% FEC 2 wt% VC, 1M $LiPF_6$ in pure EMC 2 wt% AN 5 wt% FEC 2 wt% VC.

3.5. Evolution of the Internal Resistance

DCIR experiments were integrated within the cycling protocol, hence, they were performed during the cycling behaviour tests of the cells. On all cells discussed in the sections 3.2 to 3.4 DCIR experiments were performed. The results of these experiments are shown hereafter.

DCIR experiments at 40% SOC were performed on full Si/NMC-622 coin cells with electrolytes EL1, EL2 and EL3 and electrolytes EL4, EL5 and EL6. Measurements were done after every 25 charge/discharge cycles according to DCIR protocol 1. Thus, DCIR has been measured at 20, 40 and 60% SOC and we have found that the results at 20, 40 and 60% SOC are similar. Therefore, we have decided to only incorporate the DCIR at one state of charge in this report, 40% SOC. The change in resistance in the cells as a function of the amount of cycles is shown in Figure 3.8.

Figure 3.8 shows that the diffusive resistance as well as the instantaneous resistance is at least twice as high for the batteries without additives compared to the batteries with additives. Kim et al. [25] found that the resistance of the SEI on a Si anode becomes 5 times smaller when FEC is added to the electrolyte mixture, thus the overall resistance measured by DCIR is also likely to decrease by using FEC and VC additives. Accordingly, the decrease in resistance can likely be attributed to the formation of a more stable, electronically insulating SEI layer, which is likely also thinner since detrimental side reactions are impeded.

Another remarkable feature is that the resistance increases tremendously when roll-over occurs. Roll-

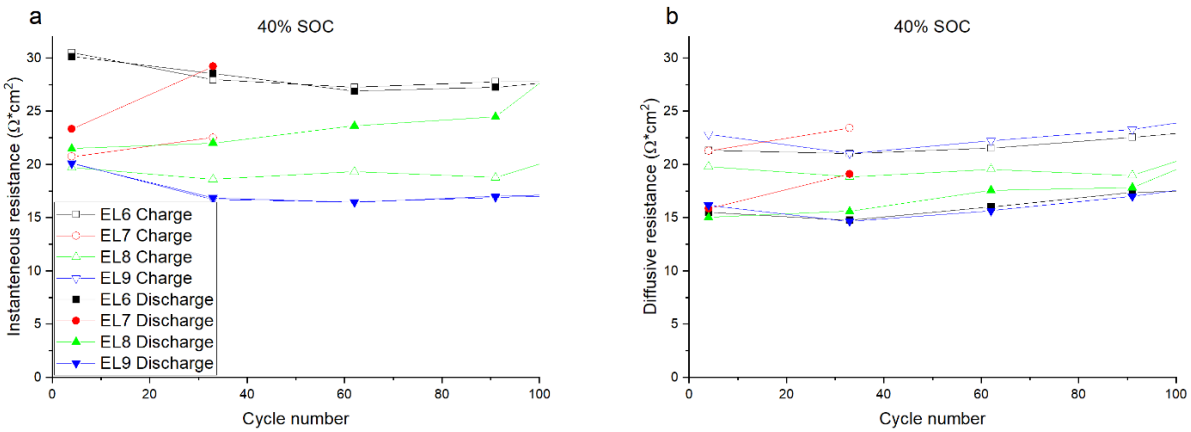

Figure 3.9: Change in Direct Current Internal Resistance in full coin cells at 50% SOC a) for instantaneous processes and b) for diffusive processes with electrolyte compositions: 1M $LiPF_6$ in EC:DEC (1:1 vol%) 2 wt% AN 5 wt% FEC 2 wt% VC, 1M $LiPF_6$ in PC:DEC (1:1 vol%) 2 wt% AN 5 wt% FEC 2 wt% VC, 1M $LiPF_6$ in PC:EC:DEC (1:1:1 vol%) 2 wt% AN 5 wt% FEC 2 wt% VC, 1M $LiPF_6$ in pure DEC 2 wt% AN 5 wt% FEC 2 wt% VC.

over is the process of instant, rapid capacity fade of the battery. We have observed this feature for many experiments and throughout the experiments performed for the purpose of this thesis. Possible explanations of the roll-over could be the consumption of Li, causing degradation of the cathode, for example by transition metal dissolution, or electrolyte consumption or drying up, leading to high viscosity, or consumption of FEC, which is reported earlier to cause sudden capacity fade [14].

DCIR experiments at 40% SOC were also performed in full Si/NMC-622 coin cells containing EL6, EL7, EL8 and EL9 after every 25 charge/discharge cycles according to DCIR protocol 1. The results are shown in Figure 3.9. It can be seen that the instantaneous resistance of EL6 is higher than the instantaneous resistance of EL8 and EL9, which might be attributed to the lower Si utilisation level of EL6 (~1500 mAh/g) compared to EL8 and EL9 (~1800 mAh/g), as shown in Figure 3.5a. Since less Si material is active in this cell, the Ohmic resistance of the cell might be higher. EL8 shows a slightly higher resistance than EL9, which is likely caused by the lower capacity retention of the cell during cycling and thus the likely degradation of the electrode material. Similarly, the quick capacity fade observed for EL7 is likely the cause of the increase in resistance.

Furthermore, it is noticeable that the diffusive resistance during charge is always higher than during discharge. This is likely caused by the solid state diffusion of Li-ions within the electrodes. A Li-ion diffusion coefficient (D_{Li^+}) of $2.3 \cdot 10^{-13}$ and $8.2 \cdot 10^{-13}$, correlating to the two-step reaction mechanism, for solid state diffusion of Li-ions in the anode upon charge was found in section 3.1. The D_{Li^+} in the NMC cathode is found to be 10 times higher during discharge, as a value of $7.9 \cdot 10^{-12}$ was found as shown in Figures A.2 and A.3 and Table A.2. The significantly higher D_{Li^+} in the NMC cathode during discharge implies a lower diffusive resistance. Another explanation might be a different driving force for Li-ion diffusion during charge compared to discharge. Upon charge of the battery an extra force, in the form of an applied potential, needs to be applied for Li-ion diffusion to take place, however, discharge is an autonomous process, for which no extra force needs to applied. Thus, the higher diffusive resistance upon charge might also be caused by a thermodynamic effect. This same feature is also clearly visible in Figure 3.8, Figure 3.10 and Figure 3.11.

Lastly, DCIR experiments at 50% SOC were performed in full Si/NMC-622 coin cells containing EL10, EL11, EL12 and EL13 after every 25 charge/discharge cycles according to DCIR protocol 2 to determine the change in resistance in the battery as a function of the amount of cycles and the results are shown in Figure 3.10. The same experiment was repeated full Si/NMC-622 pouch cells and these results are shown in Figure 3.11. The diffusive resistance for both the coin cell test and the pouch cell test display the same stable behaviour over time, with as pointed out before a larger resistance during charge than during discharge. The instantaneous resistance shows more interesting behaviour, namely a sudden drop in the resistance after the first 25 cycles, which can be observed for all cells in Figure 3.10, for EL11 in Figure 3.11 and for EL6 and EL9 in Figure 3.9.

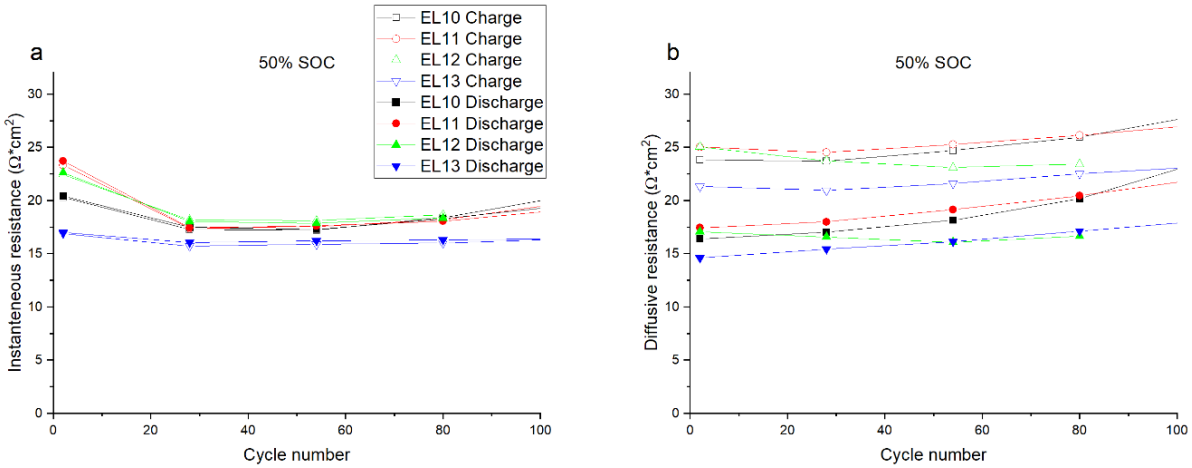

Figure 3.10: Change in Direct Current Internal Resistance in full coin cells at 50% SOC a) for instantaneous processes and b) for diffusive processes with electrolyte compositions: 1M $LiPF_6$ in EC:DEC (1:1 vol%) 2 wt% AN 5 wt% FEC 1 wt% VC, 1M $LiPF_6$ in EC:DEC (1:1 vol%) 2 wt% AN 5 wt% FEC 1 wt% VC 1 wt% DAPC, 1M $LiPF_6$ in EC:DEC (1:1 vol%) 2 wt% AN 5 wt% FEC 1 wt% VC 1 wt% DMAA, 1M $LiPF_6$ in EC:DEC (1:1 vol%) 2 wt% AN 5 wt% FEC 1 wt% VC 1 wt% TEOSCN.

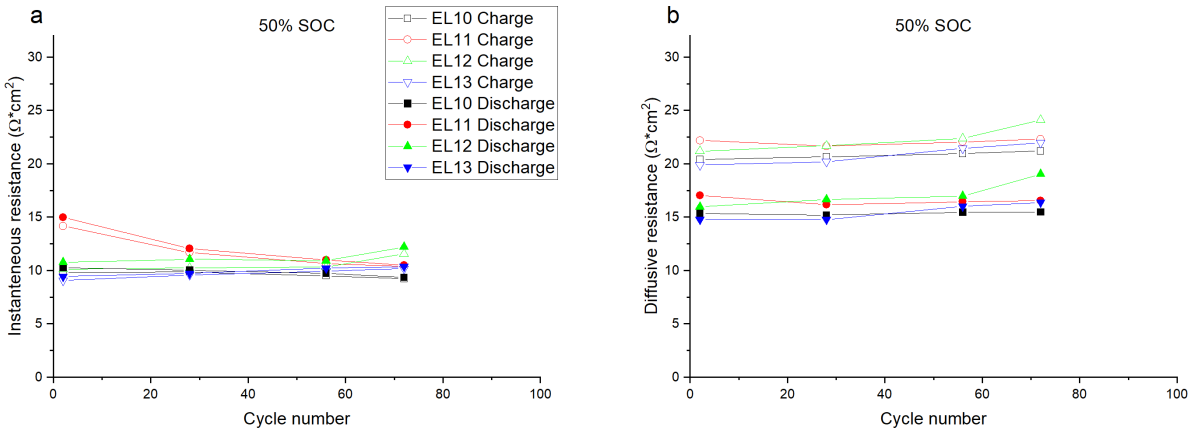

Figure 3.11: Change in Direct Current Internal Resistance in full pouch cells at 50% SOC a) for instantaneous processes and b) for diffusive processes with electrolyte compositions: 1M $LiPF_6$ in EC:DEC (1:1 vol%) 2 wt% AN 5 wt% FEC 1 wt% VC, 1M $LiPF_6$ in EC:DEC (1:1 vol%) 2 wt% AN 5 wt% FEC 1 wt% VC 1 wt% DAPC, 1M $LiPF_6$ in EC:DEC (1:1 vol%) 2 wt% AN 5 wt% FEC 1 wt% VC 1 wt% DMAA, 1M $LiPF_6$ in EC:DEC (1:1 vol%) 2 wt% AN 5 wt% FEC 1 wt% VC 1 wt% TEOSCN.

The decrease in instantaneous resistance might be caused by a better wetting of the active electrode material with electrode after a number of cycles, an increase in the active surface area of the Si particles or a change in the SEI composition. It might have been the case that for some of the cells, the electrolyte was not well dispersed yet over the electrode's surface during the initial cycles. During cycling, the electrolyte disperses more evenly over the electrode's surface and therefore, more Si is activated and the resistance occurring from the active surface area of the electrode decreases.

Another mechanism that results in an increase in the active surface area is cracking of the Si anode. It has been observed that the resistance over the cell changes with SOC during lithiation and delithiation in a W-shaped fashion, where the highest electronic resistances are found at the end and beginning of lithiation and delithiation (around 0 and 100% SOC) and the lowest electronic resistances are found between 40 and 80% [41]. As the biggest cracks are observed between 40 and 80% SOC, it can be assumed that the increase in cracks can be related to an increase in active surface area and consequently results in a decrease in resistance. It is a possibility that the cracks formed during cycling are not recovered fully and thus it is likely that the formation of cracks results in an increase in active surface area as the Si anode particles are divided into smaller particles.

Lastly, the composition of the SEI layer may have changed after 25 cycles, consequently the type of species may have changed, the distribution of species might be more homogeneous and the size of the pores might have changed. It is observed that mostly organic compounds further degrade into smaller, inorganic compounds, which typically have a higher ionic conductivity [48, 60]. Besides, the further degradation of the SEI compounds and the transformation of the SEI layer upon cycling, might results in a more homogeneous layer and a different distribution of the pores and pore sizes. A logical conclusion can be made that an increase in porosity or pore size, enhances the Li-ion diffusivity in the SEI layer [17]. Furthermore one can assume that a more homogeneous layer also benefits the pathways for Li-ion diffusion towards the Si anode.

Additionally, overall the areal instantaneous resistance in the pouch cells is approximately 5 - 15 $\Omega \cdot cm^2$ lower than in the coin cells. This is likely related to the differences in cell assembly between the coin cell and the pouch cell. The difference might be explained by a higher contact resistance and higher resistance for Li-ion transport through the electrolyte for the coin cells. The coin cell layers are held together and connected to the case on one side by a spring. As the spring cannot be perfectly centred upon assembly, a pressure distribution over the electrodes surface is likely, which results in higher resistance compared to the pouch cell, where the contacts are directly connected to the electrodes. Besides, a coin cell contains two layers of separator, of which one thick glass fibre layer, while a pouch cell only contains one layer of the thinner Celgard 2500 separator. Therefore, the diffusion of Li-ions between the anode and the cathode is subjected to a higher resistance.

3.5.1. Discussion on Direct Current Internal Resistance results

DCIR is used quite often in industry as the technique is relatively simple, quick, easy and efficient. However, DCIR does not appear in the works cited in this report, so it can be assumed that in scientific publications this technique is not encountered often. In stead, often a combination of only CV and EIS complementary to long term charge/discharge tests is used to investigate the electrochemical behaviour of a battery. This might be because the technique might not be well-known in the scientific community or the fact that it is not possible to differentiate between different processes that cause a change in resistance, but the results of DCIR are quick and easy to obtain and the interpretation of the results is straightforward, unlike EIS, which is prone to the bias of the researcher. In this research we implemented DCIR to provide a first indication on the change in internal resistance of the battery as the result of different electrolyte compositions.

Unfortunately, due to the protocols used to perform the DCIR measurements, the results of the DCIR measurement are found to be easily misinterpreted. We have found that the SOC at which DCIR is measured changes as a result of the protocols used. When DCIR protocol 1 was used, in which the cell was charged for 2h at a current rate of 0.2C, the cell should be at 40% SOC when the DCIR experiment is performed. However, the battery tester calculates the current needed to obtain a constant current rate of 0.2C based on the capacity of the cell during formation, so when capacity fade happens, DCIR is not measured at a SOC of 40%, but at a higher SOC. For example, at 80% capacity retention, the DCIR measured after 2h, is measured at a SOC of 50%.

Contrarily to DCIR protocol 1, where the SOC at which is measured increases over time, we found that for DCIR protocol 2, the SOC at which is measured decreases over time. In section 3.4, the protocol for the DCIR measurement was changed to DCIR protocol 2, where we charge to 3.6V and add a constant voltage step at this potential. For most batteries 3.6V represents about 50% SOC, if you look at the charge/discharge curves of the battery during the initial cycles. However, upon prolonged cycling, the capacity decreases and the over-potential required to charge the battery increases. Thus, the charge/ discharge curves over a set of cycles, see Figure A.4 in the appendix, show that after a significant level of capacity fade, the cell will be at a lower SOC at 3.6V.

It is assumed here that the instantaneous resistance measured by DCIR is not largely dependent on the SOC, because this resistance is determined largely by the internal resistance of the battery driven by Ohmic processes, but that the diffusive resistance is dependent on the SOC of the battery. The diffusive resistance is determined by the relaxation of the potential after a current pulse. The shape of the characteristic relaxation curve is likely dependent on the solid state diffusion of Li driven by the concentration gradient of Li in the Si particle. The concentration of Li present in the Si particle is dependent on the Si utilisation level of the battery and on the SOC of the battery. Note that the batteries show significant variations in Si utilization levels varying between $\sim$1000 mAh/g and $\sim$1900 mAh/g.

The conductivity of Si varies depending on the concentration of Li alloyed to Si. At a higher Si utilization level of the battery, the concentration of Li inside the Si is higher for the same SOC, so the conductivity of Si is different [42]. When capacity fade happens and the actual SOC at which DCIR is measured is higher than the assumed SOC, Si is in a higher lithiated state, so the concentration of Li in Si is higher and thus the conductivity will alter. The diffusion ability of Li and the conductivity of Si are likely to change depending on the Si utilisation level and the SOC. Consequently, the shape of the relaxation curve and, thus, the diffusion resistance measured by DCIR will change. Therefore, it is not possible to distinguish between the effects of the diffusion through the SEI and the diffusion in the Si.

As for DCIR protocol 1, the SOC at which is measured increases over time, and for DCIR protocol 2, the SOC at which is measured decreases over time, the diffusive resistance is expected change according to the SOC of the battery. Si itself has a poor electrical conductivity of less than 10^{-5} S cm^{-1} [1], while lithium has a much higher conductivity. Thus, upon lithiation of the Si anode, the electrical conductivity of the material is expected to increase. Pollak et al. [42] found that the conductivity of the amorphous Si layer increases significantly upon lithiation with a peak around 0.12 V vs Li/Li$^+$. The highest lithiated phase was found to be less conductive than the phase, likely corresponding to a-Li$_x$Si phase, which is formed around 0.12 V vs Li/Li$^+$. Thus, depending on the SOC of the battery, the conductivity of the Si anode varies significantly. As conductivity is the reverse of resistivity ($\sigma = 1/\rho$), upon lithiation the resistivity of the Si anode changes. Besides, for a cell with a higher Si utilisation level, and thus a higher concentration of Li in the Si, the resistance is also expected to be different from a cell with a lower Si utilization level.

3.6. Evolution of the Solid Electrolyte Interphase Resistance in symmetric coin cells

EIS is performed on symmetrical coin cells after charging the cell to 0V, both after assembly of the battery and after 25 cycles, containing solely pure Si anodes with four different electrolyte compositions: EL10, EL11, EL12 and EL13. Since, other properties of the additive and the SEI formed by its decomposition products will definitely also have an influence on the cycling behaviour of the battery, as they are listed in section 1.1.5, EIS is used besides solely long term charge/discharge experiments and DCIR. With the use of EIS, a distinction can be made between the contribution of different processes in a cell with respect to the resistance in the cell, thus the evolution of the SEI resistance can be measured and the abilities of the additives to form a good passivating layer on the electrode can be analysed. The obtained EIS spectra are analysed with the use of both DRT analysis and analysis with the use of an EC. DRT analysis was performed on the impedance data, as shown in Figure 3.12, and impedance spectra are displayed in Figure 3.15 in Nyquist plots.

An equivalent circuit is proposed as presented in Figure 3.13. The choice for this specific equivalent circuit stems from an article by Pan et al. [41], who related DRT analysis to impedance spectra represented in Nyquist plots. From calculated activation energies and time constants derived from the

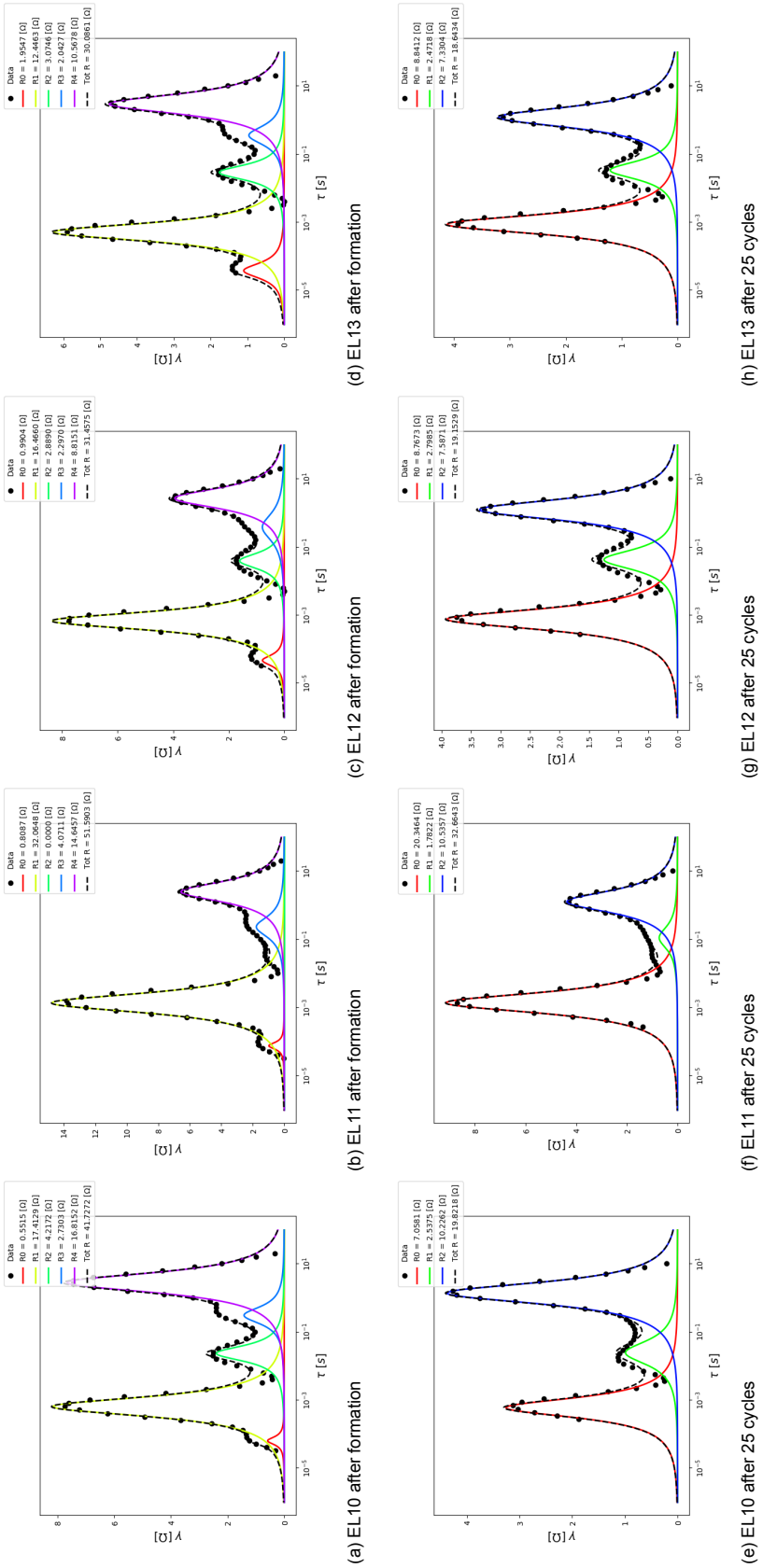

(a) EL10 after formation (b) EL11 after formation (c) EL12 after formation (d) EL13 after formation

(e) EL10 after 25 cycles (f) EL11 after 25 cycles (g) EL12 after 25 cycles (h) EL13 after 25 cycles

Figure 3.12: DRT analysis obtained by applying a Tikhonov Regularization procedure of impedance data of symmetrical coin cells of a) EL10 after formation, b) EL11 after formation, c) EL12 after formation, d) EL13 after formation, e) EL10 after 25 cycles, f) EL11 after 25 cycles, g) EL12 after 25 cycles and h) EL13 after 25 cycles.

DRT data, predominant polarization losses were obtained. These losses were found to be contact impedance, SEI layer related impedance and charge transfer impedance.

From the DRT analysis that was performed on the impedance data obtained from symmetrical coin cells, four time constants can be distinguished, which can be related to the predominant polarization losses. From the plots in Figure 3.12, time constants for the electrochemical processes are found at $\tau \approx 10^{-4.5}, 10^{-3.5}, 10^{-1.5}$ and $10^{0.5}$s. These time constants can be related to characteristic polarization losses in the battery as described by Pan et al. [41]. Respectively, the processes relate to contact impedance or electrical and magnetic effects, SEI layer impedance, charge transfer impedance and relaxation and diffusion as described in an article by Danzer [11] and shown in Figure 3.14. Therefore, the equivalent circuit (Figure 3.13) can be explained as follows.

R_s is the solution resistance between the electrodes [28], represented by the uncompensated Ohmic loss of the battery [41]. The resistance R_s originates from the current collector, the electrolyte and the separator and together can be classified as bulk resistance [10]. R_1 is classified as contact resistance originating from the contact loss of the Si electrode [41]. R_2 is classified as the SEI resistance and, as the name describes, this is the resistance arising from the resistance to alternating current by the SEI layer. R_3 is classified as the charge transfer resistance, which is connected parallel to constant phase element Q_3, originating from the double layer effect on the interphase between the SEI layer and the Si particles [11, 28, 41].

Q_2 and Q_3 are CPE's, which originate from the non-ideal capacitor behaviour, thus they display a frequency dispersion and are characterised by depressed semi-circles in the Nyquist plots [28]. The last element is W, the Warburg element. The impedance of the Warburg element originates from the mass transfer of the Li particles inside the Si deposition layer [10]. A semi-infinite Warburg impedance element shows a tail with a 45° incline, but the Nyquist plots in Figure 3.15 show tails with steeper inclines. Therefore, a finite-length Warburg impedance is assumed as a diffusion model as proposed by Levi and Aurbach [31]. This element, characterised by the addition of a capacitor in series with the Warburg element, can be explained by the finite thickness of the Si deposition layer and thus the finite diffusion of Li particles until the particles hit the Cu current collector. The accumulated lithium at the current collector surface will cause a capacitor type behaviour [31].

A fit with the equivalent circuit of Figure 3.13 was performed on the impedance spectra of Figure 3.15 with $X/|Z|$ as shown in Table 3.2. The values for the circuit elements obtained by the EC-fit are compared with the values obtained with DRT in Tables A.3, A.4, A.5 and A.6. The SEI resistance (R_2) after formation of the battery is 18.18 Ω, 31.11 Ω, 16.10 Ω and 13.84 Ω for EL10, EL11, EL12 and EL13 respectively. After 25 cycles the SEI resistance is 8.48 Ω, 20.49 Ω, 8.76 Ω and 7.54 Ω for EL10, EL11, EL12 and EL13 respectively. R_2 of EL11 is higher compared to EL10, EL12 and EL13, which is likely caused by a high amount of active lithium consumption during the first cycles for the formation of the SEI layer, which is supported by the small capacity fade during the first cycles observed in the full coin cell long term charge/discharge tests in section 3.4.1. Additionally, a decrease in R_2 in observed after 25 cycles, unlike the expected increase in R_2 due to an expected increase in SEI thickness [48, 49].

The observed R_2 decrease might be caused by a change in SEI composition, homogenisation of the SEI layer or a higher porosity after 25 cycles. Stetson et al. [48] observed a reduced superficial SEI electronic resistivity after 10 cycles on a crystalline Si wafer with the use of SSRM. As more electronically insulating organic and/or polymeric compounds decompose into more conductive inorganic compounds, the reduced resistivity was related firstly to a change in chemical composition at the interphase. For example, a lithium ethylene dicarbonate (LEDC)-rich SEI, typically formed in the presence of EC in the electrolyte, is observed to further decompose into LiF and Li_2CO_3 [60]. Wang et al. [53] reported that a change in chemical composition of the SEI has an effect on the ionic conductivity, for example, a mixture of LiF and Li_2CO_3 is believed to enhance the ionic conductivity of the SEI. Secondly, they related the reduced resistivity to a better mixed SEI phase, resulting from a reduced segregation of the SEI component by the continuous volume changes.

Furthermore, it is reported that a higher porosity of the SEI layer can enhance the Li-ion diffusion through the SEI [17]. Guan et al. [17] performed a simulation study on the micro-structural morphology evolution of the SEI on a graphite anode and showed that the Li-ion diffusion coefficient in the SEI increases with an increased porosity of the SEI layer. A change in porosity was attributed to a morphological change

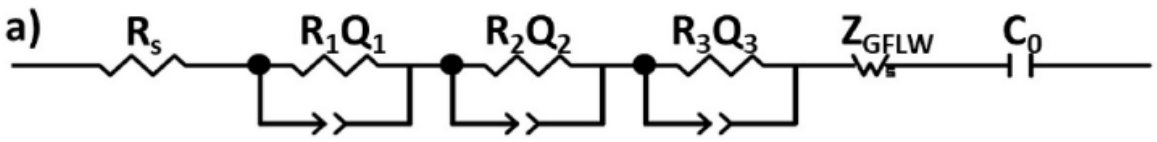

Figure 3.13: Electrical equivalent circuit for fitting of the symmetrical coin cell impedance spectra [41].

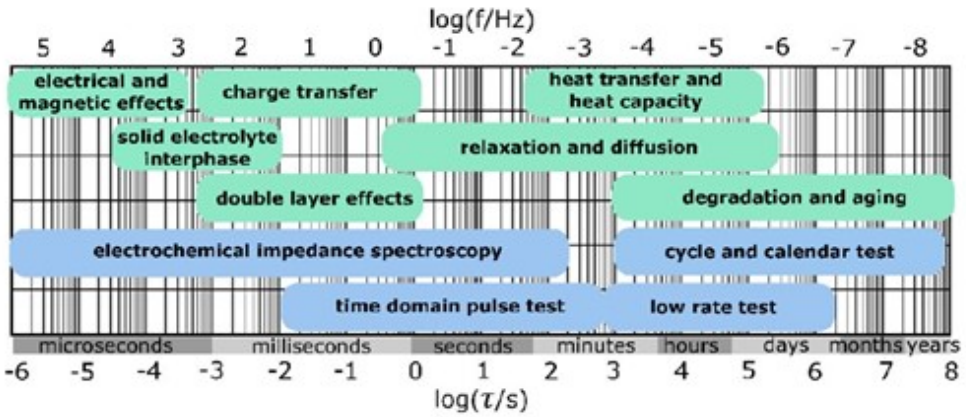

Figure 3.14: Ranges of characteristic time constants for in green dynamic, frequency dependent processes of an electrochemical system and in blue battery test methods [11].

Table 3.2: Error ($X/|Z|$) found for the fits of the EIS data with the EC for EL10, EL11, EL12, EL13 and their duplicates. The EIS measurement failed for the duplicates of EL11 and EL12 after the formation cycles.

	EL10	EL10 duplicate	EL11	EL11 duplicate	EL12	EL12 duplicate	EL13	EL13 duplicate
Formation	3.814E-3	7.352E-3	2.528E-3		7.319E-3		8.511E-3	8.743E-3
25 cycles	5.329E-3	3.701E-3	0.7785E-3	1.509E-3	3.552E-3	0.892E-3	6.218E-3	4.379E-3

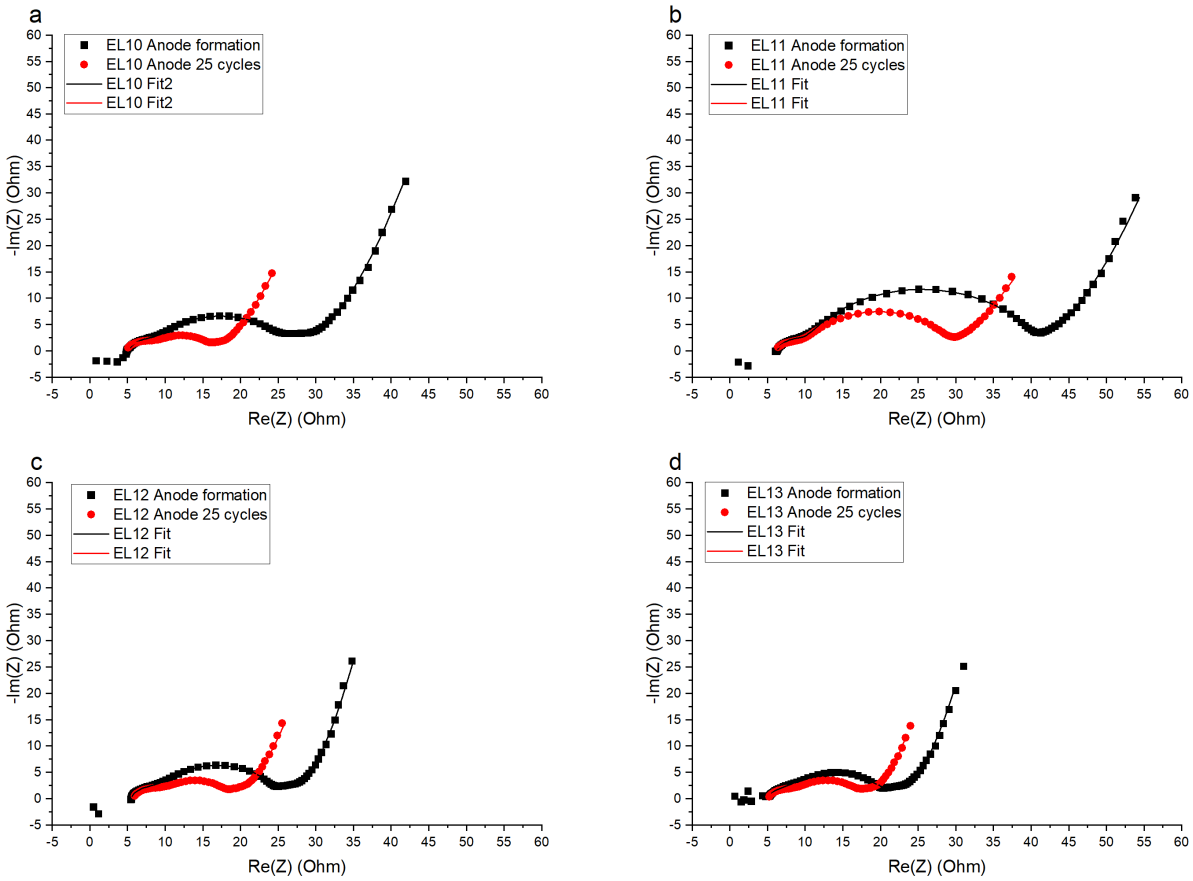

Figure 3.15: Electrochemical Impedance spectra displayed in Nyquist plots of symmetrical coin cells with pure Si anodes and electrolyte compositions a) EL10 b) EL11 c) EL12 and d) EL13.

in the composition of the SEI layer. Therefore, it is also possible that a morphological change, perhaps a homogenisation of the SEI layer, caused an increased porosity and thus a lower resistivity. Thus, it is likely that the chemical composition and distribution of compounds changed during 25 cycles, resulting in a lower R_2.

3.6.1. Discussion on Electrochemical Impedance Spectroscopy results

Electrochemical Impedance Spectra need to be analysed with care as they are prone to misinterpretations. The results might be adjusted, consciously or unconsciously, by the interpretation of a biased researcher. In the case of analysis with the use of an EC, it is very important that a EC which has a physical meaning is chosen. Therefore, it is very important that the researcher constructs a physically meaningful model of the system that is studied and is able to explain the components of the EC. The physical model used in this research is constructed with the existing knowledge on the battery system and the electrolyte/SEI/electrode interphases.

The drop in resistance was assumed to be related to a change in SEI composition, homogenisation of the SEI layer or a higher porosity, which can be validated by analysing the SEI layer after formation and after 25 cycles. SEM and cross-section SEM will show how the morphology changes and can be combined with BET analysis to measure the specific surface area, average pore size, pore volume and the porosity of the SEI layer. Thus the change in porosity and pore size can be correlated with the change in morphology and also with the change in SEI resistance. Cross-section SEM, possibly combined with energy-dispersive X-ray spectroscopy (EDX), will also show the homogeneity of the SEI layer. Lasty, XPS and NMR analysis show which species are present in the SEI and, thus, can be used to analyse the change in SEI composition.

A drop in the instantaneous resistance was observed after 25 cycles for full coin cells with EL10, EL11, EL12 and EL13 measured by DCIR, which might be correlated to the drop in resistance observed with EIS. We can assume that the resistance measured by DCIR is largely impacted by a change in SEI layer composition during cycling, as R_1, R_3 and Z_{GFLW} are quite stable over 25 cycles compared to R_2. After 25 cycles the instantaneous resistance measured by DCIR stabilized. Therefore, this stabilisation of the instantaneous resistance measured by DCIR, if correlated to a change in SEI resistance measured by EIS, might indicate a stabilisation of the SEI layer composition after 25 cycles. In order to confirm this statement, impedance measurements should also be performed after 50, 75 and 100 cycles.

Nevertheless, the assembly of the symmetrical coin cells may have caused noise in the obtained data. The pouch cells that were assembled for the production of the symmetrical coin cells, were assembled with EL9, so no DAPC, DMAA or TEOSCN was added to the electrolytes yet. During formation of the pouch cells a SEI was formed from the decomposition products of EL9. The electrodes were washed with DMC to remove the SEI layer, before assembly of the symmetrical coin cells, but it is very likely that a residue of the SEI layer still remained on the electrode surface. Consequently, the symmetrical coin cells may have had a SEI layer consisting of the decomposition products of EL9, combined with the decomposition products of EL10, EL11, EL12 and EL13 . Note here that the only difference between EL9 and EL10 is 1 wt% VC, so it can be assumed that no effect on the formation of the SEI layer is expected in this cell.

Another factor is the SOC at which the EIS measurement is performed. Pan et al. [41] show the dependence of the SEI resistance and the charge transfer resistance on the SOC of the battery. They have shown that the SEI resistance can be up to 2 orders of magnitude higher at the beginning and end of lithiation and delithiation compared to approximately 50% SOC. Therefore, it is important to measure the EIS always at the same SOC and in comparing results from one research to another to carefully look at the conditions under which the EIS is measured.

In this research, the battery was charged or discharged to 0V with an additional constant voltage step at 0V until the current was below 0.01C, likewise to how the desired SOC in DCIR protocol 2 was obtained. In section 3.5.1 it was discussed that the desired SOC is not always the actual SOC at which is measured depending on the capacity fade of the cell. However, no significant capacity fade was observed during cycling of the symmetric coin cells, as can be seen in Figure A.5. Therefore, the SOC at which was measured after formation of the cell and after 25 cycles can be assumed to be the same.

The EC chosen in Figure 3.13 is controversial to EC's often deployed in literature on LIBs with a Si

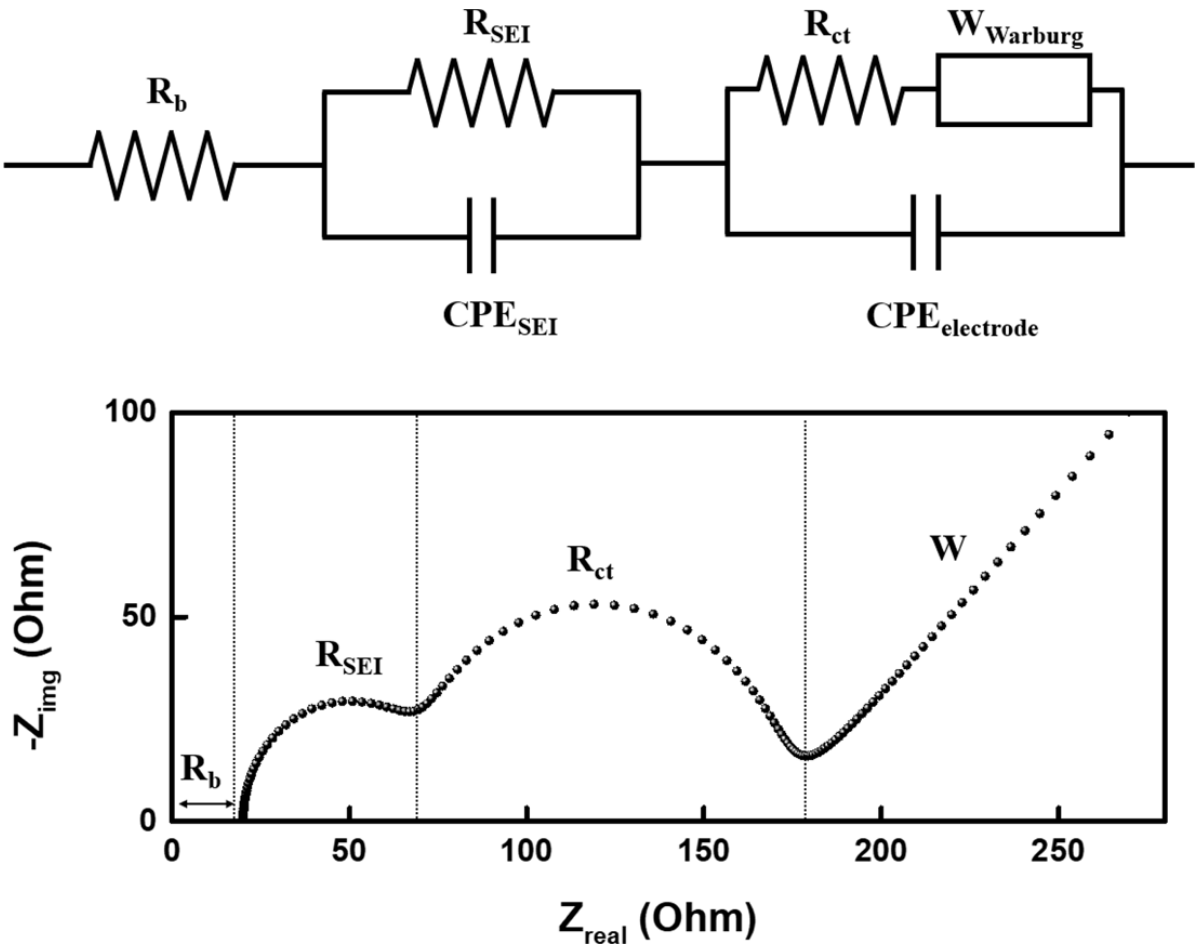

Figure 3.16: Modelled Nyquist plot and corresponding electrochemical equivalent circuit of a LIB system. Reprinted from [10].

anode. In many studies an EC like in Figure 3.16 is used, correlating the first (semi)circle in the Nyquist plot to the SEI resistance and the second (semi)circle to the charge transfer resistance [10, 25, 56]. Thus, R_1 in this research would in the case of this EC correlate with R_{SEI} and R_2 with R_{CT}, which would give an entirely different interpretation of the results. Nevertheless, Choi et al. [10] and Wang et al. [56] do stress that the EC representing a LIB electrochemical system and corresponding EIS spectra vary depending on electrode characteristics, cell type, storage and cycling conditions.

Thus, since the DRT results correspond mostly with the EC of Figure 3.13, in this report that EC is chosen. Analysis with DRT is useful, because it is a model-free approach, it only requires the analysis of peaks. A peak corresponds to a single polarization process, while frequency-dependent electrode processes often overlap in a Nyquist plot [11]. This method revealed the presence of another process at a high frequency, that is overlooked in the EC of Figure 3.16.

4

Conclusions

The aim of this research project was to investigate what effect the electrolyte composition has on the cycle life of a LIB with pure Si anode. This subject was investigated by performing long-term charge/discharge tests, DCIR, CV and EIS tests on batteries with different electrolyte compositions. Firstly, the effect of the addition of frequently used additives, FEC and VC, on the cycle life was experimentally determined, secondly the effect of the addition of cosolvents, PC and EC, and lastly the effect of other additives, DAPC, DMAA and TEOSCN. It can be concluded that an altered electrolyte composition does have an effect on the cycle life, supported by changes in initial specific capacity, capacity retention and resistance in the battery.

It was observed that the capacity retention improved by more than 100 cycles when the additives FEC and VC were added to the electrolyte mixture of $LiPF_6$ dissolved in a pure linear carbonate solvent. The improved capacity retention was attributed to a more favourable SEI that allowed for less irreversible capacity losses. Furthermore, it was observed that the addition of additives significantly lowered the resistance within the battery, which eases the reversible Li-ion diffusion between the anode and the cathode. The addition of cosolvents has shown to improve the Si utilisation level from $\sim$ 1500 mAh/g to $\sim$ 1700 mAh/g. This improvement was attributed to the preferential solvation of Li-ions with EC and PC, which allowed for easier diffusion of the Li-ions between the anode and the cathode. However, the capacity retention did not improve from the addition of the cosolvents. Thus the cycle life might not directly be improved by the addition of PC and EC to the electrolyte composition.

Lastly, it was observed that DAPC improved the capacity retention for more than 100 cycles from 67.7% to 72.2% in a full NMC-622/Si coin cell and from 84.2% to 90.8% in a full pouch cell compared to EL10. The improved capacity retention is attributed to the expected formation of a polymer-rich SEI with good ionic transport properties. A remarkable feature of the DAPC-based electrolyte is the high SEI resistance during the initial cycles, likely caused by a high amount of active lithium consumption during the first cycles for the formation of the SEI layer, and the drop in resistance after 25 cycles, likely caused by a change in SEI composition. Thus, in order to form a stable and robust SEI, the SEI needs to be formed from preferable decomposition products, that mitigate the anode's swelling, prevent penetration of electrons and allow for diffusion of Li-ions, very quickly during the first cycles, which results in some loss of active lithium.

In further research is it recommended to systematically built on the subject of the study. The processes in the battery are complex and not easily understood, therefore the amount of variables per test need to be minimized. Before the start of experimental testing, it is recommended to model the interactions of the electrolyte components with each other. This will give insights in the contribution of the electrolyte components to the conductivity, which is found to be an important factor in the initial specific capacity of the battery. Moreover, it is suggested to model the decomposition of the electrolyte to gain more understanding in the SEI composition.

The modelled SEI composition needs to be confirmed with experiments. Techniques like XPS and NMR can be enforced to experimentally determine the composition of the SEI layer. Finally, the effect of the investigated SEI composition on the cycling performance of the battery needs to be experimentally determined. During these experiments, the researcher must take care of the reproducibility and reliability of the results. It is therefore recommended to perform these tests in full pouch cells rather than (half or symmetric) coin cells, so that the results are representative for LIB produced by battery manufacturers. This is important for the society to take over the promising results obtained in the research community, so that society implements these ideas in its products and green energy driven products are promoted.

A

Additional figures

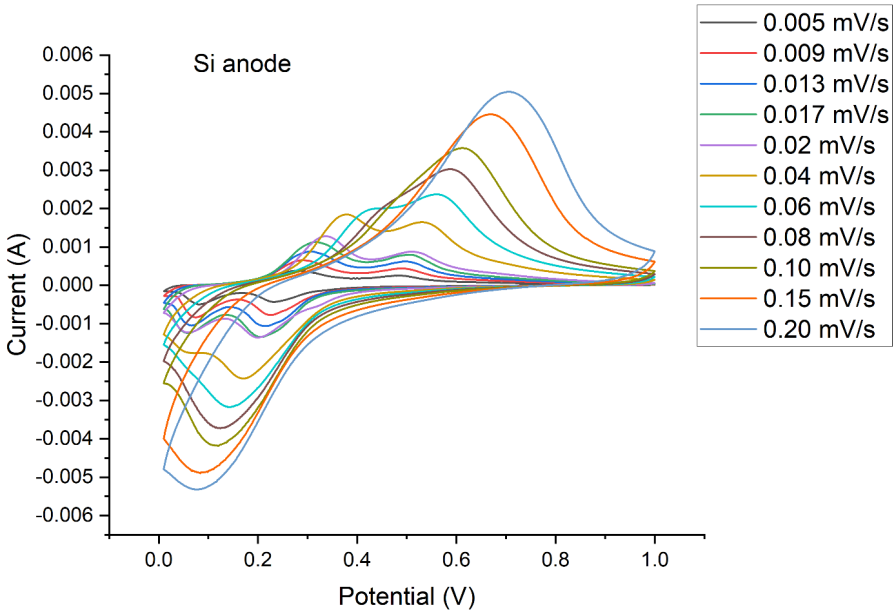

Figure A.1: Cyclic Voltammogram of Si anode half-cell at scan rates ranging from 0.005 mV/s till 0.20 mV/s.

Table A.1: Calculation of the intercept with the y-axis and the slope of the peak current vs square root of the scan rate for the Si anode sample.

		Value	Standard Error	t-Value	Prob>|t|
anodic peak 1	Intercept	-2.57764E-4	6.00439E-5	-4.29292	0.01272
	Slope	0.28468	0.01442	19.73907	3.88553E-5
anodic peak 2	Intercept	-3.74903E-4	1.04852E-4	-3.57553	0.02326
	Slope	0.22297	0.02518	8.8533	8.98807E-4
cathodic peak 1	Intercept	-7.38128E-5	1.40886E-4	-0.52392	0.62802
	Slope	-0.20342	0.03384	-6.0113	0.00386
cathodic peak 2	Intercept	4.73521E-4	9.23214E-5	5.12905	0.00684
	Slope	-0.38253	0.02217	-17.25056	6.6263E-5

Table A.2: Calculation of the intercept with the y-axis and the slope of the peak current vs square root of the scan rate for the NMC-cathode sample.

		Value	Standard Error	t-Value	Prob>|t|
anodic peak	Intercept	-2.33334E-4	1.9480E-4	-1.19777	0.28468
	Slope	0.32183	0.02022	15.91936	1.78028E-5
	D_{Li+}	1.98E-10			
cathodic peak	Intercept	-2.22162E-4	1.09346E-4	-2.03174	0.09789
	Slope	-0.06438	0.01135	-5.67383	0.00237
	D_{Li+}	7.90E-12			

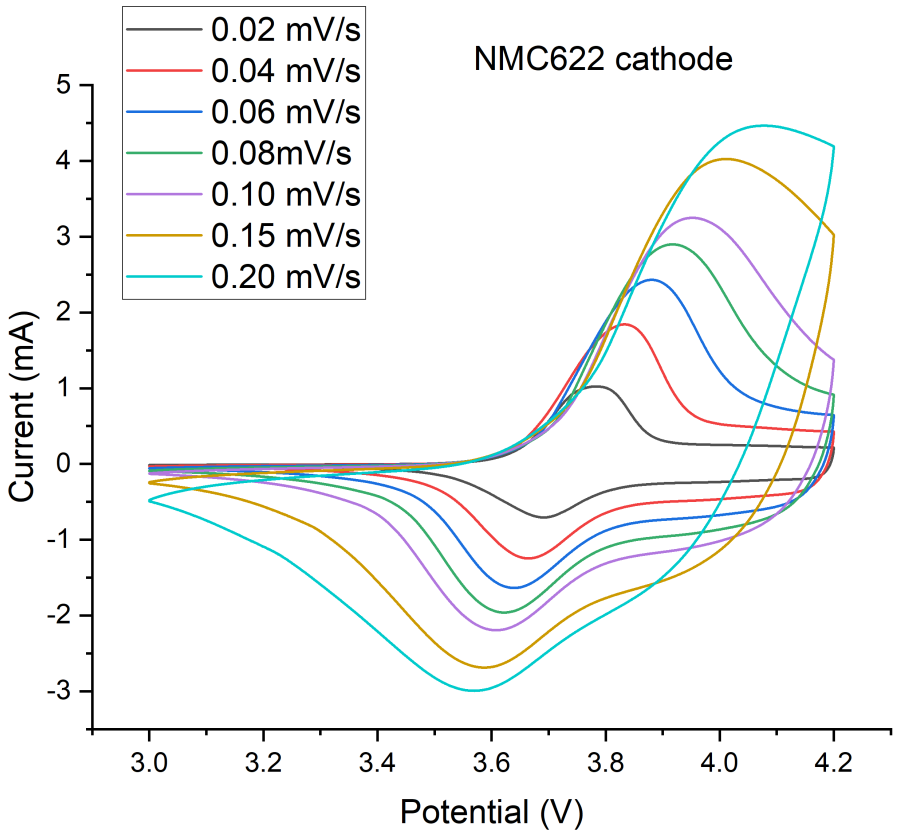

Figure A.2: Cyclic Voltammogram of NMC-622 cathode half cell at various scan rates.

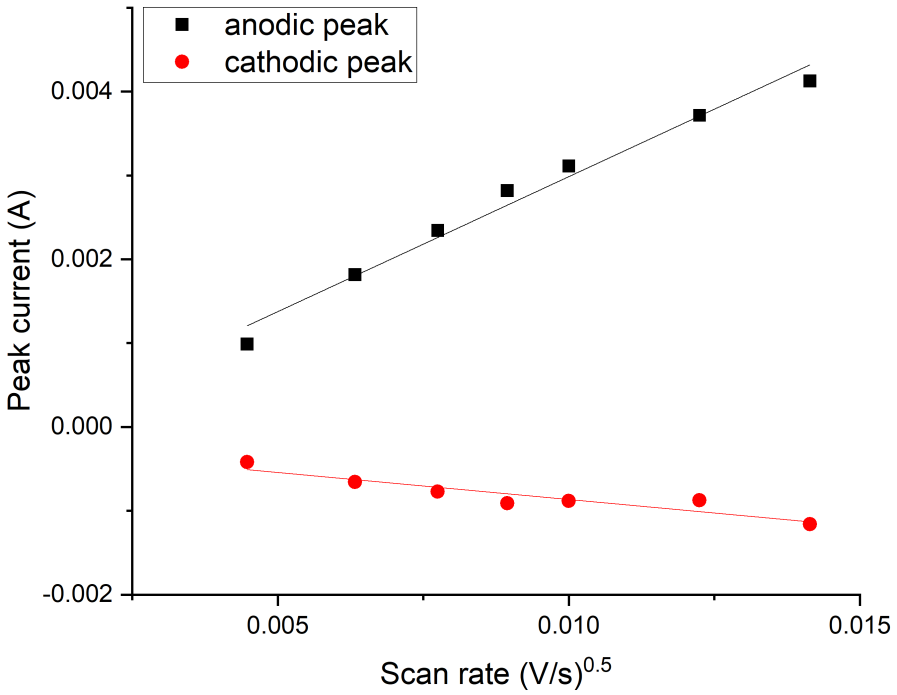

Figure A.3: Peak currents (one anodic peak and one cathodic peak) of the NMC-622 cathode half-cell cyclic voltammogram versus the square root of the scan rate with a linear fit (with equation $y = ax + b$).

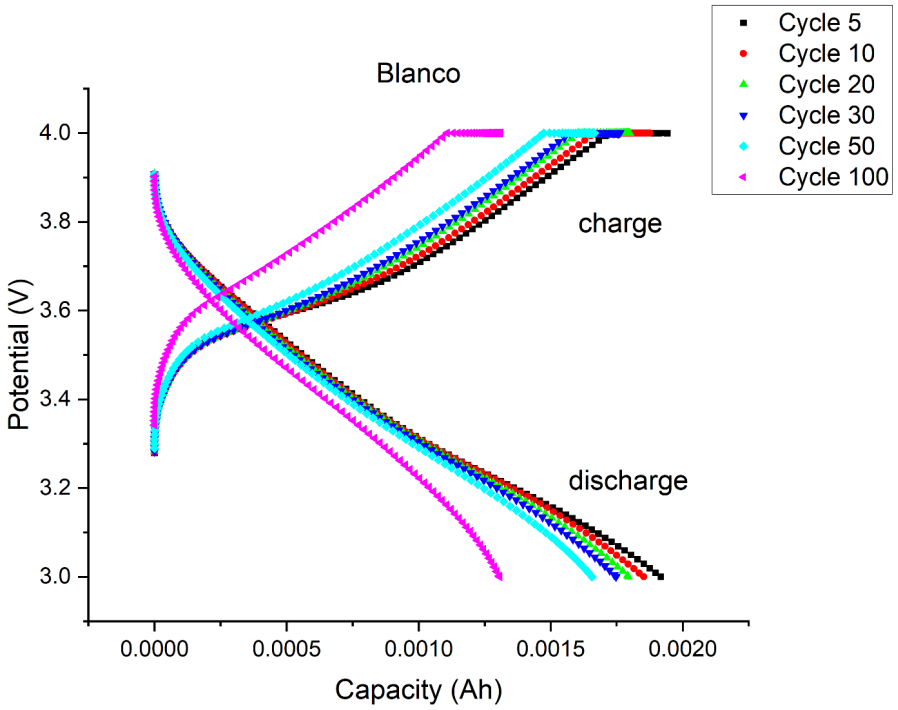

Figure A.4: Charge/discharge curves over the cycle life of a full coin cell with electrolyte composition 1M LiPF6 in EC:DEC (1:1 vol%) 2 wt% AN 5 wt% FEC 1 wt% VC cycled at a constant current rate of 0.5C.

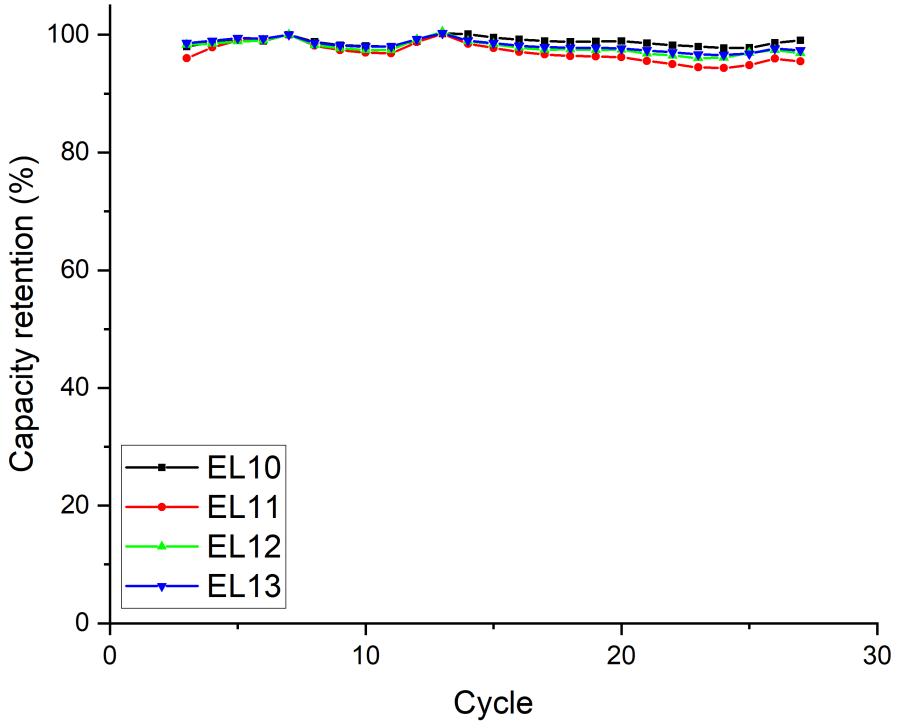

Figure A.5: Cycling performance of symmetrical Si anode coin cells charged and discharged at a constant current of 0.5C between -0.35V and 0.35V with the following electrolyte compositions: 1M $LiPF_6$ in EC:DEC (1:1 vol%) 2 wt% AN 5 wt% FEC 1 wt% VC, 1M $LiPF_6$ in EC:DEC (1:1 vol%) 2 wt% AN 5 wt% FEC 1 wt% VC 1 wt% DAPC, 1M $LiPF_6$ in EC:DEC (1:1 vol%) 2 wt% AN 5 wt% FEC 1 wt% VC 1 wt% DMAA, 1M $LiPF_6$ in EC:DEC (1:1 vol%) 2 wt% AN 5 wt% FEC 1 wt% VC 1 wt% TEOSCN.

Table A.3: EIS results for Electrolyte EL10. Values and standard deviation for different equivalent circuit elements obtained by fit with an equivalent circuit and a Distribution of Relaxation Times map. After 25 cycles R_1 could not be observed anymore in the DRT map and this resistance is likely included in R_s. Therefore, values for R_1 are not shown in the table. EC fit/DRT gives the ratio of the average value obtained by EC fit over the average value obtained by DRT. The value should be as close as possible to 1. This resembles how well the both analyses correspond with each other.

cycles	element	average EC fit	average DRT	average both	EC fit/DRT
formation	R_s (Ω)	5.07±0.16	5.41±0.03	5.24±0.20	0.94
	R_1 (Ω)	2.97±0.71	1.73±1.17	2.35±1.15	1.72
	Q_1 (Fs^{a-1})	8.06E-03±8.05E-03	1.74E-04±1.18E-04	4.12E-03±6.93E-03	46.39
	a_1	0.97±0.00	0.88±0.02	0.93±0.05	1.10
	R_2 (Ω)	17.96±0.43	18.39±0.98	18.18±0.79	0.98
	Q_2 (Fs^{a-1})	1.42E-04±0.32E-04	1.58E-04±0.14E-04	1.50E-04±0.26E-04	0.89
	a_2	0.81±0.02	0.80±0.01	0.81±0.02	1.02
	R_3 (Ω)	2.04±1.06	4.16±0.06	3.10±1.30	0.49
	Q_3 (Fs^{a-1})	9.40E-05±8.16E-05	6.77E-02±5.68E-02	3.39E-02±5.25E-02	0.00
	a_3	0.80±0.11	0.75±0.08	0.77±0.10	1.06
	s_1 ($\Omega s^{\frac{-1}{2}}$)	7.04±0.55	14.67±2.14	10.86±4.12	0.48
	C_0 (F)	0.18±0.01	0.15±0.02	0.17±0.02	1.18
25 cycles	R_s (Ω)	5.48±0.49	5.79±0.44		
	R_1 (Ω)	2.87±0.12			
	Q_1 (Fs^{a-1})	4.73E-03±4.72E-03			
	a_1	0.74±0.22			
	R_2 (Ω)	8.33±1.57	8.62±1.56	8.47±1.57	0.97
	Q_2 (Fs^{a-1})	5.44E-04±0.98E-04	3.66E-04±0.45E-04	4.55E-04±1.17E-04	1.49
	a_2	0.69±0.01	0.79±0.00	0.74±0.05	0.88
	R_3 (Ω)	1.98±0.28	2.05±0.49	2.02±0.40	0.97
	Q_3 (Fs^{a-1})	3.05E-04±2.99E-04	6.23E-02±3.79E-02	3.13E-02±4.10E-02	0.00
	a_3	0.99±0.01	0.75±0.00	0.87±0.12	1.31
	s_1 ($\Omega s^{\frac{-1}{2}}$)	5.64±0.26	9.90±0.33	7.77±2.15	0.57
	C_0 (F)	0.21±0.02	0.13±0.01	0.17±0.04	1.56

Table A.4: EIS results Electrolyte EL11. Values and standard deviation for different equivalent circuit elements obtained by fit with an equivalent circuit and a Distribution of Relaxation Times map. A correct EIS measurement was not performed after formation for the duplicate, so a standard deviation is not shown. After 25 cycles R_1 could not be observed anymore in the DRT map and this resistance is likely included in R_s. Therefore, values for R_1 are not shown in the table. EC fit/DRT gives the ratio of the average value obtained by EC fit over the average value obtained by DRT. The value should be as close as possible to 1. This resembles how well the both analyses correspond with each other.

cycles	element	average EC fit	average DRT	average both	EC fit/DRT
formation	R_s (Ω)	6.31	6.64	6.47±0.17	0.95
	R_1 (Ω)	1.34	0.81	1.08±0.27	1.66
	Q_1 (Fs^{a-1})	1.62E-04	2.11E-04	1.86E-04±0.24E-04	0.77
	a_1	0.82	0.92	0.87±0.05	0.90
	R_2 (Ω)	30.15	32.06	31.11±0.96	0.94
	Q_2 (Fs^{a-1})	1.51E-04	1.75E-04	1.63E-04±0.12E-04	0.86
	a_2	0.81	0.79	0.80±0.01	1.03
	R_3 (Ω)	2.45	4.07	3.26±0.81	0.60
	Q_3 (Fs^{a-1})	1.41E-05	8.03E-02	4.01E-02±4.01E-02	0.00
	a_3	0.90	0.78	0.84±0.06	1.16
	s_1 ($\Omega s^{\frac{-1}{2}}$)	7.87	14.65	11.26±3.39	0.54
	C_0 (F)	0.21	0.14	0.18±0.04	1.50
25 cycles	R_s (Ω)	6.23±0.04	7.15±0.41		
	R_1 (Ω)	2.58±1.04			
	Q_1 (Fs^{a-1})	3.88E-04±3.86E-04			
	a_1	0.79±0.17			
	R_2 (Ω)	19.54±2.40	21.45±1.11	20.49±2.10	0.91
	Q_2 (Fs^{a-1})	2.64E-04±0.39E-04	2.95E-04±0.08E-04	2.80E-04±0.32E-04	0.89
	a_2	0.81±0.04	0.78±0.00	0.80±0.03	1.04
	R_3 (Ω)	1.93±0.28	1.70±0.08	1.82±0.24	1.14
	Q_3 (Fs^{a-1})	1.17E-05±0.42E-05	9.39E-02±1.28E-02	4.70E-02±4.78E-02	0.00
	a_3	0.93±0.03	0.78±0.02	0.86±0.08	1.19
	s_1 ($\Omega s^{\frac{-1}{2}}$)	7.46±0.20	11.77±1.24	9.62±2.33	0.63
	C_0 (F)	0.28±0.07	0.10±0.01	0.19±0.10	2.70

Table A.5: EIS results for Electrolyte EL12. Values and standard deviation for different equivalent circuit elements obtained by fit with an equivalent circuit and a Distribution of Relaxation Times map. A correct EIS measurement was not performed after formation for the duplicate, so a standard deviation is not shown. After 25 cycles R_1 could not be observed anymore in the DRT map and this resistance is likely included in R_s. Therefore, values for R_1 are not shown in the table. EC fit/DRT gives the ratio of the average value obtained by EC fit over the average value obtained by DRT. The value should be as close as possible to 1. This resembles how well the both analyses correspond with each other.

cycles	element	average EC fit	average DRT	average both	EC fit/DRT
formation	R_s (Ω)	5.48	5.67	5.57±0.09	0.97
	R_1 (Ω)	3.47	0.99	2.23±1.24	3.50
	Q_1 (Fs^{a-1})	2.64E-05	1.68E-04	9.74E-05±7.10E-05	0.16
	a_1	0.86	0.87	0.87±0.01	0.98
	R_2 (Ω)	15.74	16.47	16.10±0.36	0.96
	Q_2 (Fs^{a-1})	1.46E-04	1.71E-04	1.59E-04±0.12E-04	0.86
	a_2	0.83	0.81	0.82±0.01	1.03
	R_3 (Ω)	1.80	2.89	2.35±0.54	0.62
	Q_3 (Fs^{a-1})	2.71E-02	2.45E-02	2.58E-02±0.13E-02	1.11
	a_3	1.00	0.82	0.91±0.09	1.22
	s_1 ($\Omega s^{\frac{-1}{2}}$)	4.74	8.82	6.78±2.04	0.54
	C_0 (F)	0.18	0.25	0.22±0.03	0.73
25 cycles	R_s (Ω)	5.80±0.07	6.78±0.64		
	R_1 (Ω)	2.11±0.04			
	Q_1 (Fs^{a-1})	5.59E-02±5.58E-02			
	a_1	0.72±0.27			
	R_2 (Ω)	8.66±0.56	8.86±0.10	8.76±0.41	0.98
	Q_2 (Fs^{a-1})	4.65E-04±0.29	4.59E-04±0.40E-04	4.62E-04±0.35E-05	1.01
	a_2	0.75±0.02	0.76±0.02	0.75±0.02	0.98
	R_3 (Ω)	2.50±0.30	2.20±0.60	2.35±0.50	1.14
	Q_3 (Fs^{a-1})	3.42E-05±2.29E-05	5.30E-02±2.23E-02	2.65E-02±3.08E-02	0.00
	a_3	0.86±0.07	0.78±0.00	0.82±0.06	1.10
	s_1 ($\Omega s^{\frac{-1}{2}}$)	4.96±0.13	7.37±0.22	6.16±1.22	0.67
	C_0 (F)	0.19±0.01	0.16±0.00	0.18±0.02	1.21

Table A.6: EIS results for Electrolyte EL13. Values and standard deviation for different equivalent circuit elements obtained by fit with an equivalent circuit and a Distribution of Relaxation Times map. After 25 cycles R_1 could not be observed anymore in the DRT map and this resistance is likely included in R_s. Therefore, values for R_1 are not shown in the table. EC fit/DRT gives the ratio of the average value obtained by EC fit over the average value obtained by DRT. The value should be as close as possible to 1. This resembles how well the both analyses correspond with each other.

cycles	element	average EC fit	average DRT	average both	EC fit/DRT
formation	R_s (Ω)	5.15±0.01	5.24±0.01	5.20±0.06	0.98
	R_1 (Ω)	2.24±0.27	2.22±0.27	2.23±0.61	1.01
	Q_1 (Fs^{a-1})	5.07E-03±0.01E-03	1.04E-04±0.12E-04	2.58E-03±4.35E-03	48.83
	a_1	0.91±0.00	0.83±0.00	0.87±0.07	1.10
	R_2 (Ω)	13.53±1.70	14.15±1.70	13.84±1.35	0.96
	Q_2 (Fs^{a-1})	1.53E-04±0.14E-04	1.69E-04±0.14E-04	1.61E-04±0.57E-04	0.91
	a_2	0.82±0.00	0.80±0.00	0.81±0.07	1.02
	R_3 (Ω)	3.18±0.37	3.44±0.37	3.31±1.12	0.92
	Q_3 (Fs^{a-1})	1.39E-02±0.11E-02	1.65E-02±0.11E-02	1.52E-02±0.99E-02	0.84
	a_3	0.90±0.00	0.83±0.00	0.87±0.05	1.09
	s_1 ($\Omega s^{\frac{-1}{2}}$)	5.84±1.41	11.97±1.41	8.91±3.33	0.49
	C_0 (F)	0.21±0.03	0.20±0.03	0.20±0.02	1.05
25 cycles	R_s (Ω)	5.21±0.36	5.64±0.26		
	R_1 (Ω)	1.19±0.36			
	Q_1 (Fs^{a-1})	9.77E-03±9.75E-03			
	a_1	0.96±0.04			
	R_2 (Ω)	6.13±1.50	8.95±0.11	7.54±1.77	0.68
	Q_2 (Fs^{a-1})	3.13E-04±0.25E-04	4.25E-04±0.09E-04	3.69E-04±0.59E-04	0.74
	a_2	0.89±0.03	0.79±0.00	0.84±0.06	1.13
	R_3 (Ω)	5.87±1.02	2.66±0.19	4.26±1.76	2.20
	Q_3 (Fs^{a-1})	1.71E-03±1.64E-03	2.79E-02±0.08E-02	1.48E-02±1.32E-02	0.06
	a_3	0.62±0.15	0.78±0.02	0.70±0.13	0.80
	s_1 ($\Omega s^{\frac{-1}{2}}$)	5.59±0.36	7.45±0.12	6.52±0.97	0.75
	C_0 (F)	0.23±0.00	0.16±0.00	0.20±0.03	1.43

Bibliography

[1] Maziar Ashuri, Qianran He, and Leon L Shaw. Silicon as a potential anode material for Li-ion batteries: where size, geometry and structure matter. *Nanoscale*, 8:74, 2015. doi: 10.1039/c5nr05116a. URL www.rsc.org/nanoscale.

[2] Felix Aupperle, Natascha Von Aspern, Debbie Berghus, Felix Weber, Gebrekidan Gebresilassie Eshetu, Martin Winter, and Egbert Figgemeier. The Role of Electrolyte Additives on the Interfacial Chemistry and Thermal Reactivity of Si-Anode-Based Li-Ion Battery. *ACS Applied Energy Materials*, 2(9):6513–6527, 9 2019. ISSN 25740962. doi: 10.1021/acsaem.9b01094.

[3] Malar Azagarsamy, Kulandaivelu Sivanandan, Hany Basam Eitouni, Jonathan P. Mailoa, Georgy Samsonidze, and Boris Kozinsky. Poly(pyrocarbonate)-based polymer electrolytes for high voltage Lithium Ion Batteries , 12 2019.

[4] Bob Zollo. Measuring DCIR of Lithium-Ion Cells, 4 2020. URL https://www.electronicdesign.com/technologies/test-measurement/article/21128843/keysight-technologies-measuring-dcir-of-lithiumion-cells.

[5] Bernard A. Boukamp. Distribution (function) of relaxation times, successor to complex nonlinear least squares analysis of electrochemical impedance spectroscopy? *JPhys Energy*, 2(4), 2020. ISSN 25157655. doi: 10.1088/2515-7655/aba9e0.

[6] L. B. Chen, J. Y. Xie, H. C. Yu, and T. H. Wang. An amorphous Si thin film anode with high capacity and long cycling life for lithium ion batteries. *Journal of Applied Electrochemistry*, 39(8):1157–1162, 8 2009. ISSN 0021891X. doi: 10.1007/s10800-008-9774-1.

[7] Libao Chen, Ke Wang, Xiaohua Xie, and Jingying Xie. Effect of vinylene carbonate (VC) as electrolyte additive on electrochemical performance of Si film anode for lithium ion batteries. *Journal of Power Sources*, 174(2):538–543, 2007. ISSN 03787753. doi: 10.1016/j.jpowsour.2007.06.149.

[8] Shuru Chen, Chaojiang Niu, Hongkyung Lee, Qiuyan Li, Lu Yu, Wu Xu, Ji Guang Zhang, Eric J. Dufek, M. Stanley Whittingham, Shirley Meng, Jie Xiao, and Jun Liu. Critical Parameters for Evaluating Coin Cells and Pouch Cells of Rechargeable Li-Metal Batteries. *Joule*, 3(4):1094–1105, 2019. ISSN 25424351. doi: 10.1016/j.joule.2019.02.004.

[9] Nam Soon Choi, Kyoung Han Yew, Kyu Youl Lee, Minseok Sung, Ho Kim, and Sung Soo Kim. Effect of fluoroethylene carbonate additive on interfacial properties of silicon thin-film electrode. *Journal of Power Sources*, 161(2):1254–1259, 2006. ISSN 03787753. doi: 10.1016/j.jpowsour.2006.05.049.

[10] Woosung Choi, Heon Cheol Shin, Ji Man Kim, Jae Young Choi, and Won Sub Yoon. Modeling and applications of electrochemical impedance spectroscopy (Eis) for lithium-ion batteries. *Journal of Electrochemical Science and Technology*, 11(1):1–13, 2020. ISSN 22889221. doi: 10.33961/jecst.2019.00528.

[11] Michael A. Danzer. Generalized distribution of relaxation times analysis for the characterization of impedance spectra. *Batteries*, 5(3):1–16, 2019. ISSN 23130105. doi: 10.3390/batteries5030053.

[12] Arjen Peter Didden. Silicon composition material for use as battery anode, 2021.

[13] Noémie Elgrishi, Kelley J. Rountree, Brian D. McCarthy, Eric S. Rountree, Thomas T. Eisenhart, and Jillian L. Dempsey. A Practical Beginner's Guide to Cyclic Voltammetry. *Journal of Chemical Education*, 95(2):197–206, 2 2018. ISSN 19381328. doi: 10.1021/acs.jchemed.7b00361.

[14] Gebrekidan Gebresilassie Eshetu and Egbert Figgemeier. Confronting the Challenges of Next-Generation Silicon Anode-Based Lithium-Ion Batteries: Role of Designer Electrolyte Additives and Polymeric Binders, 6 2019. ISSN 1864564X.

[15] Rosamaría Fong, Ulrich von Sacken, and J. R. Dahn. Studies of Lithium Intercalation into Carbons Using Nonaqueous Electrochemical Cells. *Journal of The Electrochemical Society*, 137(7):2009–2013, 1990. ISSN 0013-4651. doi: 10.1149/1.2086855.

[16] Rohit Ranganathan Gaddam, Leon Katzenmeier, Xaver Lamprecht, and Aliaksandr S. Bandarenka. Review on physical impedance models in modern battery research. *Physical Chemistry Chemical Physics*, 23(23):12926–12944, 2021. ISSN 14639076. doi: 10.1039/d1cp00673h.

[17] Pengjian Guan, Lin Liu, and Xianke Lin. Simulation and Experiment on Solid Electrolyte Interphase (SEI) Morphology Evolution and Lithium-Ion Diffusion. *Journal of The Electrochemical Society*, 162 (9):A1798–A1808, 2015. ISSN 0013-4651. doi: 10.1149/2.0521509jes.

[18] Atetegeb Meazah Haregewoin, Aselefech Sorsa Wotango, and Bing Joe Hwang. Electrolyte additives for lithium ion battery electrodes: Progress and perspectives, 6 2016. ISSN 17545706.

[19] M. Herstedt, D. P. Abraham, J. B. Kerr, and K. Edström. X-ray photoelectron spectroscopy of negative electrodes from high-power lithium-ion cells showing various levels of power fade. *Electrochimica Acta*, 49(28):5097–5110, 11 2004. ISSN 00134686. doi: 10.1016/j.electacta.2004.06.021.

[20] Tingzheng Hou, Guang Yang, Nav Nidhi Rajput, Julian Self, Sang Won Park, Jagjit Nanda, and Kristin A. Persson. The influence of FEC on the solvation structure and reduction reaction of LiPF6/EC electrolytes and its implication for solid electrolyte interphase formation. *Nano Energy*, 64(July):103881, 2019. ISSN 22112855. doi: 10.1016/j.nanoen.2019.103881. URL https://doi.org/10.1016/j.nanoen.2019.103881.

[21] Yang Jiang, Gregory Offer, Jun Jiang, Monica Marinescu, and Huizhi Wang. Voltage Hysteresis Model for Silicon Electrodes for Lithium Ion Batteries, Including Multi-Step Phase Transformations, Crystallization and Amorphization. *Journal of The Electrochemical Society*, 167(13):130533, 10 2020. ISSN 1945-7111. doi: 10.1149/1945-7111/abbbba.

[22] T R Jow, M S Ding, K Xu, S S Zhang, J L Allen, K Amine, and G L Henriksen. Nonaqueous electrolytes for wide-temperature-range operation of Li-ion cells. 121:343–348, 2003. doi: 10.1016/S0378-7753(03)00153-8.

[23] Roland Jung, Michael Metzger, Filippo Maglia, Christoph Stinner, and Hubert A. Gasteiger. Oxygen Release and Its Effect on the Cycling Stability of LiNi x Mn y Co z O 2 (NMC) Cathode Materials for Li-Ion Batteries . *Journal of The Electrochemical Society*, 164(7):A1361–A1377, 2017. ISSN 0013-4651. doi: 10.1149/2.0021707jes.

[24] Jae Kwang Kim, Gyu Bong Cho, Ho Suk Ryu, Hyo Jun Ahn, Kwon Koo Cho, Ki Won Kim, Aleksandar Matic, Per Jacobsson, and Jou Hyeon Ahn. Electrochemical properties of a full cell of lithium iron phosphate cathode using thin amorphous silicon anode, 2014. ISSN 01672738.

[25] Jung Sub Kim, Dongjin Byun, and Joong Kee Lee. Electrochemical characteristics of amorphous silicon thin film electrode with fluoroethylene carbonate additive. *Current Applied Physics*, 14(4): 596–602, 2014. ISSN 15671739. doi: 10.1016/j.cap.2014.02.008. URL http://dx.doi.org/10.1016/j.cap.2014.02.008.

[26] Koeun Kim, Hyunsoo Ma, Sewon Park, and Nam-Soon Choi. Electrolyte-Additive-Driven Interfacial Engineering for High-Capacity Electrodes in Lithium-Ion Batteries: Promise and Challenges. *ACS Energy Letters*, 5(5):1537–1553, 5 2020. ISSN 2380-8195. doi: 10.1021/acsenergylett.0c00468.

[27] T. L. Kulova, A. M. Skundin, Yu V. Pleskov, E. I. Terukov, and O. I. Kon'kov. Lithium insertion into amorphous silicon thin-film electrodes. *Journal of Electroanalytical Chemistry*, 600(1):217–225, 2 2007. ISSN 15726657. doi: 10.1016/j.jelechem.2006.07.002.

[28] Andrzej Lasia. *Electrochemical impedance spectroscopy and its applications*, volume 9781461489. 2014. ISBN 9781461489337. doi: 10.1007/978-1-4614-8933-7.

[29] Ki Lyoung Lee, Ju Young Jung, Seung Won Lee, Hee Soo Moon, and Jong Wan Park. Electrochemical characteristics of a-Si thin film anode for Li-ion rechargeable batteries. *Journal of Power Sources*, 129(2):270–274, 2004. ISSN 03787753. doi: 10.1016/j.jpowsour.2003.10.013.

[30] Seon Hwa Lee, Jang Yeon Hwang, Seong Jin Park, Geon Tae Park, and Yang Kook Sun. Adiponitrile (C6H8N2): A New Bi-Functional Additive for High-Performance Li-Metal Batteries. *Advanced Functional Materials*, 29(30):1–9, 2019. ISSN 16163028. doi: 10.1002/adfm.201902496.

[31] M. D. Levi and D. Aurbach. Simultaneous measurements and modeling of the electrochemical impedance and the cyclic voltammetric characteristics of graphite electrodes doped with lithium, 1997. ISSN 15206106.

[32] Shiyou Li, Dongni Zhao, Peng Wang, Xiaoling Cui, and Fengjuan Tang. Electrochemical effect and mechanism of adiponitrile additive for high-voltage electrolyte. *Electrochimica Acta*, 222:668–677, 12 2016. ISSN 0013-4686. doi: 10.1016/J.ELECTACTA.2016.11.022.

[33] Jun Liu, Zhenan Bao, Yi Cui, Eric J. Dufek, John B. Goodenough, Peter Khalifah, Qiuyan Li, Bor Yann Liaw, Ping Liu, Arumugam Manthiram, Y. Shirley Meng, Venkat R. Subramanian, Michael F. Toney, Vilayanur V. Viswanathan, M. Stanley Whittingham, Jie Xiao, Wu Xu, Jihui Yang, Xiao Qing Yang, and Ji Guang Zhang. Pathways for practical high-energy long-cycling lithium metal batteries. *Nature Energy*, 4(3):180–186, 2019. ISSN 20587546. doi: 10.1038/s41560-019-0338-x.

[34] Mahmoud Madian, Alexander Eychmüller, and Lars Giebeler. Current Advances in TiO 2-Based Nanostructure Electrodes for High Performance Lithium Ion Batteries. 2018. doi: 10.3390/batteries4010007. URL www.mdpi.com/journal/batteries.

[35] Arumugam Manthiram. An Outlook on Lithium Ion Battery Technology. *ACS Central Science*, 3 (10):1063–1069, 10 2017. ISSN 23747951. doi: 10.1021/acscentsci.7b00288.

[36] Chengyu Mao, Rose E. Ruther, Jianlin Li, Zhijia Du, and Ilias Belharouak. Identifying the limiting electrode in lithium ion batteries for extreme fast charging. *Electrochemistry Communications*, 97(September):37–41, 2018. ISSN 13882481. doi: 10.1016/j.elecom.2018.10.007. URL https://doi.org/10.1016/j.elecom.2018.10.007.

[37] Behrooz Mosallanejad. Asian Journal of Green Chemistry A review on advanced functional electrolyte additives for silicon-based lithium-ion batteries. *Asian Journal of Green Chemistry*, 4:473–490, 2020. doi: 10.33945/SAMI/AJGC.2020.4.10. URL www.ajgreenchem.com.

[38] Vivian Murray, David S. Hall, and J. R. Dahn. A Guide to Full Coin Cell Making for Academic Researchers. *Journal of The Electrochemical Society*, 166(2):A329–A333, 2019. ISSN 0013-4651. doi: 10.1149/2.1171902jes.

[39] M. N. Obrovac and Leif Christensen. Structural changes in silicon anodes during lithium insertion/extraction. *Electrochemical and Solid-State Letters*, 7(5), 2004. ISSN 10990062. doi: 10.1149/1.1652421.

[40] Ossila. Cyclic Voltammetry: Principles, Setup, and Applications. URL https://www.ossila.com/pages/cyclic-voltammetry.

[41] Ke Pan, Feng Zou, Marcello Canova, Yu Zhu, and Jung Hyun Kim. Comprehensive electrochemical impedance spectroscopy study of Si-Based anodes using distribution of relaxation times analysis. *Journal of Power Sources*, 479(October), 2020. ISSN 03787753. doi: 10.1016/j.jpowsour.2020.229083.

[42] Elad Pollak, Gregory Salitra, Valentina Baranchugov, and Doron Aurbach. In situ conductivity, impedance spectroscopy, and ex situ Raman spectra of amorphous silicon during the insertion/extraction of lithium. *Journal of Physical Chemistry C*, 111(30):11437–11444, 8 2007. ISSN 19327447. doi: 10.1021/jp0729563.

[43] Irina A. Profatilova, Christoph Stock, André Schmitz, Stefano Passerini, and Martin Winter. Enhanced thermal stability of a lithiated nano-silicon electrode by fluoroethylene carbonate and vinylene carbonate. *Journal of Power Sources*, 222:140–149, 2013. ISSN 03787753. doi: 10.1016/j.jpowsour.2012.08.066. URL http://dx.doi.org/10.1016/j.jpowsour.2012.08.066.

[44] Boris Ravdel, K. M. Abraham, Robert Gitzendanner, Joseph DiCarlo, Brett Lucht, and Chris Campion. Thermal stability of lithium-ion battery electrolytes. In *Journal of Power Sources*, volume 119-121, pages 805–810, 6 2003. doi: 10.1016/S0378-7753(03)00257-X.

[45] Jaewook Shin, Tae Hee Kim, Yongju Lee, and Eun Ae Cho. Key functional groups defining the formation of Si anode solid-electrolyte interphase towards high energy density Li-ion batteries, 3 2020. ISSN 24058297.

[46] Vaithiyalingam Shutthanandan, Manjula Nandasiri, Jianming Zheng, Mark H. Engelhard, Wu Xu, Suntharampillai Thevuthasan, and Vijayakumar Murugesan. Applications of XPS in the characterization of Battery materials, 2 2019. ISSN 03682048.

[47] R. Spotnitz. Simulation of capacity fade in lithium-ion batteries. *Journal of Power Sources*, 113 (1):72–80, 1 2003. ISSN 0378-7753. doi: 10.1016/S0378-7753(02)00490-1.

[48] Caleb Stetson, Taeho Yoon, Jaclyn Coyle, William Nemeth, Matt Young, Andrew Norman, Svitlana Pylypenko, Chunmei Ban, Chun Sheng Jiang, Mowafak Al-Jassim, and Anthony Burrell. Three-dimensional electronic resistivity mapping of solid electrolyte interphase on Si anode materials. *Nano Energy*, 55:477–485, 1 2019. ISSN 22112855. doi: 10.1016/j.nanoen.2018.11.007.

[49] Caleb Stetson, Yanli Yin, Andrew Norman, Steven P. Harvey, Manuel Schnabel, Chunmei Ban, Chun Sheng Jiang, Steven C. DeCaluwe, and Mowafak Al-Jassim. Evolution of solid electrolyte interphase and active material in the silicon wafer model system. *Journal of Power Sources*, 482: 228946, 1 2021. ISSN 0378-7753. doi: 10.1016/J.JPOWSOUR.2020.228946.

[50] Tatsuko Takei. Properties of non-aqueous solvents: Solubility and conductivity of solutions, 1988. ISSN 02578972.

[51] Norio Takenaka, Yuichi Suzuki, Hirofumi Sakai, and Masataka Nagaoka. On electrolyte-dependent formation of solid electrolyte interphase film in lithium-ion batteries: Strong sensitivity to small structural difference of electrolyte molecules. *Journal of Physical Chemistry C*, 118(20):10874–10882, 5 2014. ISSN 19327455. doi: 10.1021/jp5018696.

[52] Arthur Von Wald Cresce, Oleg Borodin, and Kang Xu. Correlating Li+ solvation sheath structure with interphasial chemistry on graphite. *Journal of Physical Chemistry C*, 116(50):26111–26117, 2012. ISSN 19327447. doi: 10.1021/jp303610t.

[53] Aiping Wang, Sanket Kadam, Hong Li, Siqi Shi, and Yue Qi. Review on modeling of the anode solid electrolyte interphase (SEI) for lithium-ion batteries, 12 2018. ISSN 20573960.

[54] Chong-min Wang, Kang Xu, Ji-guang Zhang, and Wu Xu. Wide-Temperature Electrolytes for Lithium-Ion Batteries. 2017. doi: 10.1021/acsami.7b04099.

[55] Fenglin Wang, Gen Chen, Ning Zhang, Xiaohe Liu, and Renzhi Ma. Engineering of carbon and other protective coating layers for stabilizing silicon anode materials. *Carbon Energy*, 1(2):219–245, 2019. ISSN 26379368. doi: 10.1002/cey2.24.

[56] Xueyuan Wang, Xuezhe Wei, Jiangong Zhu, Haifeng Dai, Yuejiu Zheng, Xiaoming Xu, and Qijun Chen. A review of modeling, acquisition, and application of lithium-ion battery impedance for onboard battery management, 2 2021. ISSN 25901168.

[57] Hui Xia, Songbai Tang, and Li Lu. Properties of amorphous Si thin film anodes prepared by pulsed laser deposition. *Materials Research Bulletin*, 42(7):1301–1309, 7 2007. ISSN 00255408. doi: 10.1016/j.materresbull.2006.10.007.

[58] Kang Xu. Nonaqueous liquid electrolytes for lithium-based rechargeable batteries. *Chemical Reviews*, 104(10):4307–4311, 10 2004. ISSN 00092665. doi: 10.1021/cr030203g.

[59] Zhixin Xu, Jun Yang, Hongping Li, Yanna Nuli, and Jiulin Wang. Electrolytes for advanced lithium ion batteries using silicon-based anodes, 2019. ISSN 20507496.

[60] Benjamin T. Young, David R. Heskett, Cao Cuong Nguyen, Mengyun Nie, Joseph C. Woicik, and Brett L. Lucht. Hard X-ray photoelectron spectroscopy (HAXPES) investigation of the silicon solid electrolyte interphase (SEI) in lithium-ion batteries. *ACS Applied Materials and Interfaces*, 7(36): 20004–20011, 2015. ISSN 19448252. doi: 10.1021/acsami.5b04845.

[61] Haotian Zhang. Battery thermal management with phase change materials (PCMs). Technical report, 2018.

[62] Longfei Zhang, Lili Chai, Li Zhang, Ming Shen, Xianlin Zhang, Vincent S. Battaglia, Tyler Stephenson, and Honghe Zheng. Synergistic effect between lithium bis(fluorosulfonyl)imide (LiFSI) and lithium bis-oxalato borate (LiBOB) salts in LiPF6-based electrolyte for high-performance Li-ion batteries. *Electrochimica Acta*, 127:39–44, 2014. ISSN 00134686. doi: 10.1016/j.electacta.2014.02.008. URL http://dx.doi.org/10.1016/j.electacta.2014.02.008.

[63] S S Zhang, K Xu, J L Allen, and T R Jow. Effect of propylene carbonate on the low temperature performance of Li-ion cells. 110:216–221, 2002.

[64] Shuo Zhang, Meinan He, Chi Cheung Su, and Zhengcheng Zhang. Advanced electrolyte/additive for lithium-ion batteries with silicon anode, 8 2016. ISSN 22113398.

[65] Yaguang Zhang, Ning Du, and Deren Yang. Designing superior solid electrolyte interfaces on silicon anodes for high-performance lithium-ion batteries, 11 2019. ISSN 20403372.

[66] Xiaohui Zhao, Gouri Cheruvally, Changhyeon Kim, Kwon Koo Cho, Hyo Jun Ahn, Ki Won Kim, and Jou Hyeon Ahn. Lithium/sulfur secondary batteries: A review, 6 2016. ISSN 22889221.

[67] Guobin Zhu, Siming Yang, Yan Wang, Qunting Qu, and Honghe Zheng. Dimethylacrylamide, a novel electrolyte additive, can improve the electrochemical performances of silicon anodes in lithium-ion batteries. *RSC Advances*, 9(1):435–443, 2019. ISSN 20462069. doi: 10.1039/C8RA07988A.